CZECH TECHNICAL UNIVERSITY IN PRAGUE
Faculty of Civil Engineering
Department of Mechanics

Degradation modelling of concrete and reinforced concrete structures due to carbonation, chloride ingress and alkali-silica reaction

DOCTORAL THESIS

Ing. Karolina Jandová

Doctoral study programme:	Civil Engineering
Branch of study:	Physical and Material Engineering
Doctoral thesis tutor:	Doc. Ing. Vít Šmilauer, Ph.D., DSc.

Prague, 2020

CZECH TECHNICAL UNIVERSITY IN PRAGUE
Faculty of Civil Engineering
Thákurova 7, 166 29 Praha 6

DECLARATION

Ph.D. student's name:	Ing. Karolina JANDOVÁ
Title of the doctoral thesis:	Degradation modelling of concrete and reinforced concrete structures due to carbonation, chloride ingress and alkali-silica reaction

I hereby declare that this doctoral thesis is my own work and effort written under the guidance of the tutor Vít ŠMILAUER.
All sources and other materials used have been quoted in the list of references.

The doctoral thesis was written in connection with research on the projects:
TAČR TA04031458 and SGS OHK1-074/16

In Prague on ....
signature

Acknowledgements

I would very much like to thank Doc. Ing. Vít Šmilauer, Ph.D., DSc. for the professional supervising, patience and valuable advices during my studies and work on my dissertation thesis. I would like to thank Ing. V. Junek from Pontex, Ltd., who provided us experimental data for Prague's concrete bridge. We gratefully acknowledge the financial support from the Technology Agency of the Czech Republic under the project TA04031458 (Software for prediction and modelling of durability and safety of transportation structures) and support from Czech Science Foundation under the project 16-20008S (Multiscale modeling of early age concrete).

Abstract

Concrete is the most man-made material in today's world. Concrete and reinforced concrete may deteriorate due to several reasons, the focus here is devoted to carbonation, chloride ingress or alkali-silica reaction. The presence of carbon dioxide in the atmosphere, available chlorides from de-icing salts or salt water and certain level of alkalis in the cement - all those factors have an impact on structural serviceability and life design of concrete and reinforced concrete structures.

The thesis presents two modelling areas of deterioration. The first area belongs to a chemo-mechanical tasks covering initiation and propagation periods of chloride and carbonation steel corrosion, taking into account concrete mix design, supplementary cementitious materials, concrete cover, crack width and environmental conditions. The strategy for solving this coupled problem stems from three stages. First, a short-term fracture-plastic constitutive model predicts cracking prior to the carbonation and chloride ingress. Second, 1D model of carbonation and chloride ingress yields the time of concrete cracking, spalling and the effective steel area. Third, mechanical analysis assesses the load-bearing capacity of a structure in dependence on the state of reinforcement corrosion. The second area addresses a chemo-mechanical expansion for alkali-silica reaction (ASR), taking into account its kinetics, environmental conditions, alkali content, reactive part of aggregates and stress-state.

Validation for carbonation and chloride ingress covers several real examples, such as a concrete strut of a prestressed bridge and Nougawa bridge in Japan. Validation for ASR covers free sample expansion and constrained members. Performance of the model is demonstrated on a concrete gravity dam, set as a benchmark example.

Abstrakt

V dnešní době patří beton mezi nejvíce vyráběný materiál ve světě. Vlastnosti betonu a železobetonu se mohou zhoršovat z několika důvodů, v našem případě se zaměříme na karbonataci, vnikání chloridů a alkalicko-křemičitou reakci. Přítomnost oxidu uhličitého v atmosféře, stejně tak výskyt chloridů z rozmrazovacích solí nebo slané vody a určitá úroveň alkálií v cementu - všechny tyto faktory mají vliv na konstrukční provozuschopnost a životnost betonových a železobetonových konstrukcí.

Tato práce se věnuje modelování degradace dvou oblastní. První z nich je oblast, kde chemomechanické modely popisují období iniciace a průběh koroze výztuže způsobené karbonatací nebo chloridy. Výpočty zohledňují návrh betonové směsi, využití přímesí, krycí vrstvu, šířku trhlin a podmínky okolního prostředí. Sdružená úloha je řešena ve třech fázích. První z nich je plastický model s poškozením, který predikuje vznik trhlin před vniknutím agresivních látek. Druhá fáze využívá 1D transportního modelu, který predikuje dobu vzniku trhliny v krycí vrstvě, dobu odpadnutí krycí vrstvy a efektivní plochu oceli. V poslední třetí fázi se stanovuje nechanickou analýzou únosnost konstrukce v závislosti na stavu koroze výztuže. Druhá oblast se zabývá chemicko-mechanickou expanzí způsobenou alkalicko-křemičitou reakcí, s přihlédnutím k její kinetice, podmínkám okolního prostředí, obsahu alkálií, reaktivní části kameniva a stavu napětí.

Validace byly provedeny na několika realných konstrukcích zatížených chloridy a karbonatací, například na betonové vzpěře předpjatého mostu a mostu Nougawa v Japonsku. Bylo provedeno několik validací pro volnou expanzi způsobenou ASR a pro případ, že je takovéto expanzi zabráněno. Využití a porovnání ASR modelu je demonstrováno na betonové gravitační přehradě.

Contents

List of Figures

List of Tables

Chapter 1

Aim and the scope

1.1 The need for modelling software tool

Several phenomenological, multiscale, physical and empirical models deal with the description of corrosion and degradation due to chloride ingress, carbonation and ASR reaction [72], [52], [51], [110], [90]. Today, wider application is possible through a software, providing a framework for modelling activities and exposing those models to users. The objective of this thesis is the implementation of selected models into a software, reflecting crack width and its effect on transport properties.

Available validated models in a software allow advanced development, design and maintenance of bridges, tunnels and other civil engineering constructions. It will also assist in the decision-making and planning of repairs and reconstructions. During the design and assessment stages, it is possible to take into account cracks caused by load actions, but also cracks caused by hydration heat or shrinkage, which have significant influence on the origin of micro-cracks in concrete with a negative impact on corrosion of reinforcement and time degradation of concrete.

In the example of the column, the chloride attack is applied in the form of a surface loading, depicted by red color in Fig. 1.1.

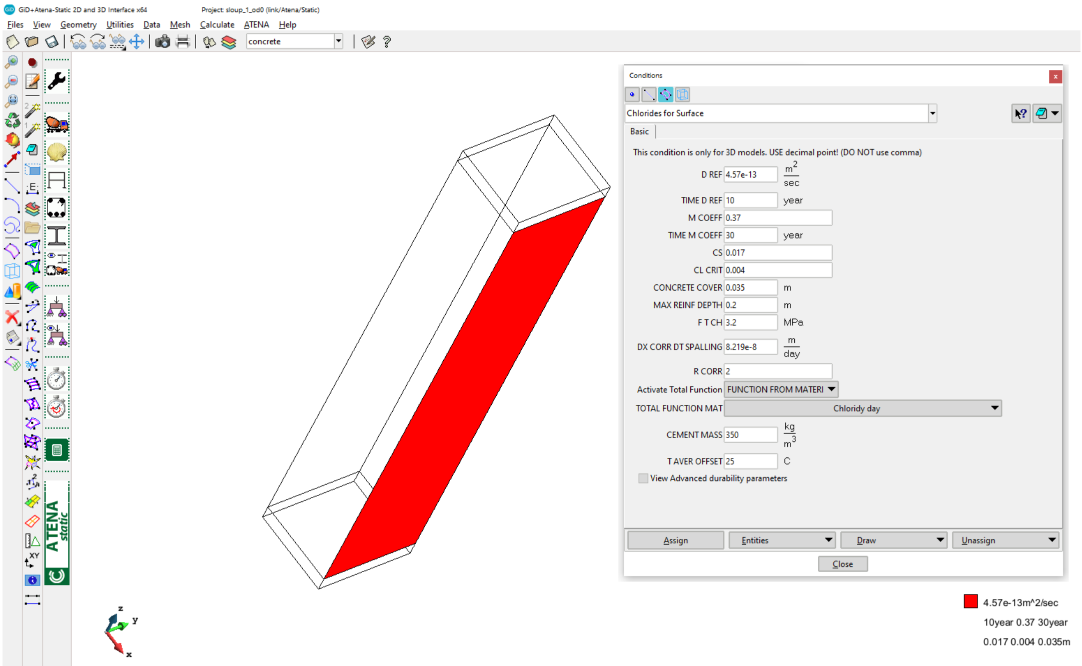

Chlorides for Surface

This condition is only for 3D models. USE decimal point! (DO NOT use comma)

D REF 4.57e-13 $\frac{m^2}{sec}$

TIME D REF 10 year

M COEFF 0.37

TIME M COEFF 30 year

CS 0.017

CL CRIT 0.004

CONCRETE COVER 0.035 m

MAX REINF DEPTH 0.2 m

F T CH 3.2 MPa

DX CORR DT SPALLING 8.219e-8 $\frac{m}{day}$

R CORR 2

Activate Total Function FUNCTION FROM MATERI

TOTAL FUNCTION MAT Chloridy day

CEMENT MASS 350 $\frac{kg}{m^3}$

T AVER OFFSET 25 C

☐ View Advanced durability parameters

🟥 4.57e-13m^2/sec

10year 0.37 30year

0.017 0.004 0.035m

Figure 1.1: Software view for modelling of chloride ingress in the form of a surface loading, with optional parameters affecting the time of corrosion start, time of cracking or spalling of concrete cover and the direct corrosion of the reinforcement.

Chapter 2

State of the art

2.1 Introduction

All concrete structures deteriorate slowly or quickly during their service lives. Reinforcement corrosion, accompanied with spalling of the concrete cover, has been identified as the most serious damaging mechanism for reinforced concrete structures (RC) in the world [106]. Consequently, this generally leads to finite serviceability and durability, affecting life cycle cost with environmental impact.

2.2 Durability and steel corrosion

Durability of reinforced concrete structure is its ability to withstand the environment action over the design life with adequate maintenance, without need of major repairs or loss of serviceability [2]. As already mentioned, the most common RC structure durability problems relate to corrosion of reinforcing steel. In industrially developed countries, maintenance cost is estimated 30-40% of total budget in construction industry [93].

2.2.1 Basic mechanisms of steel corrosion

Iron and steel are thermodynamically unstable materials and naturally try to return to a stable form, namely oxides (rust materials). This phenomenon is known as reinforcement corrosion, i.e. an electrochemical process that requires an anode, a cathode and an electrolyte. Pore water in the hardened cement paste creates the electrolyte and the steel reinforcement forms the anode and cathode [62]. During chemical reaction electrons transfer at the interface between the metal and the water. A scheme of the steel corrosion process is shown in Fig. 2.1.

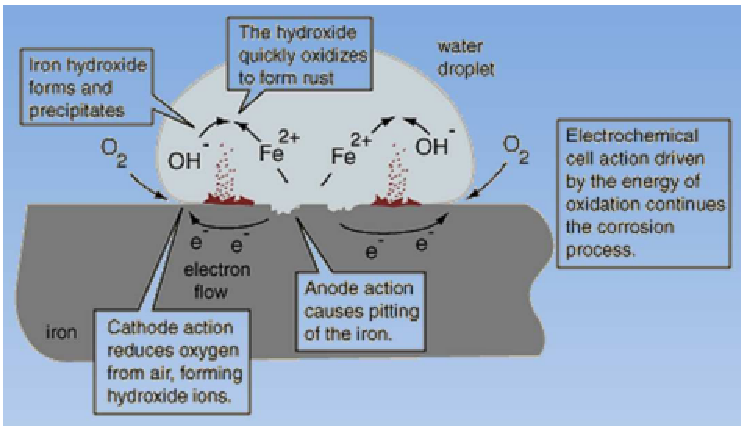

Figure 2.1: Scheme of a steel corrosion cell in concrete [86]

The corrosion process where oxygen is consumed and water is needed can be summarized by the following reaction [62]:

$$2Fe + 2H_2O + O_2 \rightarrow 2Fe(OH)_2 \tag{2.1}$$

During corrosion, two reactions on the surface occurs at the same time, very close to each other (microscopic and macroscopic distances). One of them is oxidation, the dissolution of iron, also known as anodic reaction. Oxidation forms ferrous cations and leaves electrons in the metal:

$$Fe \rightarrow Fe^{2+} + 2e^- \tag{2.2}$$

The second reaction is oxygen reduction, also called the cathodic reaction, where the free electrons from the oxidation are consumed by oxygen in the presence of water to form the hydroxyl:

$$O_2 + 2H_2O + 4e^- = 4OH^- \tag{2.3}$$

Various oxides can be formed during reinforcement corrosion depending on the environment conditions, e.g. $Fe(OH)_2$ (ferrous hydroxide), Fe_3O_4 (ferrous ferric oxide), Fe_2O_3 (ferric oxide),...

2.2.2 Corrosion kinetics

The corrosion rate of reinforcement is given by corrosion current density.

The corrosion current densities range between 0.2 to 10 μA/cm^2 [16]. The following broad criteria have been developed, summarized further in Tab. 2.1. The table assumes volume increase of rust as three on average.

Corrosion rate	i_{corr} [μA/cm^2]	Section loss [μm/year]	Rust growth [μm/year]
Passive corrosion	$<$ 0.2	2.3	7.0
Low to moderate corrosion	0.2 - 1.0	2.3 - 11.6	7.0 - 34.8
Moderate to high corrosion	1.0 - 10.0	11.6 - 116	34.8 - 348
High corrosion	$>$10.0	$>$116	348

Table 2.1: Estimation of corrosion current density, section loss and rust growth [16]

The corrosion rate of reinforcement is based on Faraday's law, amount of steel dissolving and forming hydroxide/oxide [62]:

$$m = i \cdot t \cdot a/n \cdot F \tag{2.4}$$

where m is mass of iron per area dissolved at the anode [g/m^2], i is electric current density [A/m^2], t is time [s], a is atomic mass of iron 55.8 g/mol, n is number of electrons liberated in the anodic reaction [2 for Fe = Fe^{2+} + 2e$^-$], F is Faraday's constant 96487 C/mol.

Taking the mass density of iron to be 7.87 kg/dm^3, the Faraday's law can be expressed as [62]:

$$V_{corr} = 11.6 \cdot i_{corr} \tag{2.5}$$

where V_{corr} (x_{corr}) is corrosion rate [μm/year] and i_{corr} is corrosion current density [μA/cm^2]. Other types of corrosion rate models will be described in Section 2.7.4.

Corrosion rate can be determined by various non-destructive electrochemical techniques, they measure polarisation resistance R_P for calculation of corrosion current density according to Eq. 2.5.

The most common electrochemical techniques for determining the polarisation resistance are Galvanostatic Pulse Method (GPM) and Linear Polarisation Resistance (LPR). The GPM provides polarisation resistance by change of potential due to small current pulse (galvanostatic puls) which is sent to the steel. The LPR method applies the very small voltage change (typically less than 30 mV) to the steel near to the rest potential. Relationship between applied voltage and the current response is linear. Calculation of polarisation resistance is based on Ohm's law [62]:

$$R_P = \frac{\Delta E}{\Delta I} = \frac{B}{I_{corr}} \tag{2.6}$$

where ΔE is the impressed potential and ΔI is the current response. B is constant [V] and the corrosion current $I_{corr} = B/R_P$ [62]:

$$i_{corr} = \frac{I_{corr}}{A} = \frac{B}{R_P A} = \frac{B}{A}\frac{\Delta I}{\Delta E} \tag{2.7}$$

where A is area of the steel bar that has received the impressed signal.

2.2.3 Depassivation as a start of corrosion

When steel reinforcement is placed in concrete of high pH and exposed to oxygen and moisture, it does not corrode due to the protective oxidation layer. This surface oxidation layer is provided by the corrosion reaction (Section 2.2.1) with very low corrosion current density. Taking Eq. 2.5 as a reference, the corrosion rate corresponds approximately to 0.1 μm/year, which maintains a passivating film on the surface.

After the passivation has been lost, electrochemical reactions are governed by chemical thermodynamics [62]:

$$E = \frac{-\Delta G}{nF} \tag{2.8}$$

where E is electrochemical potential [J/As = J/C = Nm/C = kgm^2/Cs^2 = V], ΔG is Gibbs free energy of reaction [J/mol], n is number of electrons transferred during the reaction [2 for Fe = Fe^{2+} + 2e$^-$], F is Faraday's constant 96487 C/mol.

The voltage attributed to a corrosion cell is given by:

$$E_{cell} = E_{cathode} - E_{anode} > 0 \tag{2.9}$$

Eq. 2.9 is further modified to Nernst equation, containing changes of the electrochemical potential, E, by different temperatures and concentrations (activities) of the species involved in the reaction [62]:

$$E_{cell} = E^0_{cell} - \frac{RT}{nF}\ln\frac{[Fe^{2+}][OH^-]^2}{\sqrt{p_{O_2}}} \tag{2.10}$$

where E_{cell} is electrochemical voltage (potential difference) of the corrosion cell [V], E^0_{cell} is electrochemical voltage of the corrosion cell in the standard state (i.e. temperature = 25°C, concentrations (activities) = 1), R is gas constant 8.314 JK^{-1} mol^{-1}, T is temperature [K], n is number of electrons transferred during the reaction [2 for Fe = Fe^{2+} + 2e$^-$], F is Faraday's constant 96487 C/mol, $[Fe^{2+}]$ is concentration of Fe^{2+} in the electrolyte adjacent to the steel surface [mol/l], $[OH^-]^2$ is concentration of OH$^-$ in the electrolyte adjacent to the steel surface [mol/l], p_{O_2} is partial pressure of oxygen in the electrolyte adjacent to the steel surface [Pa].

Eq. 2.10 can be used to construct a Pourbaix diagram that describes the surrounding conditions under which metal corrosion occurs, Fig. 2.2. This diagram describes three region types on the metal surface [62].

- The first one represents immunity region, where metal is thermodynamically stable and immune to corrosion (solid iron).
- The second one is corrosion region, where metallic iron (aqueous solution of ion Fe^{2+} and Fe^{3+}) corrodes.
- The third one is passivity region, where corrosion of solid ferrous oxide Fe_2O_3 and solid oxide Fe_3O_4 creates passive film which may protects the steel from further oxidation.

Transition from passive state to corrosion occurs when the protective passive film is destroyed. The corrosion starts if

- pH level of concrete drops below value 9 due to carbonation
- or the concrete in contact with the reinforcement contains critical value of dissolved chloride ions.

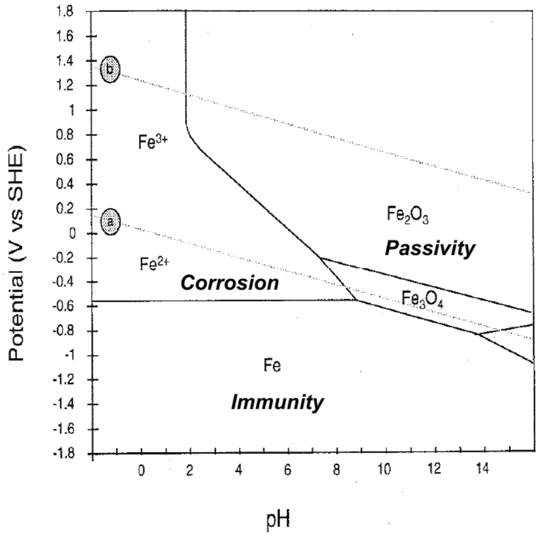

Figure 2.2: Pourbaix diagram for iron in water with three zones given by pH and potential [82]

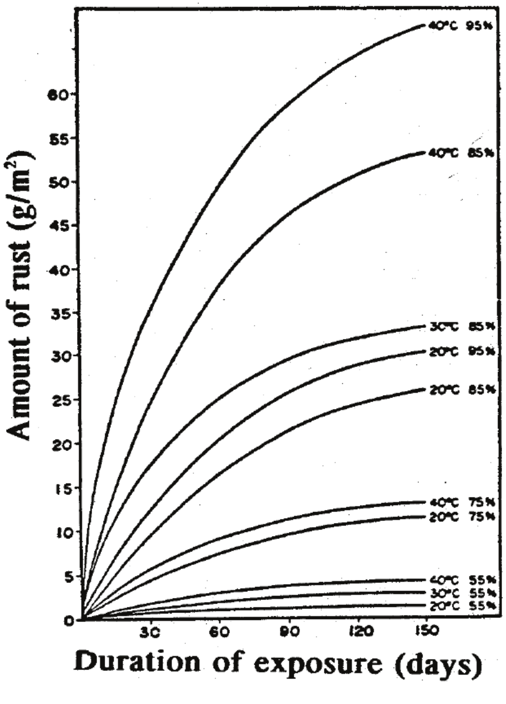

Figure 2.3: Effect of temperature and relative humidity on the amount of formed rust [80]

Process of dissolving of iron is directly affected by the temperature and by the oxygen supply which depends on P and RH. As mentioned, absence of water stops corrosion. Fig. 2.3 shows the effect of temperature and relative humidity on rust formation in carbonated concrete.

There are several types of corrosion, such as uniform, pitting, crevice, or galvanic. The most common corrosion observed in reinforced concrete is due to carbonation (uniform type) and chloride ingress (pitting type).

2.2.4 Uniform corrosion

Uniform corrosion belongs to the most widespread form of steel corrosion, characterized by corrosive attack over large areas, shown in Fig. 2.4. Uniform corrosion in concrete starts with decreased pH value under approximately 9 and is characteristic for carbonation. There is no separation of the anode and cathode. In the presence of excessive amounts of chloride a large number of very closely situated pits may form and cause an almost uniform and even attack over the entire steel surface [62].

Figure 2.4: Comparison between steel rebar corroded by natural carbonation a) and artificial carbonation b) [85].

2.2.5 Pitting corrosion

Pitting corrosion is caused by depassivation of a small area (typically a few square centimetres or even square millimetres), that leads to the creation of small holes (pin holes) on a metal surface, see Fig. 2.5.

Figure 2.5: Steel rebar corroded due to chloride ingress [67]

The mechanism of initiation of point corrosion is based on the attack of metal in places with weaker protective passive layer. The local dissolution of iron works as an anode and surrounded large area of passive steel acts as an cathode, depicted in Fig. 2.6. Pitting corrosion is typical for chloride induced corrosion [62].

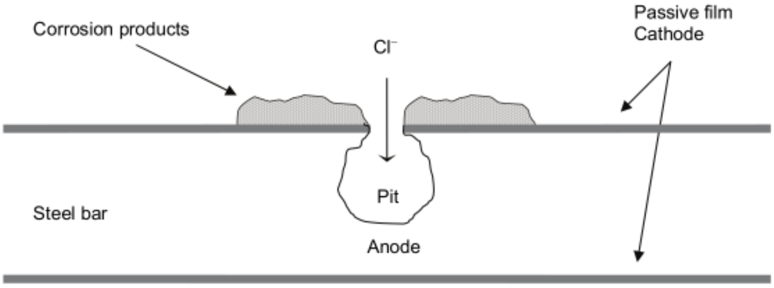

Figure 2.6: Chloride-induced pit formation on steel [62]

Pitting corrosion is considered to be more dangerous than uniform corrosion because it is more difficult to predict.

2.2.6 Factors affecting steel corrosion in concrete

The concrete cover forms a barrier and protection against aggressive agents. pH value decreases by the penetration of atmospheric CO_2 and ingress of chloride ions. Scheme of protective concrete cover shows Fig. 2.7. Once the limit values are reached, the reinforcement protective layer is broken down and the corrosion happens.

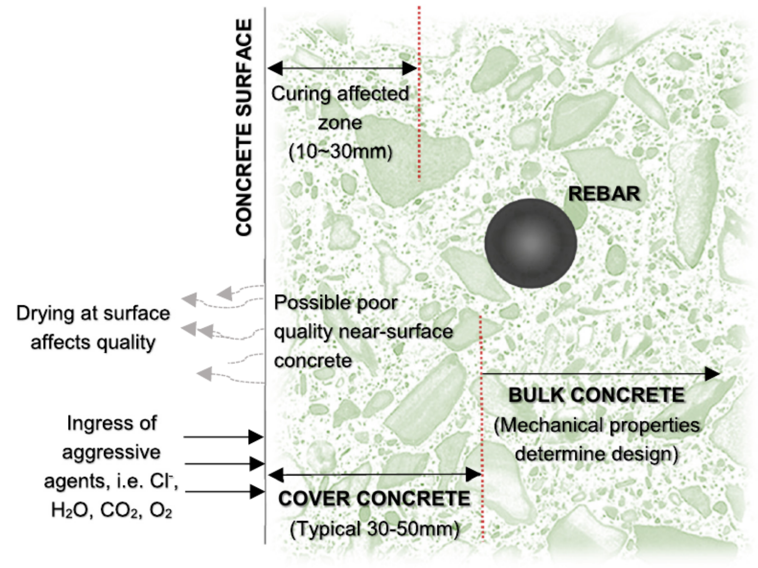

Figure 2.7: Concrete cover with physical processes [2]

Durability of reinforced concrete is mostly affected by the quality of the concrete cover layer. It is affected by several factors, e.g. mix ingredients and proportions, compaction, early-age drying affecting crack formation, or curing. The presence of cracks rapidly accelerates penetration of environmental agents through the concrete cover.

Penetration rate of oxygen depends on concrete porosity P, the temperature T and the degree of moisture content in pores RH. High P and T increase diffusion and oxygen supply. The moisture content has the highest impact on oxygen supply [15]. In fully submerged structures the supply of oxygen is so low that the corrosion rate becomes very low, even in the presence of high chloride concentration. The fastest oxygen penetration occurs under RH 50-70%.

The chlorides contained in the cement paste are divided into dissolved and bounded chlorides [62]:

$$C_{Cl,total} = C_{Cl,dissolved} + C_{Cl,bound} \tag{2.11}$$

The ability of chloride to dissolve is influenced by external source, temperature T, pH, moisture content RH and the ability of the cement (C_3A) to bind chloride to calcium chloroaluminate form [73]. These chemically bounded chlorides Cl_{bound} already does not contribute to corrosion of reinforcement.

The concentration of dissolved chlorides, $\mathrm{Cl}_{dissolved}$ increases with decreasing pH. This allows better dissolution in carbonated concrete. Consequently, carbonation increases corrosion due to chlorides.

2.2.7 Transport processes in concrete

Concrete is a porous, heterogeneous medium, consisting of a binder, filler, water, additives and admixtures. The level of penetration of harmful substances is given by the amount, type, size and arrangement of pores in cement paste, which affects the strength, deformation, permeability, shrinkage and creep. The free water content in the pores also plays an important role. The transport of gases, liquids and ions lead to a gradual deterioration of concrete. These transport processes describe diffusion, absorption or penetration of pollutants.

Transport processes occurs mostly through capillary pores, at the interface of aggregate and cement paste, and through micro-cracks. Concrete is an aging material, porosity decreases due to hydration of cement paste as well as the interconnection of capillary pores decreases with time. On the other hand, the formation of micro-cracks may increase due to the shrinkage. Therefore, the transport properties of concrete vary with time, especially when the transport properties of young concrete are measured [49].

In the real structures, several transport processes take place simultaneously; diffusion, capillary suction, general migration, etc. Basic processes are described further, together with relevant parameters.

2.2.7.1 Diffusion

Brownian motion causes movement of free atoms, ions, or molecules from an area with a higher concentration to a lower concentration. The flow, q, is expressed by Fick's first law of diffusion for 1D:

$$q = -D\frac{dC}{dx} \tag{2.12}$$

where D is diffusion coefficient [m^2/s] for flow in the direction of a negative concentration gradient, hence a negative sign. The concentration C depends on phases in which the transport takes place, e.g. the amount of gas molecules on the total volume of gas or the amount of dissolved ions in the total liquid volume etc. Fick's first law of diffusion is in its general form valid for every point in time and space during the diffusion [49].

Applying the first Fick's law of diffusion to transport processes leads to a mass balance equation, describing the change in concentration in a unit of volume over time. This relationship is usually referred as Fick's second law of diffusion in 1D. This equation is often used to determine the concentration profiles:

$$\frac{\partial C}{\partial t} = D\frac{\partial^2 C}{\partial^2 x} \tag{2.13}$$

Other transport affecting phenomena:

- Capillary suction - for porous materials such as concrete, fluids can flow even without external pressure. This is due to the surface forces of liquid and solids (capillary forces) that transport fluid to the capillary pores. Repeated wetting and drying can cause changes in the porous system and expansion of cement filler [49].

- Migration - penetration of ions into concrete is generally referred to a diffusion process, where the transport of a substances and an electric charge occurs. In order to maintain the electroneutrality of the system, the flow of anions must be balanced by an adequate cation flow. If the charge transfer is not balanced, the voltage difference increases and an electric field is created, consequently ions spread in the liquid. Attention is paid to the spread of chloride ions in concrete pores with different ion types.

2.2.7.2 Permeability

Water and air permeability of concrete surface layer is one of the most important indicators of the concrete durability [88]. With a higher number of pores, the permeability of concrete for water and gases increases.

The properties of the porous material with respect to permeability are controlled by two factors: open porosity (interconnection, depicted in Fig. 2.8) and pore size distribution. According to the size and origin of pores, three types are distinguished [109]; macropores with the diameter above 10^{-3} m, capillary pores 10^{-5}–10^{-7} m and micropores with diameter 10^{-7}–10^{-9} m.

For low permeability concrete, the capillary pores are the most important, through which the water passes under a pressure gradient. The size of these capillary pores depends primarily on the amount of excess water. If w/c ratio is greater than 0.42, the capillary pore volume increases significantly, thus permeability increases too [114]. Under the effect of an absolute pressure gradient, liquids and gases can infiltrate through a system of connected pores and cracks of cementitious material.

Air permeability is determined by the equation based on the Hagen-Poiseuille law, on the assumption of laminar air flow in the capillaries of element [49]:

$$k = \eta\frac{Q}{t}\frac{L}{A}\frac{2p}{(p_1 - p_2)(p_1 + p_2)} \tag{2.14}$$

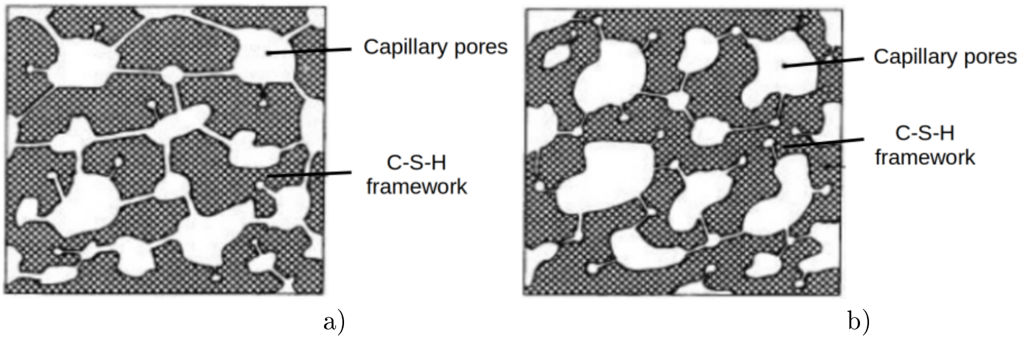

Figure 2.8: High permeability - capillary pores interconnected a), low permeability - capillary pores separated and only partially connected b) [84]

where k is air permeability coefficient [m^2], η is gas viscosity [Ns/m^2], Q is volumetric flow rate [m^3/s], t is time [s], L is gas penetration depth [m^3], A is permeated area [m^2], p is a pressure at which Q is measured [Pa], p_1 is entry gas pressure [Pa], p_2 is output pressure [Pa].

Water permeability can be described by water flow through a saturated porous material, which obeys D'Arcy's law:

$$\nu = -k\frac{\Delta p}{L} = -k\rho g\frac{\Delta p}{\rho g}\frac{1}{L} = -K_p\frac{\Delta P}{L} \tag{2.15}$$

where ν is the velocity of the water [m/s], K_p is the permeability coefficient [m/s], p is the hydraulic pressure exerted by the water [Pa], P is pressure potential $= p/r/g$, L is the specimen length [m].

For the hardened cement paste (w/c=0.3–0.7), permeability lies between 0.1–120$\cdot 10^{-14}$ m/s, for coarse aggregate ranges between 1.7–3.5$\cdot 10^{-15}$ m/s, high strength concrete 1$\cdot 10^{-15}$ m/s, for mature, good quality standard concrete 1$\cdot 10^{-12}$ m/s [93].

2.2.7.3 Crack formation in concrete

As mentioned before, cracks and microcracks in concrete have a major effect on the water permeability. The permeability increases with the amount and opening of micro-cracks in the transition zone, at the interface between cement paste and aggregate, also with the size of the aggregate [65], see also Fig. 2.9.

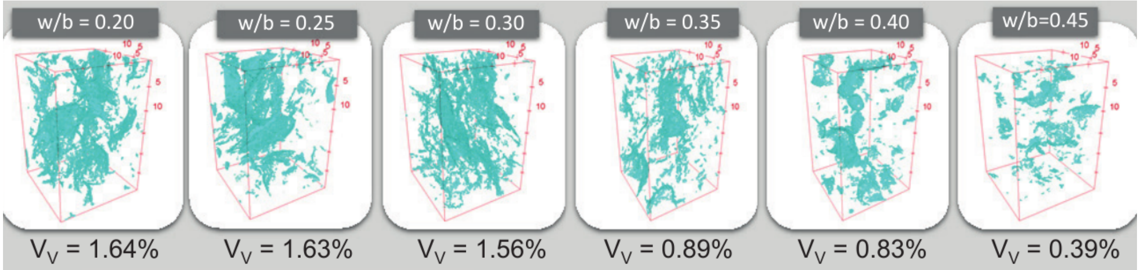

Figure 2.9: Effect of w/b ratio on the amount of microcracks in sealed mortar sample, aggregate 68% vol., sample volume 21× 21× 30 mm [60]

Cracks may develop during plastic shrinkage, $\varepsilon_{sh,pl}$, in the fresh concrete (beginning of hardening) due to rapid volume changes. Especially with a high w/c ratio, water evaporates quickly with substantial volume changes. High ambient temperature, wind and sun radiation contribute to evaporation. The cracks can be eliminated by the placement of fresh concrete, its compaction and proper treatment.

During the hardening of the concrete; cracks may occur due to thermal expansion/contraction caused by hydration heat and subequent cooling, from the autogenous $\varepsilon_{sh,au}$ and chemical shrinkage ε_{chem} caused by volume reduction of the components involved in the chemical reactions during hydration, Fig. 2.10.

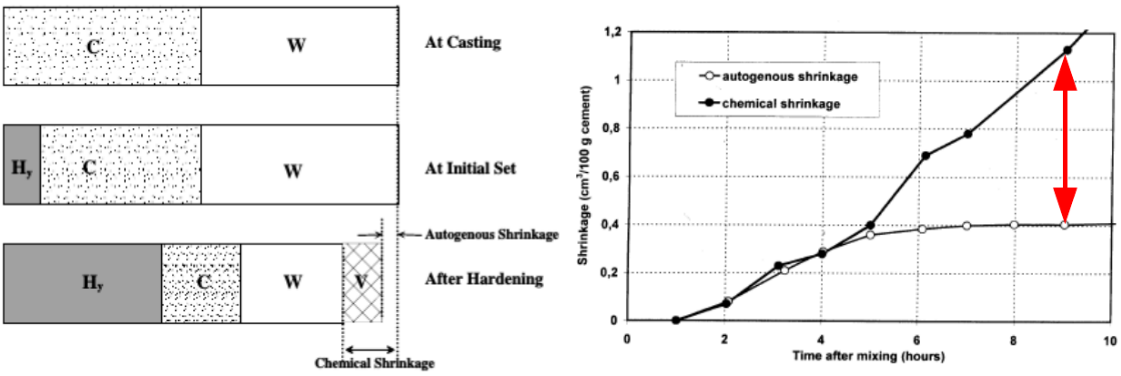

a) b)

Figure 2.10: Autogenous and chemical shrinkage [39] a), evolution of autogenous and chemical shrinkage [39] b)

Furthermore, there is drying shrinkage caused by moisture loss $\varepsilon_{sh,s}$, depicted in Fig. 2.11. Conversely, the creep of concrete mitigates shrinkage effect on stress and cracks [49].

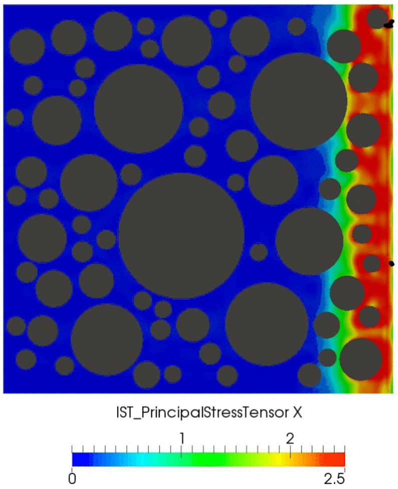

Figure 2.11: Mesoscopic model: crack evolution from drying shrinkage only (creep and damage model) [93]

Other cracks are related to external loading and serviceability limit state.

2.3 Carbonation

Carbonation occurs mainly due to presence of carbon dioxide in the air. CO_2 in the gaseous phase penetrates to concrete pores and reacts with calcium hydroxide in the presence of water or moisture. Consequently, the concentration of OH-ions in the cement mass is reduced and conditions for reinforcement corrosion are created. This diffusion-driven process is shown in Fig. 2.12 and described as follows:

$$Ca(OH)_2 + H_2O + CO_2 \rightarrow CaCO_3 + 2H_2O \tag{2.16}$$

The dissolved portlandite $Ca(OH)_2$ in pore water reacts with dissolved CO_2. Furthermore, carbon dioxide CO_2 reacts with hydrated calcium silicate CSH and various modification of calcium carbonate $CaCO_3$ arise.

The reaction speed depends greatly on the porosity and the presence of cracks in the concrete. Acceleration of carbonation around a macrocrack is shown in Fig. 2.13a).

Calcium carbonate settles in the pores and capillaries and gradually fills them. In case of concretes with lower porosity, the products fill the pores at surface layer, permeability is reduced

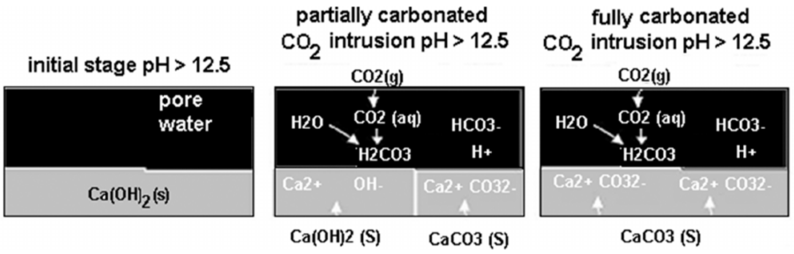

Figure 2.12: Ion dissociation phenomena of carbonation [96]

and prevent further ingress of carbon dioxide. In the case of concrete with higher porosity, the pores and capillaries do not fill sufficiently and carbonation continues to the reinforcement.

During carbonation, pH of the surface layer is reduced. Carbonation reduces initial pH value about 11 and higher (in which the concrete reliably acts as a protection against corrosion of the steel reinforcement) to a value of 9 and lower. If the carbonation front reaches the steel reinforcement, rapid corrosion occurs.

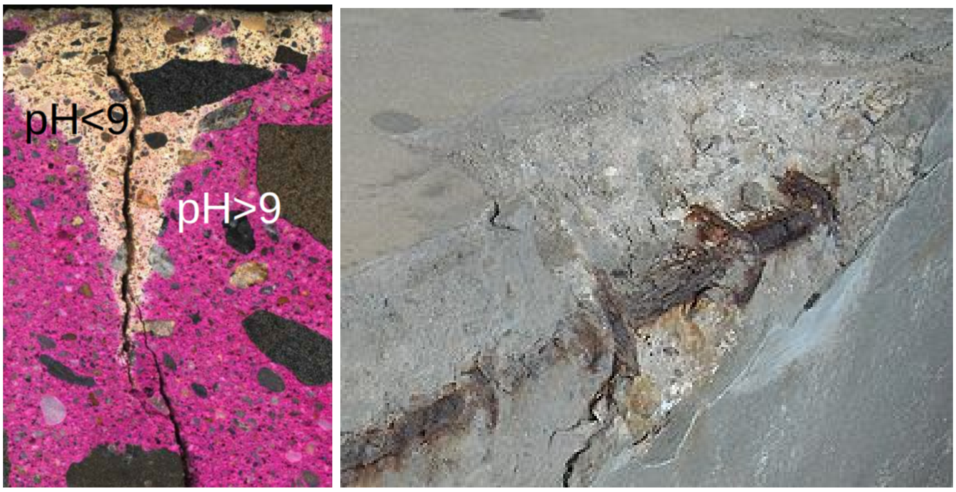

a) b)

Figure 2.13: Accelerated carbonation due to macrocrack [35] a), spalling of concrete cover [119] b)

Corrosion products have several times higher volume than the original steel, which causes the destruction of concrete surface, cracking, spalling of concrete cover and exposure of the reinforcement, causing corrosion in direct contact with the environment, see Fig. 2.13b). These processes take place first mainly in the areas of cracks and poor quality concrete with pores and caverns.

The main factors affecting concrete carbonation are the type and the content of binder, w/b ratio, the degree of hydration, the concentration of CO_2 and relative humidity, fastest under RH 50–70%, see Fig. 2.14. The rate of carbonation is also affected by alkali content, the type of cement, the fineness of the materials, temperature and the presence of cracks.

2.4 Chloride ingress

Steel corrosion due to chloride ingress occurs in chloride-containing environments such as de-icing salts, sea water and salts in coastal areas. Chloride penetrates through the concrete cover to steel. When concentration of chlorides in the place of reinforcement reaches the threshold of critical value, the corrosion starts. The critical concentration $C_{cl,cr}$ value plays an important role here, typically a value 0.6 % of binder mass [116, p. 72]. Chloride ions diffuse through the binder in concrete and the ingress is controlled by several factors such as a concrete cover thickness, chloride binding, chloride mobility, steel interface, cementitious binder (type of binder, C_3A content, pH), concrete barrier (cement type, amount of cement, w/b ratio, curing, concrete cover), and environmental

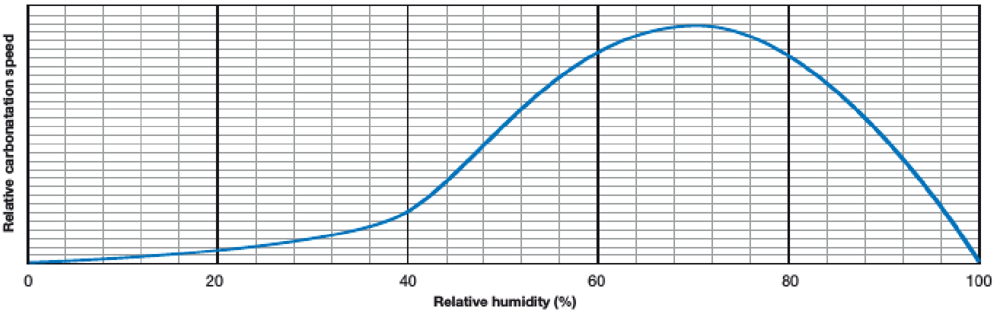

Figure 2.14: Carbonation rate strongly depends on relative humidity [98].

boundary conditions (relative humidity, temperature, chloride type). An example of corrosion caused by chloride ingress is shown in Fig. 2.15.

Figure 2.15: Corrosion of reinforcement attacked by sea water [117]

As in the case of carbonation, corrosion products cause the destruction of concrete surface, cracking, spalling of concrete cover and exposing the reinforcement to direct contact.

2.5 Durability design

Durability design of RC structures should ensure that the structure, as-built and in its design environment (exposure conditions), can withstand various aggressive influences over its design life, justifying the economic investment and satisfying the serviceability requirements. In essence, durability design involves selecting an appropriate combination of materials and structural details to ensure durability (serviceability) of the structure [3].

The most current deterministic approach provides single value answers [3]. Current specifications are largely prescriptive, obsolete and unsuitable for modern materials. They were created at previous period when durability was not considered as a critical issue. Compressive strength was taken as the main indicator that describes all the important properties of concrete, including durability.

2.5.1 Prescriptive specifications

These specifications provides methods, processes and limitation for binder content, compressive strength, w/c ratio, etc. [2] The European Standard [29] adopts a deemed-to-satisfy approach. Works with various environmental exposure classes, prescribed maximum w/c ratio, and minimum compressive strength class and cement content. It assumes that the supplied concrete has the same durability properties as the concrete in the realized construction. The approach restricts the use of innovative techniques and new concrete, it also does not contain clear details about exposure conditions and is not very verifiable in practice. In this case, only the strength of the concrete is verified by measurement.

2.5.2 Performance-based approach

This approach represent more innovative method, used for modern materials, with a greater weight on the concrete performance. It is based on measurement of properties related to durability in realized structures together with inspection and maintenance plans. Approach allows modelling and prediction of structure service life together with the probabilistic assessment of the relevant material parameters, aggressivity of environment and degradation processes [2].

As we mentioned, durability is given by quality of the concrete cover, therefore, transport properties have to be measured. RILEM [109], [13] presents appropriate tests methods that determine the concrete's resistance to chloride ingress (e.g. NT BUILD 443, NT BUILD 492, ASTM C1556 for carbon dioxide (accelerated carbonation chamber) [2].

2.6 Service life design

Service life of a concrete structure according to fib Model Code is defined as "the assumed period for which a structure or part of it is to be used for its intended purpose with anticipated maintenance but without major repair being necessary." [34]

Service life design combines economic, 'safe' and durability requirements [55].

For example, Walter introduces several elements for the successful application of performance based service life design [115]:

- limit state criteria,
- a defined service life,
- deterioration models,
- compliance tests,
- maintenance and repair strategies, and
- quality control systems

"Limit state criteria for structural performance in regard to durability should have clear physical meaning such as percentage of cracking or loss of surface. Deterioration models, which are generally mathematical, are useful for designers only if the model parameters conform to the performance criteria that are used. Thus, the key model parameters should be measurable in site-practice, implementable in construction, and incorporated into the project specifications such that they are verifiable on site. There are very few such approaches in practice presently." [2]

The following sections present performance based standards and codes dealing with durability, such as the fib Model Code for Service Life Design (fib Bulletin 34 [34]), fib Model Code 2010 [34], ISO 13823 [41], Eurocode 2 (EN 1992-1:2004).

2.6.1 ISO 13823

This standard describes four service life design approaches and works with limit state methodology, see Fig. 2.16; the full probabilistic approach, partial safety design (semi-probabilistic approach), avoidance of deterioration and deemed-to-satisfy approach. The concept is based on loading by environmental conditions and ability of concrete to resist them [2]. The same design criteria are used in the fib Model Code for Service Life Design [34].

The full probabilistic and partial safety design uses limit state theory, with three limit states. The ultimate limit state (ULS) for safety and stability design, the serviceability limit state (SLS) is the design to ensure a structure is comfortable and useable. This includes vibrations, deflections, as well as cracking. Durability limit state (DLS) express durability failure, e.g. corrosion initiation, cracking of concrete cover, etc.

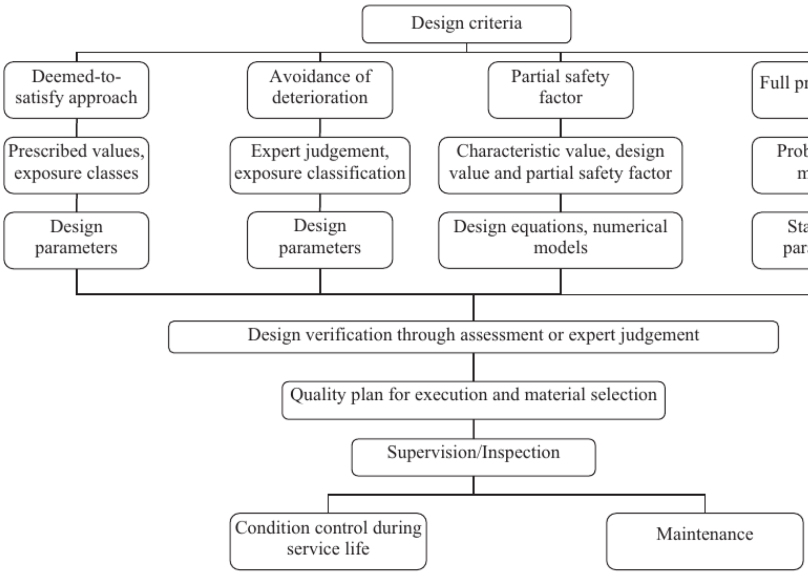

Figure 2.16: Summary of service life design approaches [41]

- The **full probabilistic method** is based on probabilistic models for deterioration and material resistance (Fig. 2.17) [2]. The basic idea of quantifying the reliability of a structure is to estimate the probability of failure, which is a reliable indicator of structural reliability. Until reaching the limit value (Limit probability value P_f), the time dependent resistance $R(t)$ of the structure should by larger than the target design requirements $S(t)$ (loading):

$$P_f = P[R(t) - S(t) < 0] \leq P_{target} \tag{2.17}$$

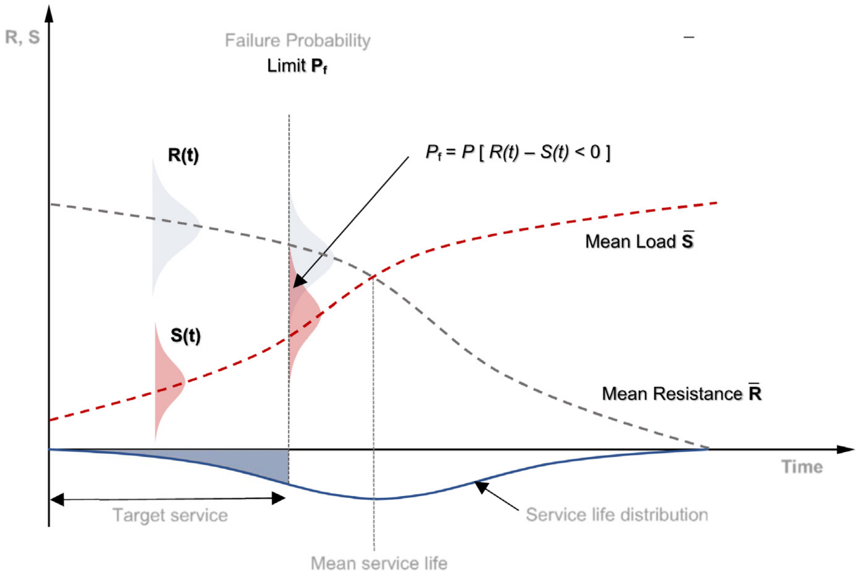

Figure 2.17: Scheme of probabilistic service life design. Adopted from ISO 13823 [41]

The full probabilistic design is best suited to the performance approach, but is still rarely used in practice. However, the approach requires validation to obtain reliable and realistic results.

- The **partial factor design approach**, uses statistically derived partial factors for the various random variables (dimensions, nominal properties), to obtain design values and ensure more practical and reliable design. These partial factors and design values are in principle evaluated on the basis of probabilistic method.

- In the **avoidance of deterioration approach**, we want to prevent concrete and steel degradation, using of stainless steel or protection coatings, etc. Therefore, it is necessary to assess each structure individually. However, some maintenance is still necessary, for example, restoring the anti-corrosive coating.

- The **deemed-to-satisfy approach** is conceptually similar to current prescriptive durability specifications, based on selection of design values (e.g. dimensioning, material and product selection, execution procedures) [2]. The difference between these approaches, the ‘deemed-to-satisfy’ approach is based on physical and chemical models for concrete, it is more ‘performance-based’ approach. These design values should also be calibrated using a fully probabilistic approach to ensure reliable durability design rules and service life prediction. The conventional prescriptive design rules express only the practical experience. Design values are obtained either by statistical evaluation of experimental data or by calibration of existing data.

2.6.2 fib Model Code, DuraCrete model

The service life design procedure with these models is similar to the determination of the structure loading. For this reason, it is closer to structural design engineers. It uses a similar categories as ISO 13823 in Fig. 2.16: full probabilistic, partial factor design, deemed-to-satisfy, and avoidance of deterioration.

This method of designing uses carbonation, chloride and reinforcement corrosion models to obtain the major time limit states (depassivation, cracking or spalling of concrete cover, and collapse). Using presented prediction models, the engineers are able to design appropriate material parameters and concrete cover to the specified resistance level. For deterioration modelling, material parameters such as carbonation resistance and chloride ingress are needed. This data can be obtained from a database of similar materials or by rapid chloride migration method and accelerated carbonation test, as mentioned above.

2.7 Service life modelling

The most current service life models for corrosion-affected RC structures adopt the two-stage service life modelling. Therefore, the service life is divided into two stages, initiation and propagation, see Fig. 3.2. The initiation period is the time during which the contaminants (carbon dioxide or chlorides) are transported through the concrete cover layer to the reinforcement. This phase ends by the depassivation of the reinforcement, i.e. the beginning of the corrosion process that occurs after reaching a critical thresholds. The length of this stage depends on the quality and thickness of the concrete cover, the presence of cracks, and the aggressivity of the environment. Reinforcement corrosion takes place during the propagation period, and its rate is governed by the availability of water and oxygen on the steel surface. Two main types of corrosion are presented - uniform (general, typical for carbonation) and pitting (localized, typical for chlorides).

Fig. 3.2 shows stages during propagation period leading to structure collapse, such as cracking of concrete cover due to expanding corrosion products and spalling of the concrete cover, often considered as the end of serviceability, followed by ultimate collapse of the structure [2].

The growth of corrosive products and the evolution of cracks are described in the Fig. 2.18. Process ends by spalling of concrete cover and direct reinforcement corrosion.

2.7.1 Carbonation and chloride ingress-induced corrosion models

A few probabilistic models developed in 1980’s consider only uncracked concrete [42], [43]. Currently, there are several practical service life models predicting the chloride and carbon ingress, such as the DuraCrete model [72], the more realistic ClinCon model which decomposes chlorides into free and bound components [104], LIFE-365 based only on computer simulations [56], DuraCon [36], or the STADIUM model [100] as a reactive transport model. The Mejlbro-Poulsens model [74] assumes the concentration gradient as the driving force, operating on a time-dependent chloride concentration and diffusion coefficients. Kwon proposed models with acceleration of carbonation and chloride ingress due to crack presence [52], [51].

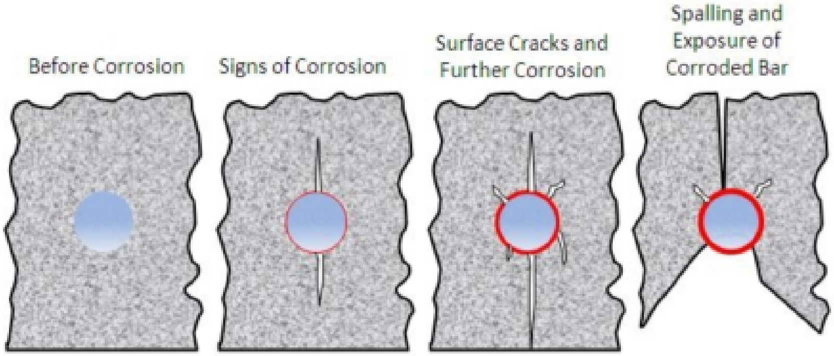

Figure 2.18: Crack evolution [18]

Apart from the LIFE-365 model, the mentioned practical models are based on the information about the concrete mix properties and proportions, on the relevant diffusion coefficient of concrete and environmental conditions, using Fick's law to obtain the representative chloride profiles, formulated in 1855 by Adolf Fick, Eq. 2.13.

For example, one of the existing models using the 1D Fick's second law, under the assumption of constant chloride content at surface and initial zero chloride content, is the following [74]:

$$C(x,t) = C_s \left[1 - erf\left(\frac{x}{2\sqrt{D_m t}}\right)\right] \tag{2.18}$$

where $C(x,t)$ is the chloride concentration at depth and time, C_s is the surface chloride concentration, D_m is averaged diffusion coefficient to the time t, t is the time for diffusion, x is the depth and erf is the statistical error function. Constant surface chloride concentration and diffusion coefficient are considered in the Eq. 2.18, but it is known that they are variable over time as discussed further.

The length of the induction period is strongly influenced by the choice of two parameters, the critical chloride threshold value $C_{Cl,crit}$ and the surface chloride concentration $C_{Cl,s}$. In the case of carbonation models, the effective carbonation resistance of concrete is crucial, measured by accelerated carbonation tests.

$C_{Cl,crit}$ is very variable parameter and influenced by many factors that affects corrosion initiation, such as moisture content, cement composition, temperature and w/c ratio [121], it is related to ability of chloride binding capacity of the cement paste. Angst [6] recommends measuring of critical thresholds directly on site to ensure the most realistic results. The most common expression of the critical thresholds is follows: % chloride by weight of cement, weight per unit concrete, and chloride to hydroxyl ratio [77].

Articles from Shakouri [91] and Petcherdchoo [81] deal with the fact that the $C_{Cl,s}$ value should be taken as a time dependent variable. Kassir and Ghosn completed investigation ot the effect of the variable chloride concentration on predicted service live, difference in some cases can be much as 100%. The chloride concentration increases over a time period and then becomes almost constant, according to the data provided by Weyers [118] but most of the models, currently in use, work with a constant value used in the Fick's equation [121].

2.7.2 Other Fick's diffusion chloride models

Cady and Weyers [17] proposed deterministic model, used for the initial estimation of the bridge decks service lives. Chloride ingress is estimated through Fick's second law and considers constant diffusion.

Mangat and Molloy [61] model includes time-depended diffusion parameter, yielding another parameter:

$$C(x,t) = C_0 \left[1 - erf\left(\frac{x}{2\sqrt{\frac{D_i}{1-m}^{(1-m)}}}\right)\right] \tag{2.19}$$

Empirical relationship for the diffusion is:

$$D_c = D_i t^{-m} \tag{2.20}$$

where D_c is effective diffusion coefficient at time t [cm^2/s], D_i is effective diffusion coefficient at time t equal to 1 second, t is the time [s] and m is empirical coefficient that varies with mixture proportions [m=2.5(w/c)-0.6]

Bamforth [7] presented a diffusion model that accounts for a time-dependent diffusion similarly as Mangat and Molloy model [61]. The concentration solution has a form:

$$C(x,t) = C_0 \left(1 - erf \left(\frac{x}{2\sqrt{\left[D_{ca(tm)} \left(\frac{t}{t_m} \right)^n t \right]}} \right) \right) \tag{2.21}$$

where $D_{ca(tm)}$ is an apparent diffusion coefficient measured at time t_m predicted at 1 year by the following:

$$D_{ca} = at^n \tag{2.22}$$

where D_{ca} is apparent diffusion coefficient, a=D_{ca} at t=1 year and n is an empirical constant.

Boddy et al. [14] developed a chloride transport model that contains the following parameters: initial chloride concentrations, initial diffusion value (D) for concrete, time-dependent reduction of D, nonlinear chloride binding isotherms, superposition of a hydraulic head on an external salt water environment, time-dependent surface concentrations and varying monthly temperatures [121]. This equation is used to determine the concentration profile:

$$\frac{\partial C}{\partial t} = D\frac{\partial^2 C}{\partial^2 x} - \nu\frac{\partial C}{\partial x} + \frac{\rho}{n}\frac{\partial S}{\partial t} \tag{2.23}$$

where C is "free" chloride concentration, S is "bound" chloride, D is diffusion coefficient, ρ is concrete density, n is porosity and ν is average linear velocity (calculated from flow rate Q, cross-sectional area A, hydraulic conductivity k and hydraulic gradient h)

2.7.3 Modelling of cracked concrete

Carbonation and chloride ingress-induced corrosion models usually do not allow to model the influence of crack width on the acceleration of these processes, but research shows that it is a major parameter that affects the length of initial period. All concrete contain cracks; early-age cracks, caused by hydration heat and drying shrinkage in massive members, which are not critical to the bearing capacity, but substantial to rapid reinforcement corrosion; and the progressive cracks caused by external loading. For example Ozbolt et al. [75] "investigated transport of capillary water, oxygen and chloride through concrete cover, immobilization of chloride in the concrete, transport of OH$^-$ ions through electrolyte in concrete pores, and cathodic and anodic polarization, using a 3-D numerical model based on continuum mechanics and thermodynamics (hygro-thermal-mechanical models) for damaged and undamaged concrete." Further, Kwon extends the carbonation and chloride ingress models for crack effect, described below [52], [51].

2.7.3.1 Modelling of carbonation in cracked concrete

In investigation of Kwon and Na [52], there were 27 RC columns exposed to carbonation for eighteen years in the urban area. The carbonation distribution was derived for three cases, sound, crack and joint concrete with crack mappings (cold joint occurs between two batches caused by delay in the placement of the second batch).

Their research considers only early-age cracks with a constant length and width because of the difficulty in considering of the crack opening and closing due to rehydration [96], [95].

The studied columns have been designed with the strength of 24 MPa and the concrete cover of 67.5 mm. The crack width was around 0.1∼0.2 mm, the cracks over 0.3 mm wide were repaired within the annual maintenance. "The concrete surface is pecked by chisel, and a phenolphthalein indicator of 1% concentration and digital calipers are used for measuring the carbonation depth based on JIS 1152" [52].

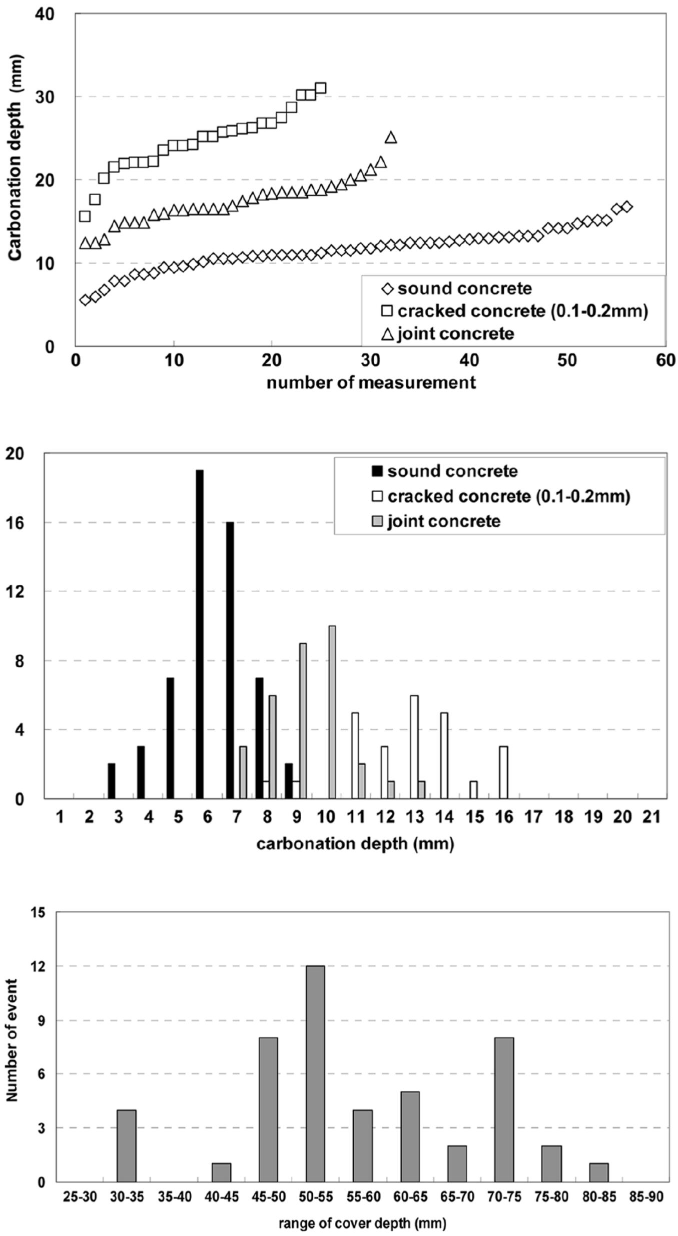

a)

b)

c)

Figure 2.19: Result of measured carbonation distribution. Carbonation depth and measurement number a), histogram of carbonation depth with different conditions b), histogram of cover depth c) [52]

The results of the research are reported in Fig. 2.19. "The average carbonation depth is measured to be 11.7 mm taken from sound concrete in 56 data-set, 24.6 mm from cracked concrete in 24 data-set (0.1∼0.2 mm of crack width), and 17.4 mm from joint concrete in 32 data-set, assuming that the carbonation depth is in proportion to the square root of the exposed time" [52].

The measured carbonation depths and their regression can be written by equations for unsound concrete (with crack and joint) Eq. 2.25, 2.26 and sound concrete Eq. 2.24, plotted in Fig. 2.20, [52]:

$$\text{Sound concrete: } C = 2.778\sqrt{T} \tag{2.24}$$

$$\text{Cracked concrete: } C = 5.808\sqrt{T} \text{ (crack width } 0.1 \sim 0.2 \text{ mm)} \tag{2.25}$$

$$\text{Joint concrete: } C = 4.092\sqrt{T} \tag{2.26}$$

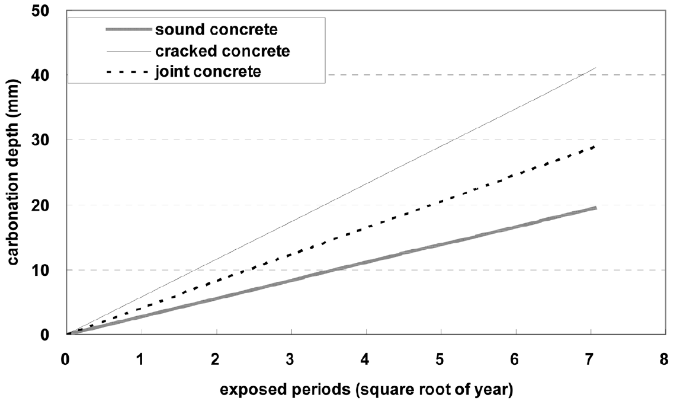

Figure 2.20: Carbonation depth with exposed period [52]

where C is carbonation depth [mm] and T is exposed period [year].

The described model works with assumption that carbonation depth is proportional to crack width $\sqrt{w}$, for the case of cracked concrete, Eq. 2.25 can be modified for averaged crack width as follows:

$$C = (2.816\sqrt{w} + 1)A_1\sqrt{T} \tag{2.27}$$

where w is crack width [mm] and A_1 is carbonation velocity in sound concrete according to Eq. 3.1. The more details in description of implemented cracked carbonation model in Chapter 3.1. The carbonation velocity for different crack width is plotted in Fig. 2.21.

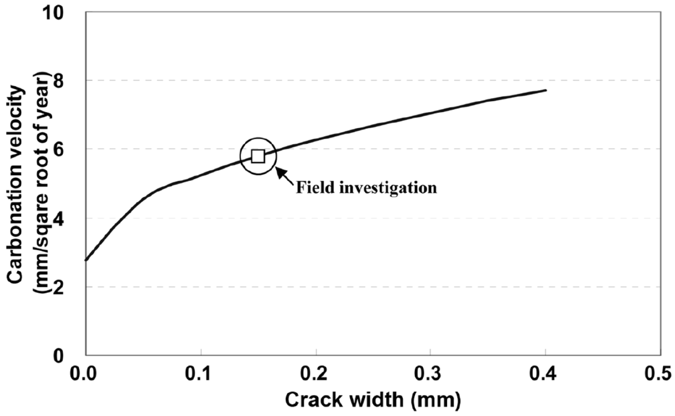

Figure 2.21: Carbonation velocity for different crack widths (18 years) [52]

2.7.3.2 Modelling of chloride ingress in cracked concrete

The effect of cracks on the diffusion and permeation of chloride has been investigated in several other studies, represented in these articles [108], [97], [95], [38] requiring further studies to specify the rules for their use.

The study of Kwon et al. [51] solves the influence of a crack on chloride diffusion. It was investigated at two different port wharves for 8 and 11 years, located at Inchon Port in South Korea, in 1995 and 1992. The crack effect was carried out for three crack widths; 0.1 mm, 0.2 mm and 0.3 mm. To avoid the influence of crack density effect, they used samples with a single crack. For each crack width, three concrete samples were taken from the concrete deck slab and used in test method AASHTO T 260 to obtain diffusion coefficient [51].

The early-age cracks are assumed to have a constant width across their length, originating from hydration heat and drying shrinkage. The progressive cracks due to collisions and rehydration are not considered [51].

Figure 2.22: View of wharf structures [51]

The following Figs. 2.23,2.24 show the measured chloride profiles, they show increasing concentration with larger crack width.

For each crack width three samples were taken from area with single crack only (to avoid the crack density effect) and without external loading. The measured data from each sample are shown with symbols and their average value by solid line.

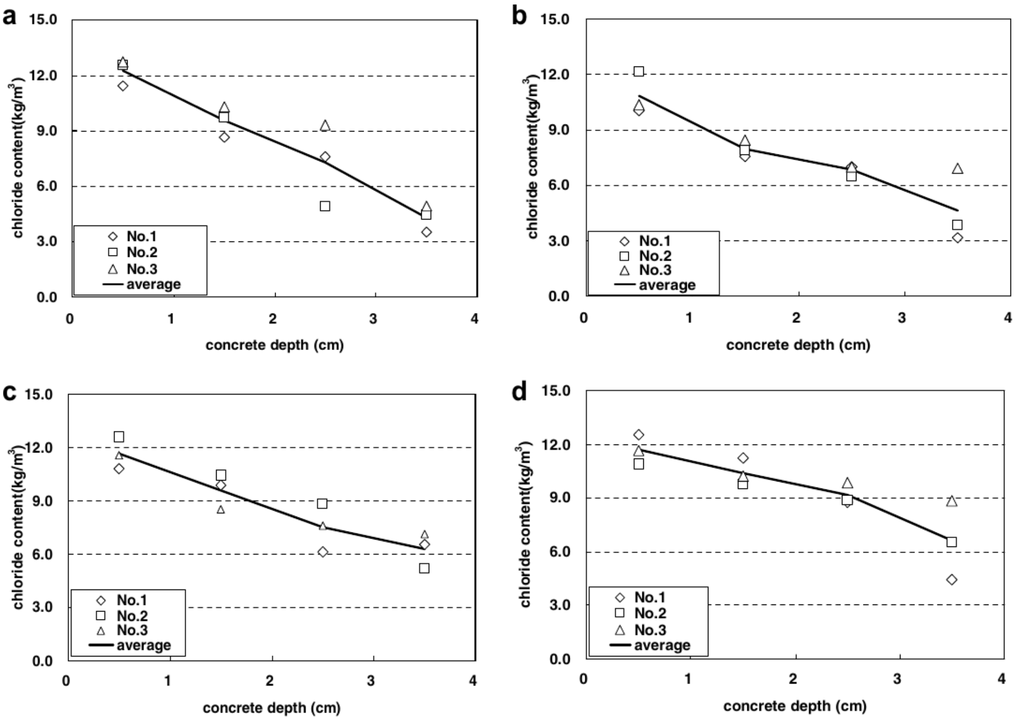

Figure 2.23: Measured chloride profiles in core samples after 8 years: Sound concrete a), 0.1 mm crack width b), 0.2 mm crack width c), 0.3 mm crack width d) [51]

The combination of averaged diffusion coefficients D_m (used in Eq. 2.18) with regression analysis of this field investigation yields the averaged diffusion coefficient $D(w)$ in a cracked concrete [51]:

$$D(w) = f(w) \cdot D_m \tag{2.28}$$

where $D_m(t)$ is the mean (averaged) diffusion coefficient at the time t [m^2/s] and $f(w)$ is a crack effect function:

$$f(w) = 31.61w^2 + 4.73w + 1 \ (w \geq 0.1 \text{ mm}, R^2 = 0.984) \tag{2.29}$$

Inserting the crack effect function Eq. 2.29 into Eq. 2.18 improves chloride diffusion model of cracked concrete Eq. 3.18, used and described in Section 3.2.3.

Relationship between crack width, chloride content and diffusion coefficient is plotted in Fig. 2.25

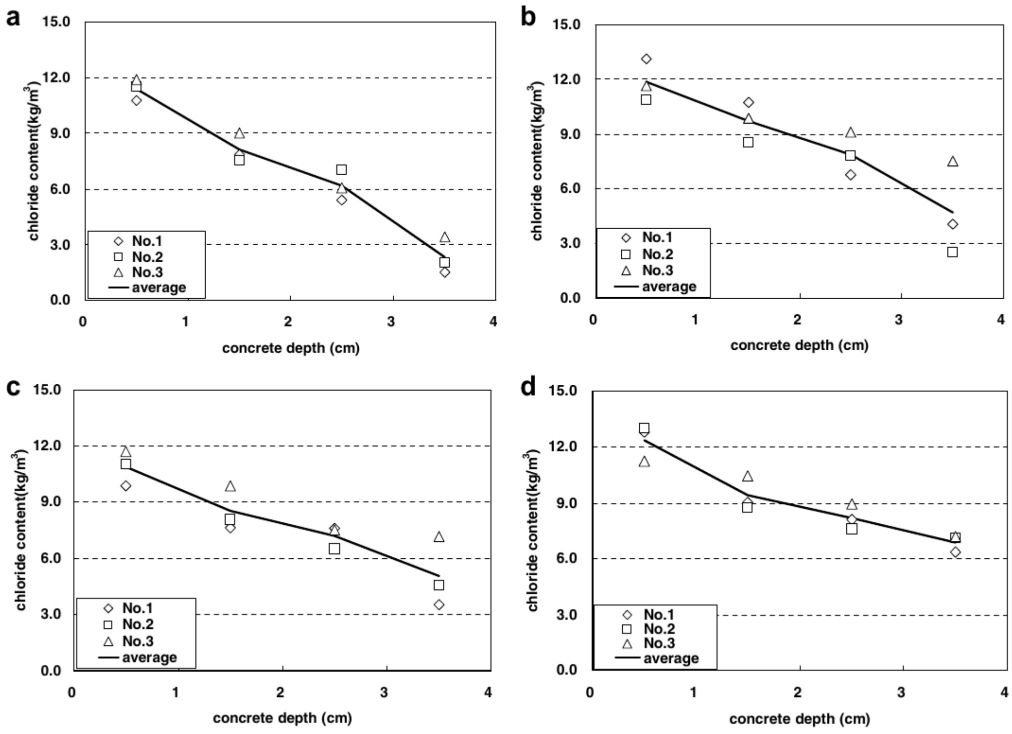

Figure 2.24: Measured chloride profiles in core samples after 11 years: Sound concrete a), 0.1 mm crack width b), 0.2 mm crack width c), 0.3 mm crack width d) [51]

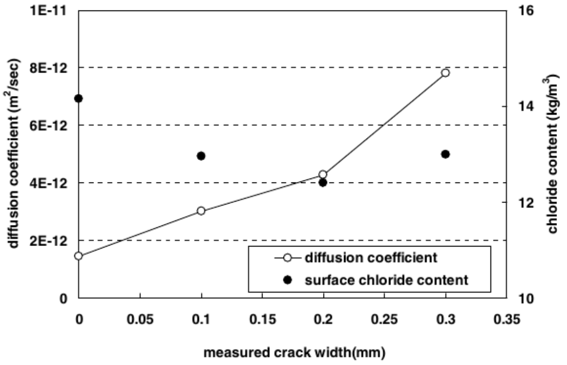

Figure 2.25: Measured relationship between crack width, chloride content and diffusion coefficient [51]

2.7.4 Modelling of reinforcement corrosion rate

Models presented in this chapter describe reinforcement loss during the propagation period, until the spalling od concrete cover. Three types of the corrosion rate models exist [62]:

- models based on electrochemistry;
- models related to a diffusion-limited access of oxygen;
- models in the form of empirical relations (e.g. based on electrical resistivity of the concrete)

Models based on electrochemistry are characterized as “Complex corrosion models based on electrochemical principles and Butler-Volmer kinetics have been developed [64], [50]. These models are not yet sufficiently developed and they are impractical for practising engineers due to the high level of details required - e.g. knowledge of where pits will localize, future variations in relative humidity in the concrete, etc. Simpler models are required” [62].

Rodriguez’s model [87] uses Faraday’s law to compute the corrosion rate of reinforcement according to the kinetics of the cathodic and anodic reactions or the oxidation-reduction:

$$\dot{x}_{corr}(t) = 0.0116 i_{corr}(t) \tag{2.30}$$

where $\dot{x}_{corr}$ is the average corrosion rate in the radial direction [μm/year], i_{corr} is the corrosion current density [μA/cm^2] and t is the calculated time after the end of the initiation period [years]. The constant 0.0116 is a convention factor from μA/cm^2 to mm/year under the assumptions that (Fe) has n equal to 2 (number of electrons freed by corrosion reaction), M equals to 55.85 g (atomic mass of Fe) and d (density of iron) equals to 7.88 g/cm^3. By the integration of Eq. 2.30, the corroded depth is obtained:

$$x_{corr}(t) = \int_{t_{ini}}^{t} 0.0116 i_{corr}(t) R_{corr} \, \mathrm{d}\tau \tag{2.31}$$

where x_{corr} is the total amount of corroded steel in the radial direction [mm] and R_{corr} is a parameter depending on the type of corrosion [-]. For uniform corrosion (such as carbonation) $R_{corr} = 1$, for pitting corrosion (such as chlorides) $R_{corr} = \langle 2, 4\rangle$ according to [37] or even $R_{corr} = \langle 4, 5.5\rangle$ according to [27].

Corrosion rate can be estimated also from exposure class of concrete before cracking time from table presented in Fig. 2.26.

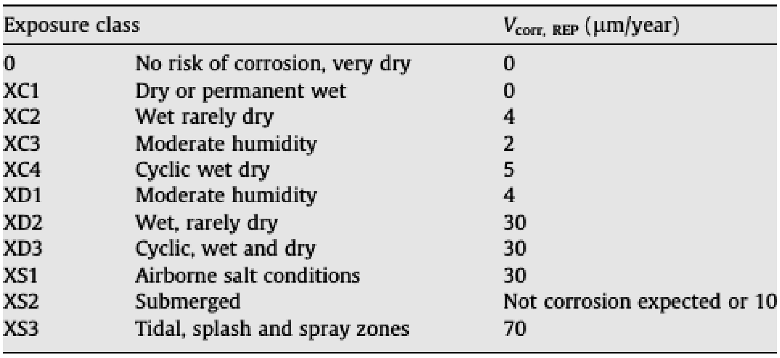

Exposure class		$V_{corr,\ REP}$ (µm/year)
0	No risk of corrosion, very dry	0
XC1	Dry or permanent wet	0
XC2	Wet rarely dry	4
XC3	Moderate humidity	2
XC4	Cyclic wet dry	5
XD1	Moderate humidity	4
XD2	Wet, rarely dry	30
XD3	Cyclic, wet and dry	30
XS1	Airborne salt conditions	30
XS2	Submerged	Not corrosion expected or 10
XS3	Tidal, splash and spray zones	70

Figure 2.26: Average corrosion rates based on exposure classes from EN206 [63]

Model related to a diffusion-limited access of oxygen is based on the following equation [48]:

$$i/nF = -D_{O2}(dC^*_{O2}/dx) \tag{2.32}$$

where i is cathodic current density [μA/cm^2], n is number of electrons transferred in the cathodic reaction (=4), F is Faraday’s constant [96487 C/mol], D_{O2} is efficient diffusion coefficient of O$_2$ in concrete [m^2/s], C^*_{O2} is concentration of O$_2$ [mol/m^3], x is distance [m]

The corrosion rate can be expressed by **empirical relations**, one of these models is presented in DuraCrete model [72]:

$$x_{corr} = \frac{m_0}{\gamma} \cdot F_{Cl} \cdot F_{Calv} \cdot F_{O_2} \cdot F_{oxide} \tag{2.33}$$

where m_0 is factor given by the corrosion rate versus electrical resistivity, γ is electrical resistivity of the concrete and parameters F are factors influencing the local corrosion rate, the chloride corrosion rate factor, the galvanic effect factor, the oxygen availability factor and the oxide (rust) factor.

After spalling of concrete cover, the direct corrosion of the reinforcement occurs. Corrosion rates i_{corr} for uncovered steel can be estimated from Fig. 2.27. They strongly depend on the aggressivity of the surrounding environment.

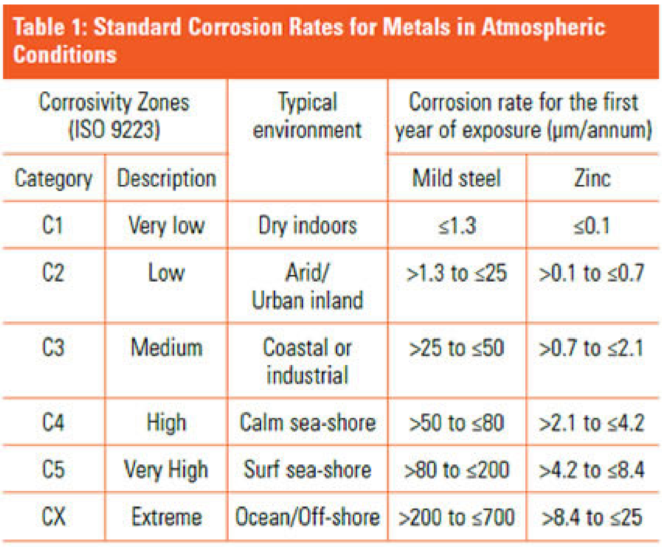

Table 1: Standard Corrosion Rates for Metals in Atmospheric Conditions

Corrosivity Zones (ISO 9223)		Typical environment	Corrosion rate for the first year of exposure (µm/annum)	
Category	Description		Mild steel	Zinc
C1	Very low	Dry indoors	≤1.3	≤0.1
C2	Low	Arid/ Urban inland	>1.3 to ≤25	>0.1 to ≤0.7
C3	Medium	Coastal or industrial	>25 to ≤50	>0.7 to ≤2.1
C4	High	Calm sea-shore	>50 to ≤80	>2.1 to ≤4.2
C5	Very High	Surf sea-shore	>80 to ≤200	>4.2 to ≤8.4
CX	Extreme	Ocean/Off-shore	>200 to ≤700	>8.4 to ≤25

Figure 2.27: Corrosion rates of steel under atmospheric exposition, reproduced from [99]

2.7.4.1 Corrosion current density models for chlorides

Vu and Stewart [113] formulated a model based on oxygen diffusivity and electrical resistivity. If the relative humidity is low, the electrical resistivity is a decisive factor, otherwise, the oxygen distribution is a controlling factor. For an assumed ambient relative humidity 75% and temperature 20°C, the corrosion current density i_{corr} [μ A/cm^2] after the end of the corrosion initiation yields:

$$i_{corr}(t_{ini}) = \frac{37.8(1-w/c)^{-1.64}}{d} \tag{2.34}$$

where t_{ini} means the start of the propagation period, w/c is the water cement ratio and d is the cover thickness [mm].

Vu and Stewart research [113] considers reduction of corrosion rate during propagation period plotted in Fig. 2.28, the i_{corr} is presented as:

$$i_{corr}(t) = i_{corr}(t_{ini}) \cdot 0.85 t^{-0.29} = \frac{32.13(1-w/c)^{-1.64}}{d} t^{-0.29} \tag{2.35}$$

Liu and Weyers's [58] model is formulated from experimental studies, statistical analysis of 44 uncracked bridge deck slabs with a concrete cover of 25, 51, 67 mm, with various w/c ratios (0.41, 0.42, 0.43 and 0.45) and cement content from 337 to 382 kg/m^3. The corrosion rates were measured by two devices (3LP and Gecor) in differentially contaminated specimens by NaCl for five years in an outdoor environment. The result is this non-linear regression model [59]:

$$\begin{aligned} i_{corr} = 0.926 \cdot \exp \Big[& 7.98 + 0.7771 \ln(1.69 C_t) - \frac{3006}{T} - \\ & 0.000116 R_c + 2.24 t^{-0.215} \Big] \end{aligned} \tag{2.36}$$

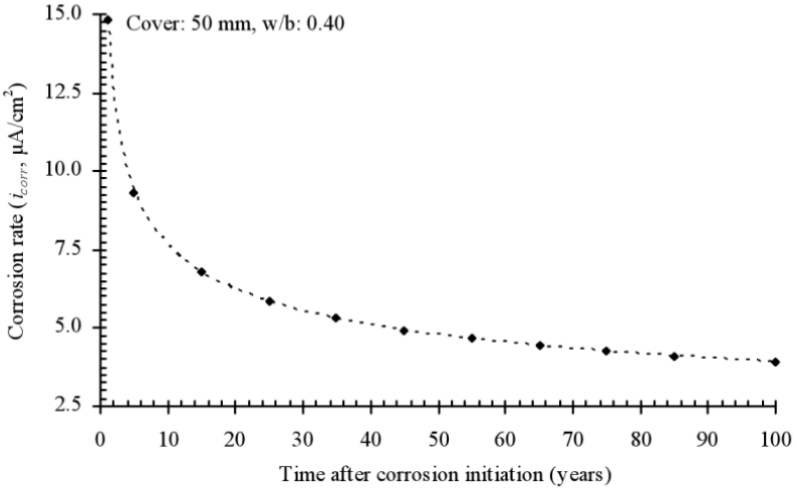

Figure 2.28: Reduction of i_{corr} with time during propagation period [113]

where i_{corr} is the corrosion current density [μA/cm^2], C_t is the total chloride content [kg/m^3 of concrete] at reinforcement determined from 1D non-stationary transport, T is the temperature at the depth of reinforcement [K] and t is the time after initiation [years]. R_c is the ohmic resistance of the cover concrete [Ω] [59]:

$$R_c = \exp\left[8.03 - 0.549\,\ln(1 + 1.69C_t)\right] \tag{2.37}$$

Other corrosion current density models exist besides those presented. For example; Alonso et al. model [4] and Yalcyn and Ergun model [122] neglects influence of concrete cover thickness.

In the case of corrosion due to carbonation, i_{corr} can be evaluated directly from Fig. 2.29. Corrosion rate is given by relative humidity [76].

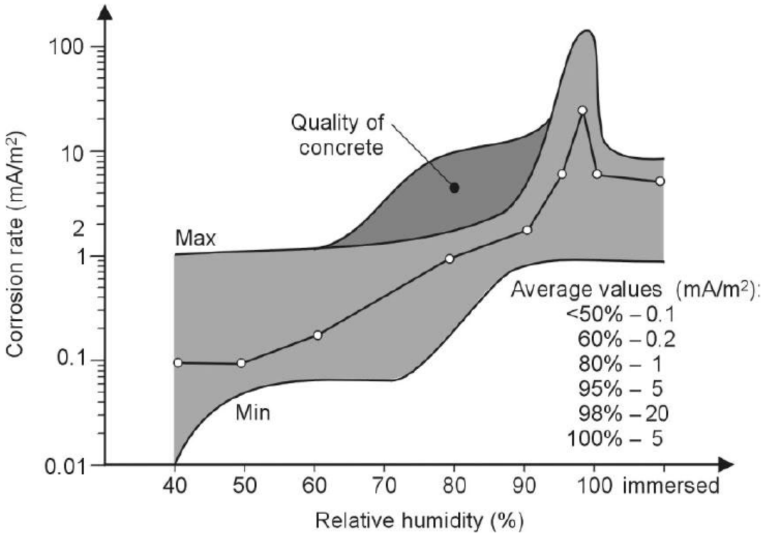

Figure 2.29: Corrosion rate in carbonated concrete and its dependence on relative humidity [76], note that 1 mA/m^2 = 0.1 μm/cm^2

2.7.5 Modelling of corrosion-induced deterioration of concrete

Corrosion of the reinforcement causes its damage. The rust is formed during this corrosion process. The volume of final products is approximately 2–10 times larger than the original reinforcement [121]. Consequently, the stresses are generated. If the tensile strength of the concrete is reached, the concrete cover layer will crack, illustrated in Fig. 2.30.

Liu and Weyer's model [58] considers three stages for reinforcement corrosion:

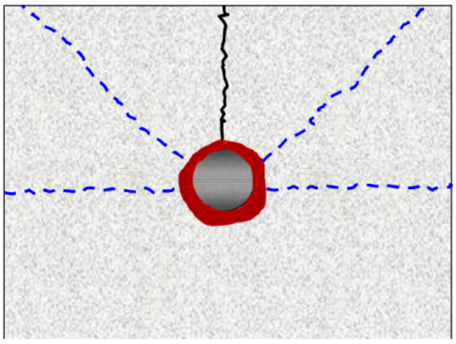

Figure 2.30: Illustration of the first corrosion induced crack [121]

1. Free expansion - amount of corrosion products is less than amount needed to filling of porous zone around reinforcement.
2. Stress initiation - amount of corrosion products filled a porous zone.
3. Concrete cracking - the critical amount of corrosion products W_{crit} is reached and cracking starts. The volume of the porous zone depends on "surface area of the reinforcement, w/c ratio, degree of hydration, and degree of consolidation." [58].

W_{crit} is determined as follows [mg/mm]:

$$W_{crit} = \rho_{rust} \left(\pi \left[\frac{C f_t'}{E_{ef}} \left(\frac{a^2 + b^2}{b^2 - a^2} + \nu_c \right) + d_0 \right] d_{ini} + \frac{W_{st}}{\rho_{st}} \right) \tag{2.38}$$

where ρ_{rust} is a density of the corrosion products [mg/mm^3], C is the concrete cover [mm], f_t' is the tensile strength of the concrete [MPa], E_{ef} is the effective elastic modulus of the concrete, $E_{ef} = E_c/(1 + \varphi_{creep})$, ν_c is Poisson's ratio of the concrete, d_0 is the thickness of the pore band around the steel/concrete interface [mm], d_{ini} is the diameter of the reinforcement [mm], W_{st} is the amount of steel loss, ρ_{st} is the density of steel [mg/mm^3], $a = (d_{ini}+2d_0)/2$, $b = C+(d_{ini}+2d_0)/2$.

Model have been developed to predict the time of corrosion-induced cracking of the concrete cover $t_{p,cr}$ (depicted in Fig. 3.2):

$$t_{p,cr} = \frac{W_{crit}^2}{2k_p} \tag{2.39}$$

where k_p is the rate of rust production:

$$k_p = 0.098\,(1/\alpha)\,\pi d_{ini} i_{corr} \tag{2.40}$$

where i_{corr} is an annual mean corrosion rate [μA/cm^2] and α = 0.523-0.622.

Other models deal with the cracking due to critical amount of corrosion products; Bažant [8], Alonso et al. [5] and Broomfield [15] models.

The cracking of concrete cover given from the DuraCrete model [72] is based on the critical penetration depth of corroded steel $x_{corr,cr}$ formulated as:

$$x_{corr,cr} = a_1 + a_2 \frac{C}{d_{ini}} + a_3 f_{t,ch} \tag{2.41}$$

where a_1, a_2, a_3 are the universal regression parameters, a_1 equals to $7.44 \cdot 10^{-5}$ m, the parameter a_2 equals to $7.3 \cdot 10^{-6}$ m and a_3 is $-1.74 \cdot 10^{-5}$ m/MPa. C is the cover thickness of concrete [m], d_{ini} is the initial bar diameter [m], $f_{t,ch}$ is the characteristic splitting tensile strength of concrete [MPa].

The critical penetration depth of corroded steel at spalling $x_{corr,sp}$ is calculated from [72] as:

$$x_{corr,sp} = \frac{w_d - w_0}{b} + x_{corr,cr} \tag{2.42}$$

where the parameter b depends on the position of the bar (for top reinforcement equals to 8.6 and for bottom equals to 10.4), w_d is the critical crack width for spalling (characteristic value 1 mm), w_0 is the width of the initial crack and $x_{corr,cr}$ is the depth of corroded steel at the time of cracking [m].

2.8 Alkali-silica reaction

In the majority of concretes, aggregates are more or less chemically inert. However, some aggregates react with the alkalies in concrete, causing expansion and cracking over a period of many years. This alkali-aggregate reaction has two forms: alkali-silica reaction (ASR) and alkali-carbonate reaction (ACR). Alkali–silica reaction (ASR), one of those common deleterious mechanisms, consists in a chemical reaction between "unstable" silica mineral forms within the aggregate materials (opal, tridymit, crystobalite, chert, volcanic glass) and the alkalies (Na) dissolved in the concrete pore solution. It generates a secondary alkali–silica gel that induces expansive pressures within the reacting aggregate material(s) and the adjacent cement paste upon moisture uptake from its surrounding environment, thus causing micro cracking, loss of material's integrity (mechanical/-durability) and, in some cases, functionality in the affected structure. A schematic illustration of the ASR expansion and corresponding cracking is shown in Fig. 2.31.

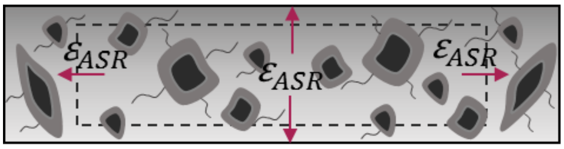

Figure 2.31: Expansion of material due to ASR

Several aggregate types in common use, particularly those with a siliceous composition, may be attacked by the alkaline in concrete. This attack, essentially a dissolution reaction, requires a certain level of moisture and alkalis (leading to high pH) within the concrete to take place. During the reaction, a hygroscopic gel forms. When imbibing water, the gel will swell and thus cause expansion, cracking, and in worst case disruption of the concrete [57]. The Fig. 2.32 show examples of real cracked concrete structures due to ASR expansion.

Figure 2.32: Expansion of material due to ASR reaction [120] [32]

There are several test methods for measuring of ASR expansion, fox example ASTM C 1293 (The Standard Test Method for Concrete Aggregates by Determination of Length Change of Concrete Due to ASR). This method operates with concrete prisms with dimensions of 75 × 75 × 285 mm and w/c ratio from 0.42 to 0.45. Maximal expansion is measured at relative humidity 100% and temperature 38°C. Test ASTM C 1567 (Accelerated Mortar-Bar Method) is the same as the previous one ASTM C 1293 but suited for mortar prisms. The optical microscopy can also help in observing and studying of expansion, outputs presented in Fig. 2.33.

Thus, the degree of reaction of an aggregate is a function of the alkalinity of the pore solution. For a given aggregate, a critical lower pH-value exists below which the aggregate will not react. Consequently, ASR will be prevented by lowering pH of the pore solution beneath this critical level where the dissolution of alkali-reactive constituents (silica) in the aggregates will be strongly reduced or even prevented, as discussed in [87]. No "absolute" limit is defined, because the critical alkali content largely depends on the aggregate reactivity [37], but from many experimental test we can estimate threshold value [57], [83].

Many studies carried out over the past few decades have shown that ASR can affect the mechanical properties of concrete. Usually, ASR generates a significant reduction in tensile strength

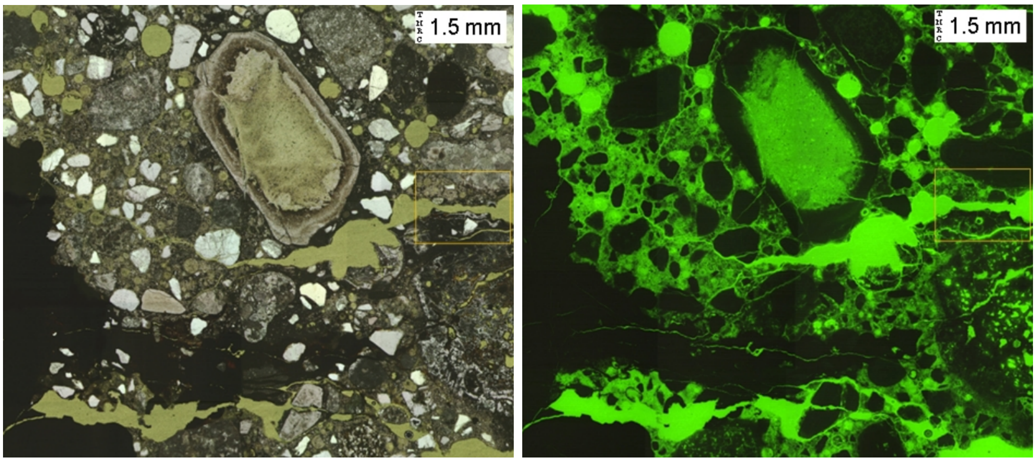

a) b)

Figure 2.33: The upper-middle sand chert particle has undergone ASR. Voids and cracks near the chert aggregate are lined with alkali-silica gel [93] a), the fluorescent dye together with blue and yellow filters allow for easier observation of cracks, voids, and porosity. The alkali-silica reactive chert aggregate is more porous in the interior, and more dense where in contact with the cement paste [93] b)

Figure 2.34: Alto Ceira dam demolished in 2012 due to excessive ASR

and modulus of elasticity of concrete. These two properties are much more affected than compressive strength, which begins to decrease significantly only at high levels of expansion. For example, in Portugal, more than 30% of concrete dams are affected by ASR. One of them is Alto Ceira dam, which was due to ASR damage demolished and replaced by a new dam, see Fig. 2.34

2.8.1 Modelling of alkali-silica reaction

Several ASR models were developed over the years to predict expansion and damage on both ASR affected materials (microscopic models) [70], [10], [24] and ASR affected structures/structural elements (macroscopic models) [110], [90], [25]. The first group has a goal of modelling both the chemical reactions and the mechanical distresses caused by ASR or even the coupling of the two phenomena. The second group aims at understanding the overall distress of structures/structural concrete elements in a real context, simulating their likely in situ behaviour [31] to bridge the scientific approaches with practical applicability to real structures.

In terms of mechanical effects, it is known that ASR expansions occur over long time periods.

During this process, ASR affected concretes are subjected to a progressive stress built up that is very likely to cause creep on the distressed materials.

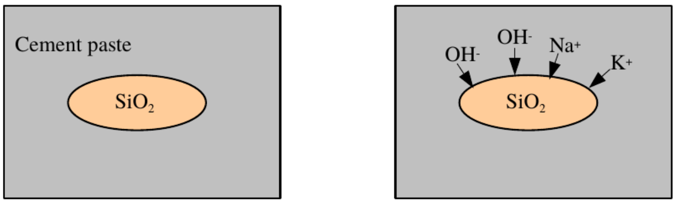

Reactive SiO_2 is attacked by OH^- and then by Na^+, K^+.

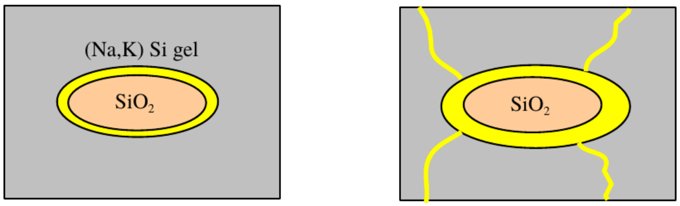

Alkali-silca gel is formed.

Alkali-silca gel absorbs water and expands

Figure 2.35: Mechanism of ASR expansion [93]

ASR depends on the availability of three factors: alkalies liberated from cement, siliceous minerals present in certain kinds of aggregates and water. Several microscopic and random factors are involved in ASR expansion, such as concrete porosity, amount and location of reactive regions in the material and permeability [31]. These parameters, added to concrete's intrinsic heterogeneity, turn simulating ASR expansion into a rather complex task. Even though ASR process has not been well explained so far, the commonly accepted theory for describing it is two distinct phases need to be considered: gel formation and water absorption by the gel, causing the expansion. Fig. 2.35 shows schematic illustration of ASR. According to this mechanism, reaction does not always lead to expansion. As long as there is enough void space to be filled by the gel, i.e. pores and cracks, concrete volume remains unchanged.

2.9 Mechanical material models

Modelling of crack propagation during ASR relies on underlying mechanical models. Concrete is treated as a homogeneous continuum and the onset of damage with cracking is based on stress criteria [45]. A brief summary recalls basic formulation of used models.

The linear elastic model describes the simplest relationship between strain and stress, based on the Hooke's law:

$$\sigma = E\varepsilon^e \tag{2.43}$$

where ε^e is the elastic strain and E is Young's modulus.

In the real material, sooner or later there will be deviations from linearity and different behaviour in loading and unloading depending on the specific type of material. Therefore, the elastic material is extended for inelastic effects, such as the permanent strains due to plastic deformation processes or the reduction of stiffness coefficients due to the cracks and voids formation and development [45].

The elastic-plastic model shown in the Fig. 2.36a) focuses on the description of the permanent (plastic) strain. During unloading, the material behaves as linear elastic with the same initial

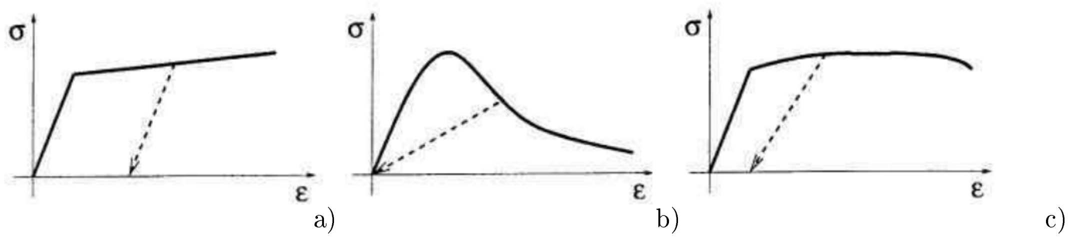

Figure 2.36: Stress-strain diagrams. Elastic-plastic material a), fracture-elastic material b), fracture-plastic material c) [45]

stiffness. The elastic-plastic behaviour expressed by equations:

$$\sigma = E(\varepsilon - \varepsilon^p) \tag{2.44}$$

where ε is the total strain $\varepsilon = \varepsilon^e + \varepsilon^p$ and ε^p is the plastic strain.

In contrast, isotropic damage models are based on the idea of the cracks and voids formation and development with corresponding reduction in material stiffness:

$$\sigma = (1 - \omega)E\varepsilon \tag{2.45}$$

where ω is the damage variable, which ranges from 0 (virgin material) to 1 (fully damaged material). If the material remains elastic between the cracks (no permanent strain occur), the strain-stress diagram returns to zero after unloading, as shown in the Fig. 2.36b).

The combination of previous two models gives a fracture-plastic model, which describes the real behaviour of materials, such as concrete. There is a reduction in stiffness and permanent strains, which is depicted by the stress-strain diagram in the Fig. 2.36c). The fracture-plastic model is used in static analyses presented in this work and described in more detail below.

2.9.1 Fracture-plastic model

The modelling of crack effect on acceleration of chloride ingress and carbonation together with concrete degradation due to ASR expansion is the main benefit of this work. The nonlinear finite element analyses presented further are performed with the ATENA software [22] using the combined fracture-plastic model for concrete by Červenka & Papanikolaou [19].

The constitutive model formulation assumes small strains and the strain decomposition into elastic ε^e, plastic ε^p and fracture ε^f components. The stress development is described by the rate equations reflecting progressive damage (concrete cracking) and plastic yielding (concrete crushing):

$$\dot{\sigma} = D \cdot (\dot{\varepsilon} - \dot{\varepsilon}^p - \dot{\varepsilon}^f) \tag{2.46}$$

Flow rules govern the evolution of plastic and fracturing strains:

$$\text{Plastic model: } \varepsilon^p = \dot{\lambda}^p \cdot m^p, \quad m^p = \frac{\partial g^p}{\partial \sigma} \tag{2.47}$$

$$\text{Fracture model: } \varepsilon^f = \dot{\lambda}^f \cdot m^f, \quad m^f = \frac{\partial g^f}{\partial \sigma} \tag{2.48}$$

where $\dot{\lambda}^p$ is the plastic multiplier rate and g^p is the plastic potential function, $\dot{\lambda}^f$ is the inelastic fracturing multiplier and g^f is the potential defining the direction of inelastic fracturing strains. The multipliers are evaluated from the consistency conditions.

The Menetrey-Willam model [66] is used for the plasticity of concrete in multiaxial stress state in compression, see Fig. 2.37, with nonlinear hardening in Fig. 2.38, and linear softening in Fig. 2.39.

In tension, the Rankine criterion for tensile fracture with exponential softening by Hordijk [40] is used, where w_t stands for the crack width, see Fig. 2.40.

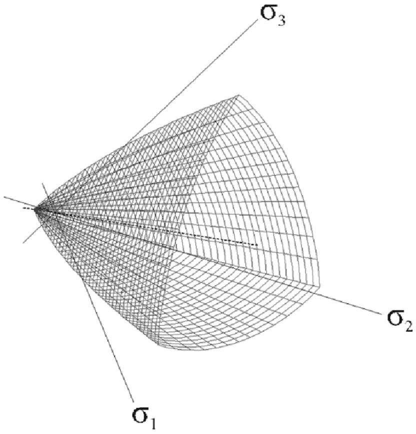

Figure 2.37: Visualization of the three-parameter concrete failure criterion; Menetrey & Willam [66]

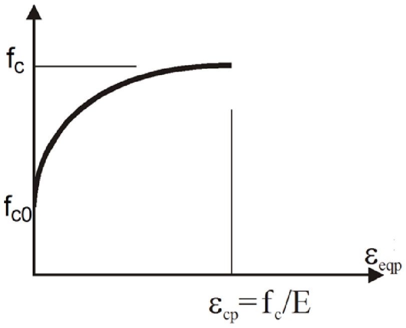

Figure 2.38: Hardening law for the concrete plasticity model in compression

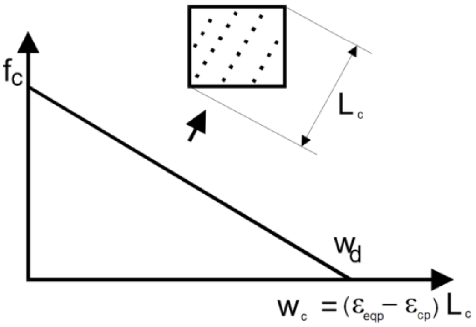

Figure 2.39: Softening law for the concrete plasticity model in compression

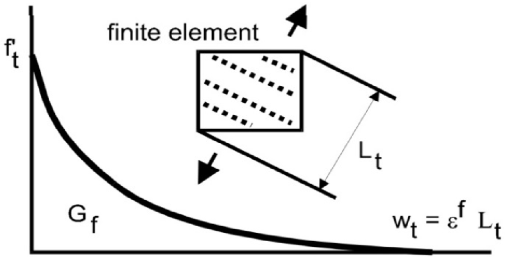

Figure 2.40: Crack opening law according to Hordijk [40]

The stress softening in tension is determined using the crack band approach of Bažant & Oh [9] and, analogically, in compression of Červenka et al. [20]. The crack band as well as the crush band size are adjusted with regard to the crack orientation approach proposed by Červenka &

Margoldová [21]. This method is illustrated in Fig. 2.41 and described by Eq. 2.49:

$$\begin{aligned} L_t^{'} &= \alpha\gamma L_t \quad \text{and} \quad L_c^{'} = \gamma L_c & (2.49) \\ \gamma &= 1 + (\gamma_{max} - 1)\frac{\theta}{45}, \quad \theta \in \langle 0; 45 \rangle, \quad \gamma_{max} = 1.5 & (2.50) \end{aligned}$$

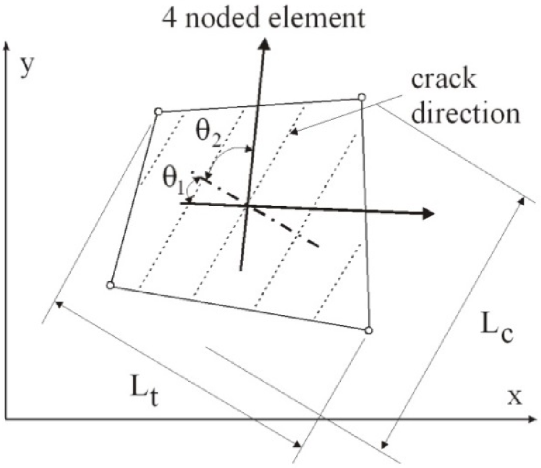

Figure 2.41: Crack band formulation

The crack angle θ is taken as the average angle between the crack direction and element sides.

The above formulation controls the strain localization accounting for the mesh size and the crack orientation. The parameter α is introduced to cover the localization effect due to the element type as reported recently in the work of Slobbe et al. [92]. In this study, $\alpha = 1$ is used for low order elements with a 2×2 integration scheme and $\alpha = 0.6$ for quadratic elements with a 3×3 integration scheme.

Some additional features of cracked concrete are included in the model, namely the reduction of compressive strength and shear stiffness degradation, often referred as a shear retention effect, should be mentioned due to their importance in problems dominated by shear failure.

The damage of concrete by cracks is reflected according to Bentz et al. [11] in the reduction factor r_c of the compressive strength f_c as follows:

$$\sigma_c = r_c f_c, \quad r_c = \frac{1}{0.8 + 170\varepsilon_1}, \quad r_c^{lim} \leq r_c \leq 1.0 \tag{2.51}$$

where ε_1 is the tensile strain perpendicular to the crack. The largest maximal fracturing strain is used for ε_1 and the compressive strength reduction is limited by r_c^{lim}. In this work, $r_c^{lim} = 0.8$ is considered. The shear strength of the cracked surface is also considered according to the modified compression field theory (MCFT) by Bentz et al. [11]:

$$\sigma \leq \frac{0.18\sqrt{f_c^{'}}}{0.31 + \frac{24w}{a_g + 16}} \tag{2.52}$$

taking into account the crack width w and the aggregate size a_g. Since MCFT does not offer shear stiffness, the authors proposed to relate the shear stiffness K_t^{cr}, oriented tangentially to the crack face, to the normal stiffness K_n^{cr} already defined by the crack opening law:

$$K_t^{cr} = s_F K_n^{cr} \tag{2.53}$$

The normal stiffness comes directly from the tensile softening law in Fig. 2.40 as:

$$K_n^{cr} = f_t(w_t)/w_t \tag{2.54}$$

This makes the shear stiffness dependent on the crack opening displacement and independent of the mesh size. The scaling factor $s_F = 50$ was used in the presented analyses.

Chapter 3

Performance of selected models for concrete

Reinforcement corrosion due to chloride ingress and carbonation are considered to be the most damaging mechanism for reinforced concrete (RC) structures in the world [106]. The previous chapter describes in detail the relevant corrosion processes for steel and later for ASR.

The resistance of the structure to ASR is given by the use of aggregates containing reactive silica minerals, alkalis contained in cement and relative humidity. ASR expansion can leads to damage of the concrete. The presented approach considers the direct degradation of material parameters according to the degree of reaction and the reaching of the expansion pressure of the tensile strength of concrete.

In case of reinforcement corrosion, the aggressive agents have to penetrate through the concrete cover layer at first, therefore, the durability of the structure is given by the quality of this layer, see Fig. 3.1. Reinforcement and concrete corrosion generally leads to decreased serviceability and durability, which has a further impact on the life cycle costs and the environment. Chloride ingress is mostly caused by de-icing salts, sea water and salts in coastal areas. The quality of the concrete cover, without cracks, with low porosity and permeability, with high ability to resist to chlorides and carbon dioxide is controlled by several factors such as concrete cover thickness, cement type and content, w/b ratio and environmental boundary conditions [51], [58].

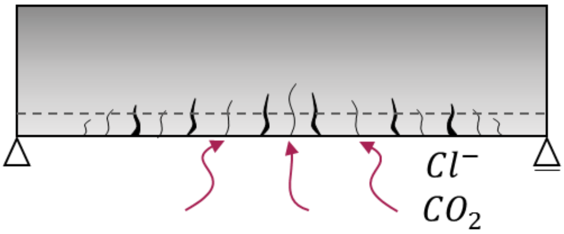

Figure 3.1: Corrosion mechanism due to chloride ingress and carbonation

The classical approach assumes the onset of reinforcement corrosion when the chloride concentration exceeds a critical threshold in the place of reinforcement for the chloride ingress. In the second case of corrosion due to carbonation, this moment gives the lowering of pH under the value of 9 [72, Tab 8.7]. The critical chloride content approaches 0.6% by weight of the binder [116, p. 72]. Other sources give a consistent range of 0.5-0.9% for a tidal and splash zone and 1.6%-2.3% for submerged concrete [72, Tab 8.7].

The initiation period t_i corresponds to no steel corrosion, see Fig. 3.2. After the initiation period, the propagation period t_p takes place, when the steel reinforcement corrodes and expanding corrosion products are formed. Chlorides often exhibit a pitting corrosion [28], for carbonation uniform corrosion is typical. The times $t_{p,cr}$ and $t_{p,sp}$ in Fig. 3.2 correspond to the cracking and spalling time of the concrete cover. They are related to corrosion depths $x_{corr,cr}$ and $x_{corr,sp}$ [72].

The Chapter 2.7 presents several models dealing with prediction of chloride concentration, carbonation depth and steel corrosion rate, which serve to determine the reduction of reinforcement over time.

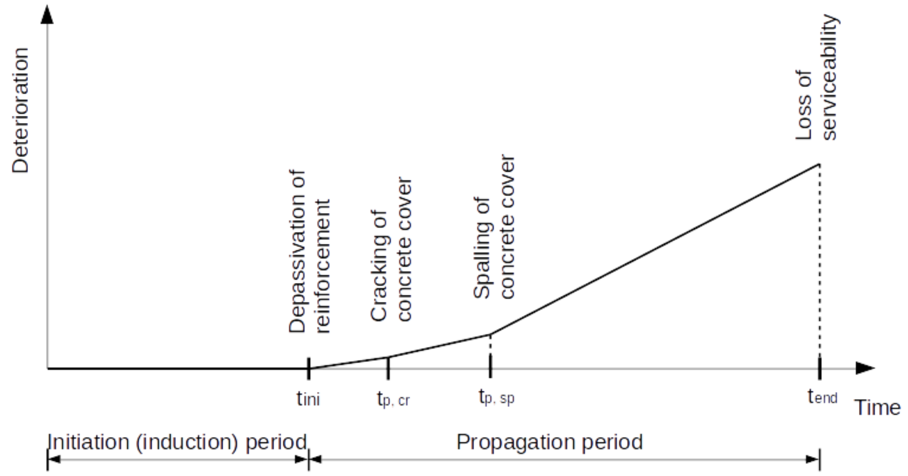

Figure 3.2: Initiation and propagation period

3.1 Carbonation material model

3.1.1 Carbonation model by Papadakis

Carbonation depth of a sound (macroscopically uncracked) concrete has the form [79]:

$$x_c = \sqrt{\frac{2D_{e,CO_2}CO_2}{0.218(C+kP)}}\sqrt{t} = A_1\sqrt{t} \tag{3.1}$$

where x_c is the carbonation depth, D_{e,CO_2} is the effective diffusivity for CO_2, C is the Portland cement content in kgm^{-3}, $k \in \langle 0.3, 1.0\rangle$ is the efficiency factor of supplementary cementitious material (SCM) such as slag, silica fume, or fly ash, P is the amount of SCM in kgm^{-3}, CO_2 is the volume fraction of CO_2 in the atmosphere taken as 3.6e-4 and t is the time of exposure.

The effective diffusivity in m^{2}s^{-1} is given by empirical equation [79]:

$$D_{e,CO_2} = 6.1\cdot 10^{-6}\left(\frac{[W-0.267(C+kP)]/1000}{\frac{C+kP}{\rho_c}+\frac{W}{\rho_W}}\right)^3\cdot(1-RH)^{2.2} \tag{3.2}$$

where W is the water content in fresh concrete in kgm^{-3}, C is the cement density in kgm^{-3} assumed as 3150 kgm^{-3} and RH is the relative humidity of ambient air. Eq. 3.1,3.2 allow predicting either carbonation depth, x_c, or induction time, t, of uncracked concrete.

Cracked concrete leads to faster carbonation. This acceleration was quantified [52], which modifies Eq. 3.1 to the form:

$$x_c(t) = (2.816\sqrt{w}+1)A_1\sqrt{t} \tag{3.3}$$

where w is the crack width in mm and A_1 is the carbonation progress according to Eq. 3.1. Eq. 3.3 allows computing carbonation depth and induction time as well. Note that crack width of 0.3 mm increases the carbonation depth by a factor of 2.54. This also means that induction time is 6.46 times shorter in such a case when compared to uncracked concrete.

In reality, crack may grow gradually over service time. Thus Eq. 3.3 needs to be recast into an incremental form. An increment of carbonation depth in a given time step Δt is evaluated from the total derivative of Eq. 3.3:

$$\Delta x_c(t) = \frac{(2.816\sqrt{w_{i+1}}+1)A_1}{2\sqrt{t_{i+0.5}}}\Delta t + \frac{2.816A_1\sqrt{t_{i+0.5}}}{2\sqrt{w_{i+0.5}}}\Delta w \tag{3.4}$$

where w_{i+1} is the crack width at the end of a time step, $t_{i+0.5}$ is the mid-time during time integration. It is assumed that a nonzero crack increment Δw at integration time $t_{i+0.5}$ has no effect on carbonation depth, thus the term Δw can be left out. Eq. 3.4 allows predicting either carbonation depth or induction time of gradually cracking concrete [94].

Eqs. 3.1, 3.2, 3.3 have been implemented in software CarboChlorCon, see Fig. 3.3. It is available at `http://mech.fsv.cvut.cz/~smilauer/index.php?id=software`

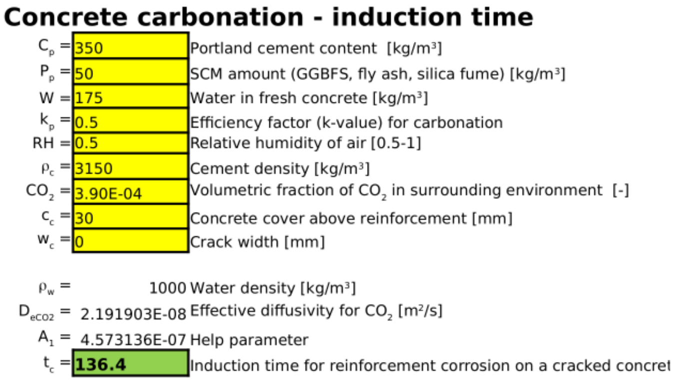

Concrete carbonation - induction time

C_p = 350 Portland cement content [kg/m³]
P_p = 50 SCM amount (GGBFS, fly ash, silica fume) [kg/m³]
W = 175 Water in fresh concrete [kg/m³]
k_p = 0.5 Efficiency factor (k-value) for carbonation
RH = 0.5 Relative humidity of air [0.5-1]
ρ_c = 3150 Cement density [kg/m³]
CO_2 = 3.90E-04 Volumetric fraction of CO_2 in surrounding environment [-]
c_c = 30 Concrete cover above reinforcement [mm]
w_c = 0 Crack width [mm]

ρ_w = 1000 Water density [kg/m³]
D_{eCO2} = 2.191903E-08 Effective diffusivity for CO_2 [m²/s]
A_1 = 4.573136E-07 Help parameter
t_c = **136.4** Induction time for reinforcement corrosion on a cracked concret

Figure 3.3: Software CarboChlorCon for carbonation with implemented Papadakis model

3.1.2 Effect of parameters P, C, W on the length of initiation period

As presented in the previous Section 3.1.1, the initiation time is influenced by a crack width and concrete composition, especially by the amount of SCM (P), by the Portland cement content (C) and by the water content (W). Influence of these three parameters on the length of the initiation period for concrete cover 30 mm is showed in Fig. 3.4. Fig. 3.4 considers concrete without cracks, crack widths of 0.1 mm, 0.2 mm and 0.3 mm. Only one parameter changes in each graph and the

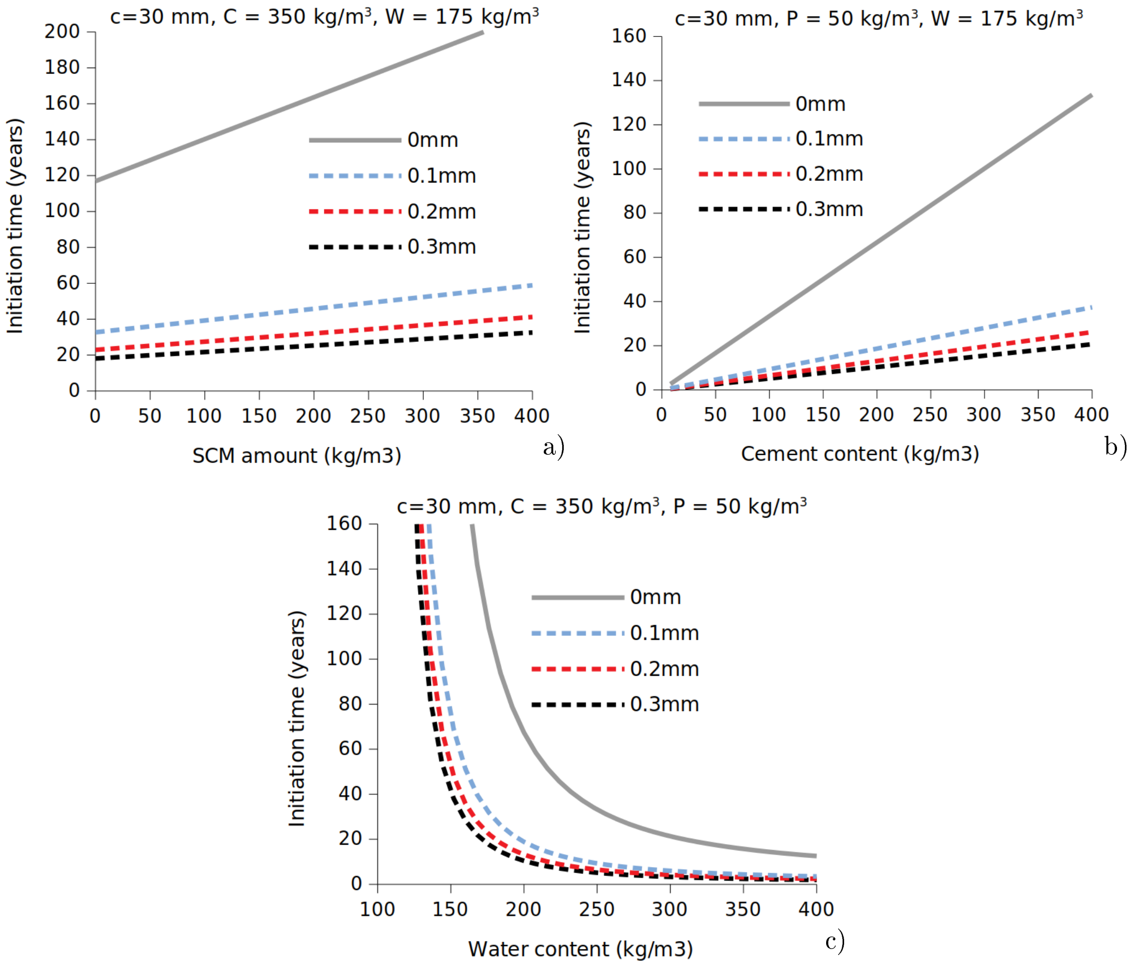

Figure 3.4: Effect of amount of SCM a), influence of Portland cement content C b), influence of water content W c)

others ones remain constant.

In the first case a) the SCM content changes. The initiation time ranges from 117 to 210 years for the sound concrete. In the case of a crack width of 0.3 mm, the initiation time ranges from 18 to 33 years. This means that a crack of 0.3 mm decreases the initiation time by approximately 6.5 times compared to sound concrete for SCM content 400 kg/m^3. The minimum amount of SCM to ensure an initiation time longer than 25 years is 190 kg/m^3 for all four crack scenarios. The initiation time increases with higher SCM content. Therefore, it has a positive effect on the extension of the reinforcement state without corrosion.

The situation is similar in the second case, where the content of Portland cement C varies b). Higher amounts of the cement content have a positive effect on the length of the induction time. The initiation time ranges from 0 to 133 years for the sound concrete. In the case of a crack width of 0.3 mm, the initiation time ranges from 0 to 20 years. The minimum cement content to ensure an initiation time longer than 20 years is 392 kg/m^3 (w/c=0.45) for all four crack scenarios.

In the last case, the initiation time decreases with higher water content W. The maximum amount of water to ensure an initiation period of 25 years is 272 kg/m^3 (w/c=0.78) for sound concrete and 160 kg/m^3 (w/c=0.46) for cracked concrete.

3.2 Chloride ingress material models

Models predicting the initiation period assume that steel corrodes as soon as the chloride concentration exceeds a critical threshold [72, Tab 8.7]. For this reason, determination of chloride profile due to chloride ingress is essential.

In the previous Chapter 2, several models of chloride ingress were presented. This part describes three selected models in more detail, their use and comparison in validation. The first model is the Collepardi-Marcialis-Turriziani model [23], the second one is ClinConc model proposed by Tang [103] which considers chloride binding. The last one is the DuraCrete model [72].

3.2.1 Collepardi-Marcialis-Turriziani (CMT) model for initiation period

This simple model was developed in 1970s to solve chloride ingress into concrete. The model uses an erf function as a solution to Fick's second law of diffusion under the semi-infinite boundary condition [23]:

$$C(x,t) = C_i + (C_s - C_i) erf\left(\frac{x}{2\sqrt{D_a t}}\right) \tag{3.5}$$

where C_s is the chloride content at surface [kg/m^3 or kg/kg of the binder], C_i is the initial chloride content in the concrete (can be negligible), x is the distance from the surface in [m], D_a is apparent diffusion coefficient [m^2/s] and t is the exposure time.

In this case, the key is to determine the parameters D_a and C_s, which are constant during the whole calculation. This model is suitable for determining the short-term profile of the chloride concentration. Parameters D_a and C_s are obtained by curve-fitting of the chloride ingress profiles from laboratory tests.

3.2.2 ClinConc model for initiation period

This model combines free chloride ingress with non-linear chloride binding [104]. The simulation of free chloride ingress uses the principle of Fick's law with the free chlorides concentration as the driving potential. The distribution of the total chloride content in concrete uses the mass balance equation combined with non-linear chloride binding. In the first step, it is needed to determine the free chloride content in the concrete at depth x from the following equation [103]:

$$\frac{c - c_i}{c_s - c_i} = 1 - erf\left(\frac{x}{2\sqrt{\frac{\xi_D D_{6m}}{1-n}} \left(\frac{t'_{6m}}{t}\right)^n \left[\left(1 + \frac{t'_{ex}}{t}\right)^{1-n} - \left(\frac{t'_{ex}}{t}\right)^{1-n}\right] t}\right) \tag{3.6}$$

where c, c_s and c_i are the concentration of free chlorides in the pore solution at depth x, at the surface of the concrete and initially in concrete, D_{6m} is the diffusion coefficient at the age of six months (t'_{6m}), ξ_D is the factor bridging the D_{6m} to the initial apparent diffusion coefficient for the decrease of diffusivity with age, t'_{ex} is the age of concrete at the start of exposure and t is the duration of exposure.

The factor ξ_D is determined from following expression [103]:

$$\xi_D = \frac{\left(0.8a_t^2 - 2a_t + 0.5\right)\left(1 + 0.59K_{b6m}\right) e^{\frac{E_D}{R}\left(\frac{1}{293}-\frac{1}{T}\right)}}{1 + k_{OH6m}K_{b6m}f_b\beta_b\left(\frac{c_s}{35.45}\right)^{\beta_b-1} e^{\frac{E_b}{R}\left(\frac{1}{T}-\frac{1}{293}\right)}} k_D \tag{3.7}$$

where a_t is a factor which describes how the chloride binding changes over time, f_b and β_b are chloride binding constants, E_D and E_b are activation energy chloride diffusion and binding, k_D is the expansion factor depending on the type of binder and water-binder ratio, k_{OH6m} and K_{b6m} are factors accounting the effects of hydroxide concentration in the pore solution, cement gel content and water accessible porosity at the age t'_{6m}, expressed as follows:

$$k_{OH6m} = e^{0.59}\left(1 - \frac{0.043}{[OH]_{6m}}\right) \tag{3.8}$$

$$k_{b6m} = \frac{W_{gel6m}}{1000\varepsilon_{6m}} \tag{3.9}$$

where $[OH]_{6m}$, W_{gel6m} and ε_{6m} are the hydroxide concentration in mol/m^3 of pore solution, cement gel content in kg/m^3 of concrete and water accessible porosity at the age t'_{6m} [103].

According to the experience obtained from 10 years exposure in the seawater at Swedish west coast realized by L. Tang [102], the expansion factor, k_D, can be estimated by:

$$k_D = \begin{cases} 1 + 8(0.4 - w/b) + 7SF + 3800(SF \cdot FA)(SF + FA) & 0.25 \le w/b \le 0.4 \\ 1 & w/b > 0.4 \end{cases} \tag{3.10}$$

where w/b is the water/binder ratio, SF and FA is the mass fraction of silica fume and fly ash to the total binder. The binding factor a_t is described as following [103]:

$$a_t = \begin{cases} 0.36 + 1.4(0.4 - w/b) + 0.4SF + 38(SF \cdot FA)(SF + FA) & 0.25 \le w/b \le 0.4 \\ 0.36 + 1.4(0.4 - w/b) & 0.4 < w/b \le 0.6 \end{cases} \tag{3.11}$$

For concrete with Portland cement or silica fume, the values f_b equals to 3.6 and β_b equals to 0.38. For the binders with fly ash (FA) and slag (BFS is the mass fraction of slag to the total binder), the constants are estimated from follows equations [103]:

$$\text{Fly ash: } f_b = 3.6 + 7FA \quad \beta_b = 0.38 - 0.3FA \tag{3.12}$$

$$\text{Slag: } f_b = 3.6 + 3.5BFS \quad \beta_b = 0.38 - 0.14BFS \tag{3.13}$$

The age factor n can be derived by parameter a_t, expressed by following equation:

$$n = (-0.45a_t^2 + 0.66a_t + 0.02) + n_{dry} \tag{3.14}$$

for cases where chloride concentration is in constantly in contact with concrete surface (submerged) is n_{dry} equal to zero.

3.2.2.1 Calculation of total chloride content

The total chloride content C to differentiate from the free chloride concentration c, is basically the sum of the bound chloride c_b and free chloride c. In this approach, the relationship between the free and total chloride chloride content is required. When chloride binding isotherm is known, the following expression can be used to derive total chloride concentration (mass % of binder) [103]:

$$C = \frac{\varepsilon(c_b + c)}{B_c} \cdot 100 \tag{3.15}$$

where ε is the water accessible porosity at the age after exposure, B_c is the cementitious binder content in kg/m^3 of concrete and

$$c_b = f_t \cdot k_{OH6m} \cdot K_{b6m} \cdot f_b \cdot c^{\beta_b} \cdot e^{\frac{E_b}{R}\left(\frac{1}{T}-\frac{1}{293}\right)} \qquad [\text{g/l}] \tag{3.16}$$

where f_t is a factor accounting for the time dependency of chloride binding and can be calculated by the following equation:

$$f_t = a_t \ln\left(\frac{c-c_i}{c_s-c_i}t+0.5\right)+1 \tag{3.17}$$

3.2.3 DuraCrete model for initiation period

There is an analytical solution for 1D transient ingress with an initially zero chloride content [72]:

$$C(x,t) = C_s\left[1-erf\left(\frac{x}{2\sqrt{D_m(t)f(w)t}}\right)\right], \quad f(w) = 31.61w^2+4.73w+1 \tag{3.18}$$

where C_s is the chloride content at surface [kg/m^3 or kg/kg of the binder], $D_m(t)$ is the mean (averaged) diffusion coefficient at the time t [m^2/s] [51], x is the distance from the surface in [m] and $f(w)$ includes acceleration by the crack width w [mm]; e.g. a crack width of 0.3 mm increases the mean diffusion coefficient by a factor of 5.26. C_s and $C(x,t)$ can be expressed relative to the concrete volume or to the binder mass. The solution of Eq. 3.18 is illustrated in Fig. 3.5; a chloride profile with and without cracks from the example presented in section 3.2.3.2.

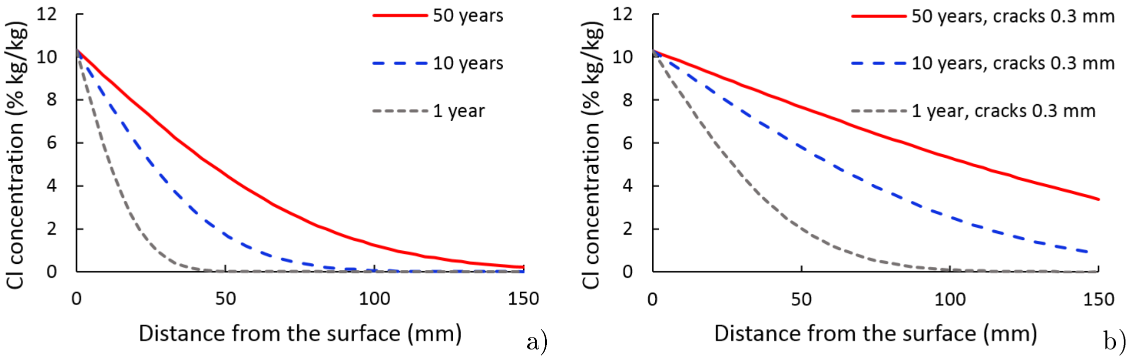

Figure 3.5: Chloride ingress model including cracks. Chloride profile without cracks a), with cracks 0.3 mm b)

The instantaneous diffusion coefficient $D(t)$ for chloride ingress is assumed to decrease over the time t according to the power law:

$$D(t) = D_{ref}\left(\frac{t_{ref}}{t}\right)^m \tag{3.19}$$

where m is the decay rate (also called the age factor). The same exponential form was employed in Model Code 2010 [116]. If $m = 0$, a constant value of $D(t) = D_{ref}$ is recovered; such a model was proposed by Collepardi et al. [23]. Nowadays, it has become clear that this assumption is too conservative and is not generally recommended.

The mean diffusion coefficient $D_m(t)$ is obtained by averaging $D(t)$ over the exposure time:

$$D_m(t) = \frac{D_{ref}}{1-m}\left(\frac{t_{ref}}{t}\right)^m, \quad t < t_R, \tag{3.20}$$

$$D_m(t) = D_{ref}\left[1+\frac{t_R}{t}\left(\frac{m}{1-m}\right)\right]\left(\frac{t_{ref}}{t_R}\right)^m, \quad t \geq t_R \tag{3.21}$$

where t_R is the time,after which the diffusion coefficient remains constant and, which is generally taken as 30 years [107]. t_{ref} corresponds to the time, when the diffusion coefficient was measured. Fig. 3.6 shows a characteristic evolution of the diffusion coefficient $D(t)$ and $D_m(t)$ through 100 years.

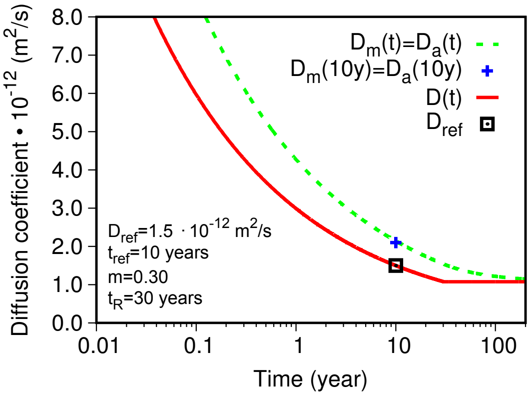

Figure 3.6: Evolution of apparent and mean diffusion coefficients

Once crack width changes over time, integration of derived Eq. (3.18) provides the mean diffusion coefficient $D_m(t)$ as:

$$D_{m,w}(t, w) = D_m(t) \int_0^{\overline{w}} 63.22w + 4.73dw \tag{3.22}$$

Software CarboChlorCon provides an implementation of the DuraCrete model with Kwon's crack acceleration [51]. It is available at `http://mech.fsv.cvut.cz/~smilauer/index.php?id=software`

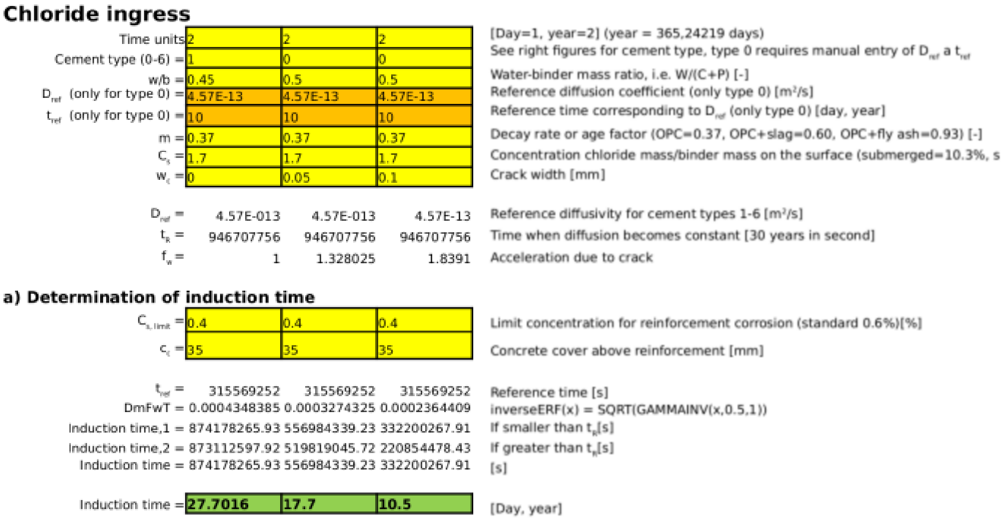

Chloride ingress

Time units	2	2	2	[Day=1, year=2] (year = 365,24219 days)
Cement type (0-6) =	1	0	0	See right figures for cement type, type 0 requires manual entry of D_{ref} a t_{ref}
w/b =	0.45	0.5	0.5	Water-binder mass ratio, i.e. W/(C+P) [-]
D_{ref} (only for type 0) =	4.57E-13	4.57E-13	4.57E-13	Reference diffusion coefficient (only type 0) [m²/s]
t_{ref} (only for type 0) =	10	10	10	Reference time corresponding to D_{ref} (only type 0) [day, year]
m =	0.37	0.37	0.37	Decay rate or age factor (OPC=0.37, OPC+slag=0.60, OPC+fly ash=0.93) [-]
C_s =	1.7	1.7	1.7	Concentration chloride mass/binder mass on the surface (submerged=10.3%, s
w_c =	0	0.05	0.1	Crack width [mm]
D_{ref} =	4.57E-013	4.57E-013	4.57E-13	Reference diffusivity for cement types 1-6 [m²/s]
t_R =	946707756	946707756	946707756	Time when diffusion becomes constant [30 years in second]
f_w =	1	1.328025	1.8391	Acceleration due to crack

a) Determination of induction time

$C_{s,limit}$ =	0.4	0.4	0.4	Limit concentration for reinforcement corrosion (standard 0.6%)[%]
c_c =	35	35	35	Concrete cover above reinforcement [mm]
t_{ref} =	315569252	315569252	315569252	Reference time [s]
DmFwT =	0.0004348385	0.0003274325	0.0002364409	inverseERF(x) = SQRT(GAMMAINV(x,0.5,1))
Induction time,1 =	874178265.93	556984339.23	332200267.91	If smaller than t_R[s]
Induction time,2 =	873112597.92	519819045.72	220854478.43	If greater than t_R[s]
Induction time =	874178265.93	556984339.23	332200267.91	[s]
Induction time =	**27.7016**	**17.7**	**10.5**	[Day, year]

Figure 3.7: Software CarboChlorCon for chloride ingress modelling

3.2.3.1 Diffusion coefficients for chlorides

The proper determination of diffusion coefficients presents a challenging task, taking into account various cements, concretes, exposure conditions and inverse analysis. The DuraCrete model [72] provides the estimation of the apparent diffusion coefficient from the formula:

$$D_a(t) = D_m(t) = k_e k_c D_{Cl}(t_0) \left(\frac{t_0}{t}\right)^m \gamma_{Da} \tag{3.23}$$

where $k_e \in \langle 0.27, 3.88\rangle$ is the environment factor, $k_c \in \langle 0.79, 2.08\rangle$ is the curing factor, $D_{Cl}(t_0)$ is the measured diffusion coefficient determined at the time t_0, $m \in \langle 0.2, 0.93\rangle$ is the decay rate

Binder type	Decay rate factor m [-]
Ordinary Portland Cement (OPC)	0.37
OPC + silica fume	0.39
OPC + slag	0.60
OPC + fly ash	0.93

Table 3.1: Decay rate factor m for different binder compositions in a spray/splash zone [72, Tab. 8.6]

factor and $\gamma_{Da} \in \langle 1.25, 3.25 \rangle$ is the partial factor. In our notation, $D_a(t) = D_m(t)$ and $t_0 = t_{ref}$. Tab. 3.1 gives an example of decay rate factors for a spray/splash zone [72, Tab. 8.6].

The experimental data for concretes exposed to a spray zone for 10-years provided more accurate results [105]. The authors stated that the DuraCrete model for a spray zone strongly underestimates the long-term profile, leading to the under-designed life of a structure [105, p. 50]. Fig. 3.8 summarizes the results from 10-year exposure data in terms of the apparent diffusion coefficient also in dependence of the water-binder ratio. In this particular case, $t_{ref} = 10$ years, m is listed in Tab. 3.1, $D_{ref} = (1 - m)D_a$, t_R can be assumed as 30 years.

3.2.3.2 Example of chloride ingress in submerged salt water

This example uses DuraCrete model. Let us consider regular concrete made from ordinary Portland cement, water-to-cement ratio (w/c)=0.55. According to Fig. 3.8a), D_a is $2.07 \cdot 10^{-12}$ m^{2}s^{-1} at t_{ref}=10 years. According to the DuraCrete model [72, Tab. 8.6], the decay rate factor for concrete submerged in sea water corresponds to $m = 0.30$. In such particular case, $D_{ref} = (1 - m)D_a = 1.45 \cdot 10^{-12}$ m^{2}s^{-1}. Fig. 3.6 shows the evolution of diffusion coefficients for this particular case.

Let us take a characteristic value $C_s = 10.3\%$ by mass of binder [72, Tab 8.5], the critical level for corrosion as 1.35% by mass of binder [72, Tab 8.7] and concrete cover is 100 mm. Tab. 3.2 summarizes initiation times according to Eq. 3.18 with the effect of cracks. It is evident that a macrocrack 0.3 mm decreases the initiation time by almost ten times. The model assumes that the macrocrack width remains constant up to the reinforcement.

Crack width [mm]	Induction time [years]
0.0	53.8
0.1	23.6
0.2	9.8
0.3	4.7

Table 3.2: Induction time for chloride corrosion of submerged concrete, in dependence on original crack width. Cover thickness 100 mm

3.2.3.3 Validation of chloride ingress in a spray zone

The validation relies on the data gathered in a Swedish de-icing highway environment where various concrete compositions were exposed to spray/splash conditions [105]. Experimental data are compared with the three models described above; CMT, ClicConc and DuraCrete.

Chloride profiles measured on concrete blocks of size 400 × 300 × 300 mm after 1.5, 4.5 and 9.8 years of exposure are presented and used for validation. Cores of diameter 100 mm were extruded and analysed, locations of tested blocks are shown in Fig. 3.9. For the detailed description of used data see [105].

First, let us consider ordinary Portland cement OPC I with w/c=0.40 and $m = 0.37$. The reference diffusion coefficient is calculated from Fig. 3.8a) and yields the value $D_a = 0.43 \cdot 10^{-12}$ m^2/s and $D_{ref} = (1 - m)D_a = 0.27 \cdot 10^{-12}$ m^2/s were used for all the models.

Graphs a), b), c) in Fig. 3.10 contain the measured concentration from two samples compared with three presented models. Fig. 3.10b) demonstrates significant variations after a 1.5 year expo-

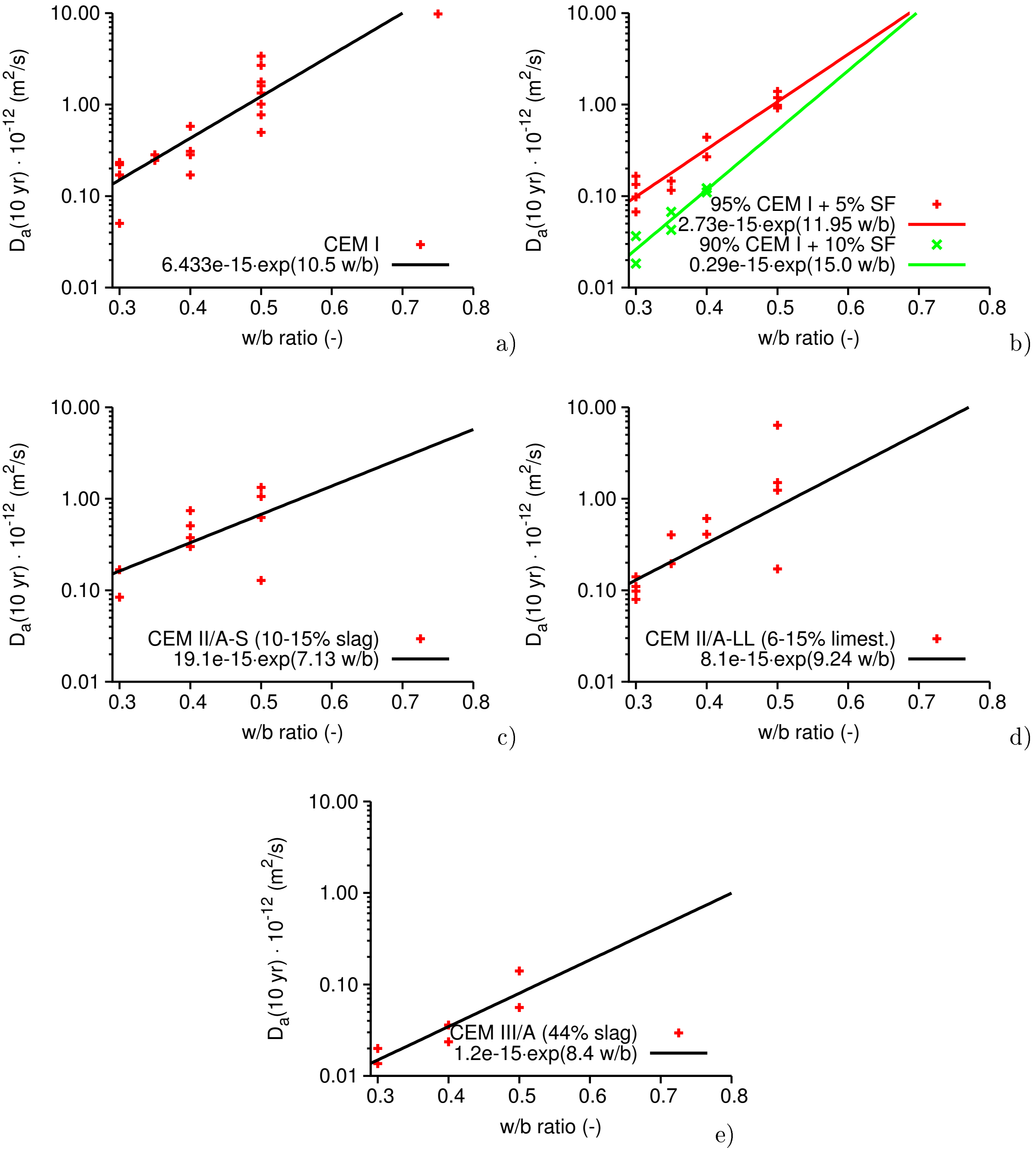

Figure 3.8: Apparent diffusion coefficients for different cement types, 10-year exposure of concrete in a spray zone [105]

sure compared with chloride profile of DuraCrete model. The same C_s value as in the DuraCrete model was used in the simplest CMT model, Fig. 3.10a). Chloride profile after 1.5 years corresponds better compared with DuraCrete, on the other hand, exposure of 4.5 and 9.8 years are underestimated.

The considered values used in ClinConc model of D_{RCM6m} is $1.2997 \cdot 10^{-12}$ m^2/s, age factor n is 0.65 [105]. The environmental data of the free chloride concentration c_s = 1.5 g/l and the annual average temperature T = 10°C (excluding the freezing period). The initial free chloride concentration in the pore solution was assumed as 0.002 g/l. The concrete age at the start of exposure, t_{ex} = 28 days. Other parameters are from the study [105]. Chloride profile obtained by ClinConc model compared with measured data shows Fig. 3.10c).

As can be seen from the Fig. 3.10, CMT model provides the underestimated concentration profiles and ClinConc model slightly overestimated.

The diffusion coefficient decreases over time, depicted in Fig. 3.6. This explains the underestimated CMT results, which uses as a reference apparent diffusion coefficient at 10 years. ClinConc,

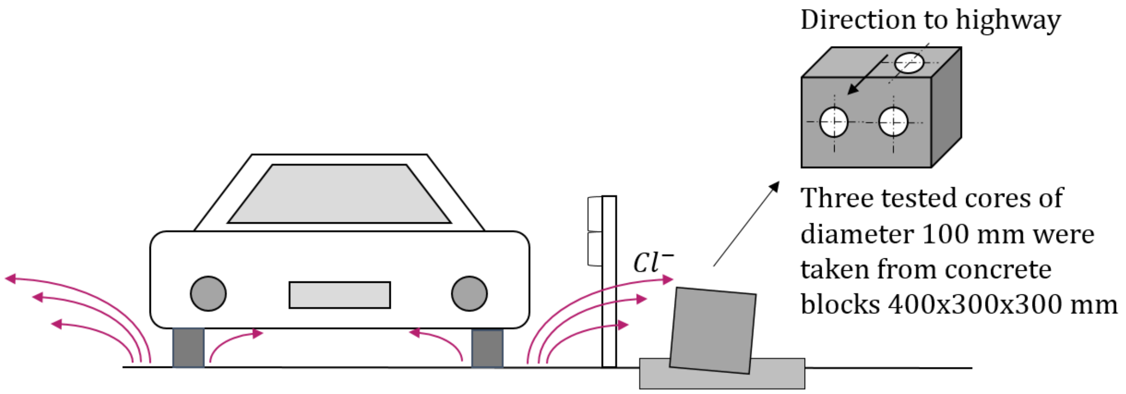

Figure 3.9: Location of tested concrete blocks inserted in steel frame on gravel layer [105].

on the other hand, uses 6-month values and the total chloride concentration, which is in this case 1.1× higher than surface concentration of other two models. Deviations (calculated according to Eq. 3.24) from the measured averaged concentration data at depth of 20 mm are shown in Tab. 3.3.

$$\text{deviation} = \frac{C_{modelled} - C_{measured}}{C_{measured}} \tag{3.24}$$

Exposure [years]	Measured Aver. C [% kg/kg]	CMT [%]	DuraCrete [%]	ClinConc [%]
1.5	0.115	-80.5	2.6	158.5
4.5	0.158	-22.9	40.0	151.8
9.8	0.261	-99.9	-89.6	-36.8

Table 3.3: Comparison of the presented chloride ingress models with measured averaged data at depth 20 mm

The effect of 5% SF is studied further. The same location and exposure was tested with concrete 95% CEM I + 5% SF, w/b=0.40. The reference diffusion coefficient from Fig. 3.8b) yields the value $D_a = 0.33 \cdot 10^{-12}$ m^2/s and $D_{ref} = (1 - 0.39)D_a = 0.20 \cdot 10^{-12}$ m^2/s and it was used for all three models. Apparently, the silica fume addition decreased D_{ref} by 26% when compared to the previous concrete. It is known that silica fume addition increases the autogeneous, drying shrinkage and strength of concrete and such elements are more susceptible to cracking [94]. Fig. 3.11b) shows the validated chloride profiles of DuraCrete model. There is an apparent, small chloride variation in the first 10 mm, signalizing a crack zone. Perfect agreement would recover if the boundary condition were shifted 10 mm inside concrete to encounter for surface cracking. Fig. 3.11a) shows chloride profile where CMT model were used. In ClinConc model the diffusion parameter D_{RCM6m} is $9.85 \cdot 10^{-13}$ m^2/s, the age factor n is 0.79 [105]. Chloride profile obtained by ClinConc model compared with measured data shows Fig. 3.11c). The results obtained by DuraCrete and CMT model are underestimated. Better compliance with measured data show the results obtained by the ClinConc model.

Deviations from the measured averaged concentration data at depth of 20 mm are shown in Tab. 3.4.

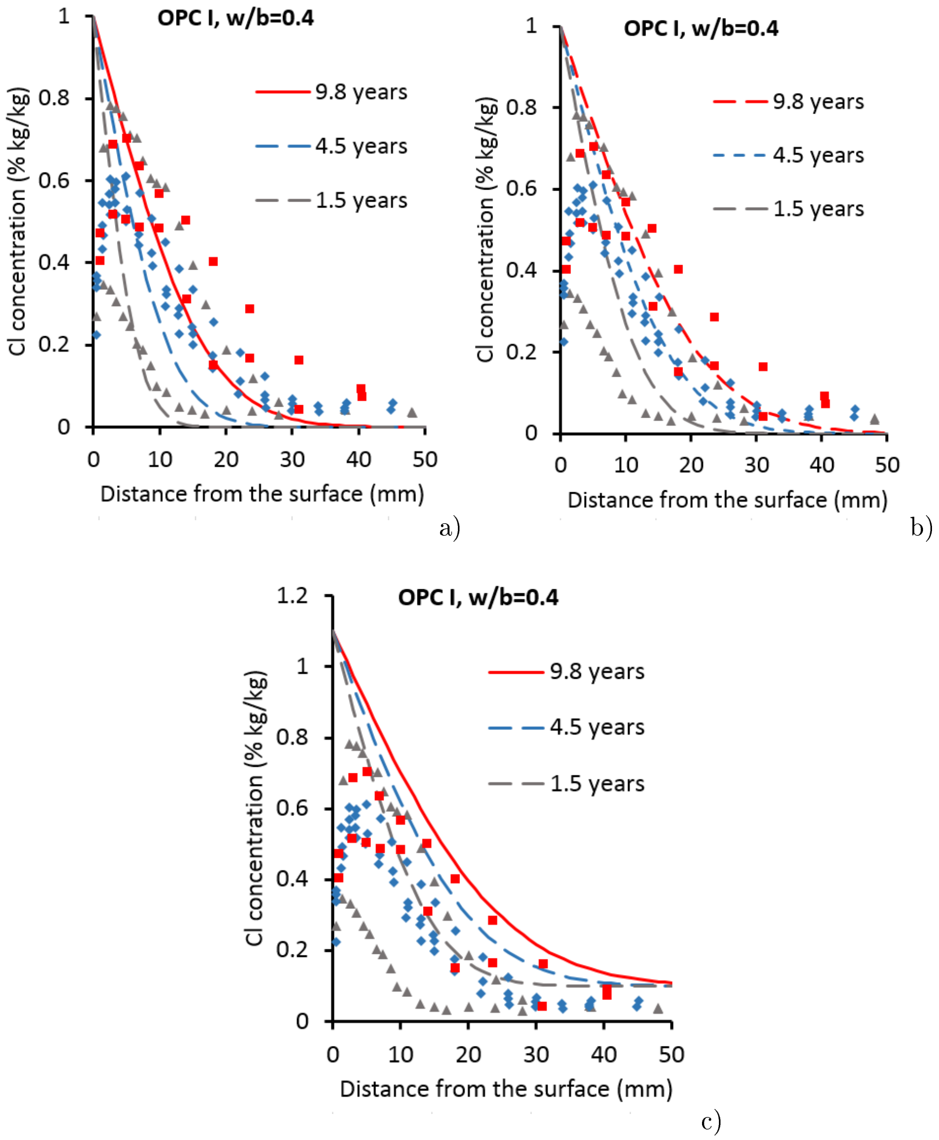

Figure 3.10: Validation of chloride ingress on OPC with w/b=0.40. CMT model a), Duracrete model b), ClinConc model c) [105]

Exposure [years]	Measured Aver. C [% kg/kg]	CMT [%]	DuraCrete [%]	ClinConc [%]
1.5	0.137	-93.6	-47.0	74.2
4.5	0.296	-74.5	-45.9	12.1
9.8	0.326	-99.9	-96.6	-58.9

Table 3.4: Comparison of the presented chloride ingress models with measured averaged data at depth 20 mm

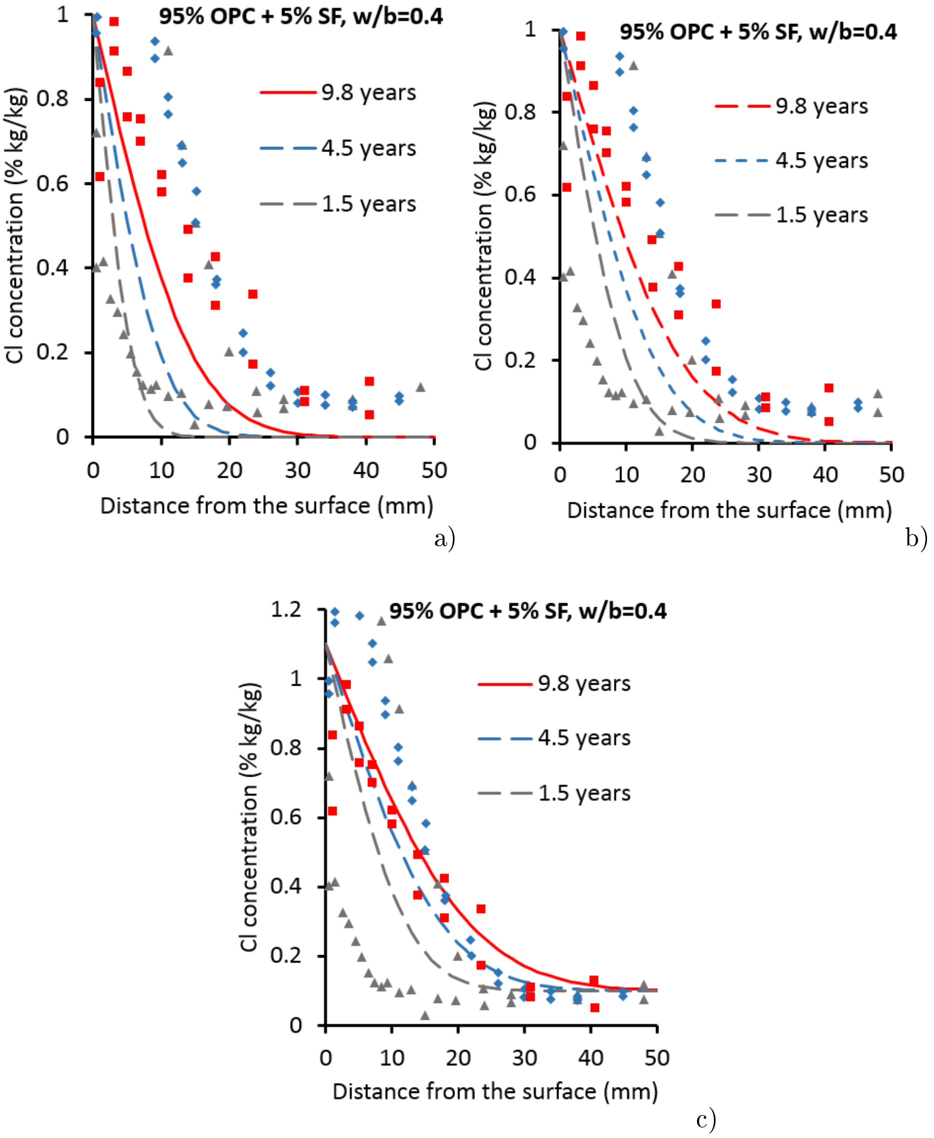

a)

b)

c)

Figure 3.11: Validation of chloride ingress on OPC with w/b=0.40 and with the addition of 5% silica fume. CMT model a), Duracrete model b), ClinConc model c) [105]

3.2.4 Reinforcing bar deterioration

The following model is used for idealized prediction of uniform corrosion and simplified solution for the pitting corrosion. The effective bar diameter reads:

$$d(t) = d_{ini} - \psi 2 x_{corr}(t) \tag{3.25}$$

where $d(t)$ is the evolution of the bar diameter at the time t, d_{ini} is the initial bar diameter, before corrosion has started [mm], both depicted in Fig. 3.12, ψ represents an uncertainty factor of the model with a default value of $\psi = 1$ and x_{corr} is the total amount of corroded steel according to Eq. 2.31.

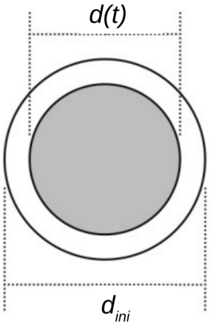

Figure 3.12: Illustration of assumed cross-section loss [87]

The first approach for modelling of pitting (localized) corrosion considers the reduction of reinforcement area in a similar way as the previous uniform corrosion model, depicted in Fig. 3.13a) [87]. The residual cross-section is expressed as follows:

$$d(t) = d_i - x R_{corr} \tag{3.26}$$

where $d(t)$ is the evolution of the bar diameter at the time t, d_i is the initial bar diameter, before corrosion has started [mm], x represents $x_{corr}(t)$ and R_{corr} is a parameter depending on the type of corrosion [-], range described in Eq. 2.31.

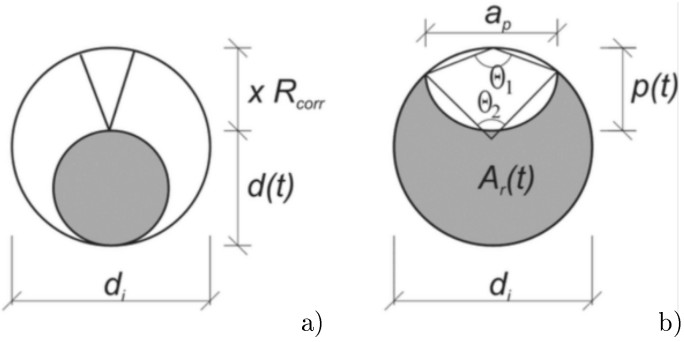

Figure 3.13: Illustrated models for pitting corrosion. Proposed by [87] a), proposed by [112] b)

The second approach is more advanced, proposed by Val and Melchers [112], depicted in Fig. 3.13b). The cross-section area of corroding rebar is calculated as:

$$A_r(t) = \begin{cases} \psi\left(\pi \frac{d_i^2}{4} - A_1 - A_2\right) & p(t) \leq \frac{\sqrt{2}}{2} d_i \\ \psi\left(A_1 - A_2\right) & \frac{\sqrt{2}}{2} d_i < p(t) \leq d_i \\ 0 & p(t) > d_i \end{cases} \tag{3.27}$$

where $p(t) = \psi x_{corr}(t) R_{corr}$ means the radius of the pit in time t, the other parameters are expressed as follows:

$$A_1 = \frac{1}{2}\left[\theta_1\left(\frac{d_i}{2}\right)^2 - a_p\left(\frac{d_i}{2} - \frac{p(t)^2}{d_i}\right)\right],\ A_2 = \frac{1}{2}\left[\theta_2 p(t)^2 - a_p\frac{p(t)^2}{d_i}\right] \tag{3.28}$$

$$a_p = 2p(t)\sqrt{1 - \left(\frac{p(t)}{d_i}\right)^2},\ \theta_1 = 2\arcsin\left(\frac{a_p}{d_i}\right),\ \theta_2 = \arcsin\left(\frac{a_p}{2p(t)}\right) \tag{3.29}$$

3.3 Performance of alkali-silica reaction model

During alkali-silica reaction (ASR), aggregates containing certain forms of silica reacts with alkali hydroxide in concrete to form a gel which adsorbs water from the surrounding cement paste or the environment. Gel formation causes expansive pressure that can damage the concrete.

ASR damage indicates random map cracking or spalled concrete in areas with a frequent supply of moisture, e.g. near the ground behind retaining walls, near joints and free edges in pavements, or in piers or columns subject to wicking action.

Both expansive pressure and deterioration of concrete strength parameters are included in the presented ASR models. The expansive pressure is taken into account by applying initial normal strains in concrete. This extra load is added to other element load of the structure.

Function for volumetric eigenstrain reads:

$$\varepsilon_{ASR}(t) = \varepsilon_{cal}^{\infty}\xi(t)F_M \tag{3.30}$$

where $\varepsilon_{cal}^{\infty}$ is volumetric strain of ASR swelling at infinite time, $\xi(t) \in \langle 0, 1\rangle)$ is the chemical extent of ASR and F_M is the coefficient reflecting moisture influence. It is described later in Section 3.3.2.

3.3.1 Model for ASR kinetics

ASR kinetics is considered according to Ulm [110]:

$$1 - \xi = t_c(\theta, \xi)\dot{\xi} \tag{3.31}$$

where $t_c(\theta, \xi) = k_d/A_0$ is the characteristic time. It has been found that t_c depends on temperature $\theta[K]$ and the ASR extent ξ.

Ulm considers an isothermal, macroscopic stress-free ASR expansion test carried out at constant temperature $\theta = \theta_0$. This test records the volumetric strain ε_{ASR} as a function of time and ASR extent is calculated as:

$$\xi(t) = \frac{\varepsilon_{ASR}(t)}{\varepsilon_{ASR}(\infty)} \tag{3.32}$$

For macroscopically stress-free sample Eq. 3.31 in Eq. 3.32 yields

$$\begin{aligned} \varepsilon_{ASR}(\infty)(1-\xi) &= \varepsilon_{ASR}(\infty)t_c(\theta,\xi)\frac{\dot{\varepsilon}_{ASR}(t)}{\varepsilon_{ASR}(\infty)} \\ \varepsilon_{ASR}(\infty) - \xi\varepsilon_{ASR}(\infty) &= t_c(\theta,\xi)\dot{\varepsilon}_{ASR}(t) \\ \varepsilon_{ASR}(\infty) - \varepsilon_{ASR}(t) &= t_c(\theta,\xi)\dot{\varepsilon}_{ASR}(t) \end{aligned} \tag{3.33}$$

where $\varepsilon_{ASR}(t)$ and $\dot{\varepsilon}_{ASR}(t)$ are measurable functions of time, t_c is the characteristic time which can be determined from a stress-free expansion test. The performed experiments for different constant temperatures show the dependence of t_c on temperature θ [K] and reaction extent ξ [-] as follows [110]:

$$t_c = \tau_c(\theta_0)\lambda(\xi, \theta_0) \tag{3.34}$$

$$\lambda(\xi, \theta) = \frac{1 + exp[-\tau_L(\theta_0)/\tau_c(\theta_0)]}{\xi + exp[-\tau_L(\theta_0)/\tau_c(\theta_0)]} \tag{3.35}$$

In this experimentally determined kinetics function, $\tau_c(\theta)$is a characteristic time [days] and $\tau_L(\theta)$ is a latency time [days]. The use of Eq. 3.35 and Eq. 3.34 in Eq. 3.33 yields after integration [110]:

$$\varepsilon_{ASR}(t) = \varepsilon_{ASR}(\infty)\xi(t),\ \xi(t) = \frac{1 - exp(-t/\tau_c)}{1 + exp(-t/\tau_c + \tau_L/\tau_c)} \tag{3.36}$$

Evolution of ASR extent Eq. 3.32 with depicted time constants τ_c and τ_L shows Fig. 3.14, where τ_c is the characteristic time associated with the gel formation and τ_L is the latency time associated with the dissolution of reactive silica of aggregates [110]. Both constants can be determined from the stress-free isothermal ASR swelling test.

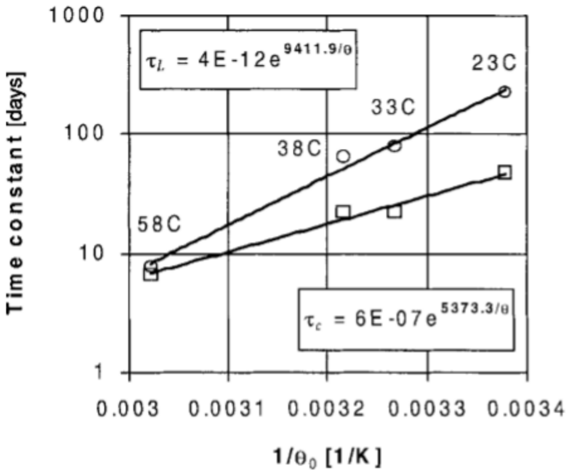

Figure 3.14: Larive's test data of temperature dependency of ASR time constants τ_c and τ_L. Slope of trendlines represents activation energy constants U_c = 5,400 K and U_L = 9,700 K, reproduced from [110]

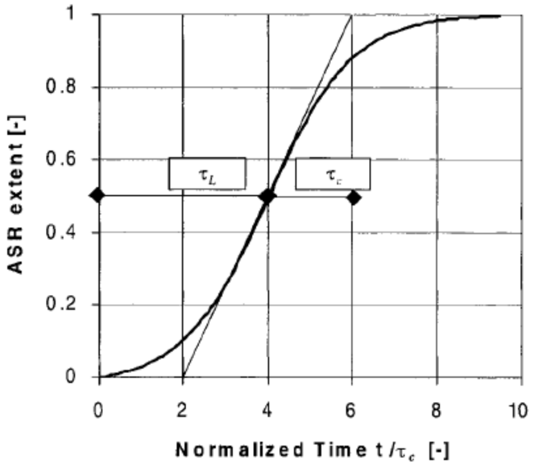

Figure 3.15: Definition of Latency time τ_L and Characteristic time τ_c in normalized isothermal expansion curve ξ=$\varepsilon(t)/\varepsilon(\infty)$, reproduced from [110]

The Ulm explored the temperature dependence of the time constants τ_c and τ_L from stress-free expansion tests for different constant temperatures (23, 33, 38, and 58°C) [110]. Their plots, matching the Arrhenius concept are given in Fig. 3.15.

$$\tau_c(\theta) = \tau_c(\theta_0)exp\left[U_c\left(\frac{1}{\theta} - \frac{1}{\theta_0}\right)\right] \tag{3.37}$$

$$\tau_L(\theta) = \tau_L(\theta_0)exp\left[U_L\left(\frac{1}{\theta} - \frac{1}{\theta_0}\right)\right] \tag{3.38}$$

where

$$U_c = 5400 \pm 500 \text{ K}; U_L = 9400 \pm 500 \text{ K} \tag{3.39}$$

The temperature dependence of the time constants τ_c and τ_L for different constant temperatures (23, 33, 38 and 58°C) is explored in Fig. 3.14. The characteristic and latency times obtained from a parameter analysis are shown in Fig. 3.16, Fig.3.17. According to Larive's experimental data from water saturated tests [33] τ_c (288.15 K) = 80 days and τ_L (288.15 K) = 550 days, τ_c (281.15 K) = 130 days and τ_L (288.15 K) = 1230 days. Under drying conditions, the values for τ_L roughly increase by a factor of 4; and τ_c by 2.5 [53], [110]. Reaction extent ξ=1 means that alkali-silica chemical reaction has stopped.

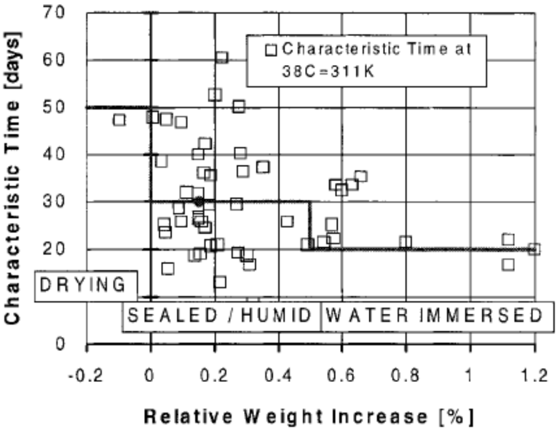

Figure 3.16: Parameter Analysis of Characteristic Time τ_c (θ_0 = 311 K) of ASR Swelling with Regard to Hydral Ambient Conditions, reproduced from [110]

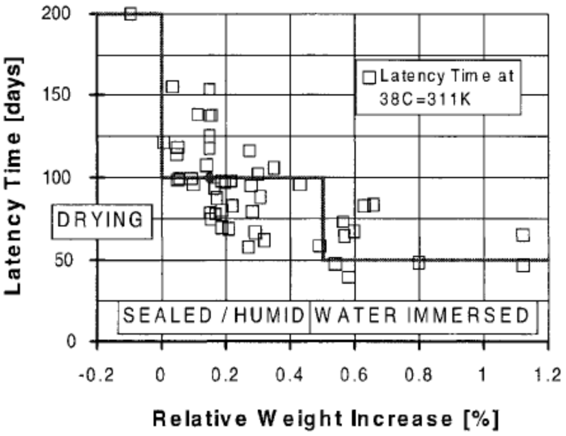

Figure 3.17: Parameter Analysis of Latency Time τ_L (θ_0 = 311 K) of ASR Swelling with Regard to Hydral Ambient Conditions, reproduced from [110]

3.3.2 Influence of moisture

Approximately 75% relative humidity (RH) within concrete is necessary to initiate significant ASR, which is assumed to vary linearly between 75% RH and 100% RH as shown in Fig. 3.18

The coefficient F_M reflects influence of relative humidity h. The function for F_M is approximated as:

$$F_M(h) = \frac{1}{1 - h_{min}}(h - h_{min}) \tag{3.40}$$

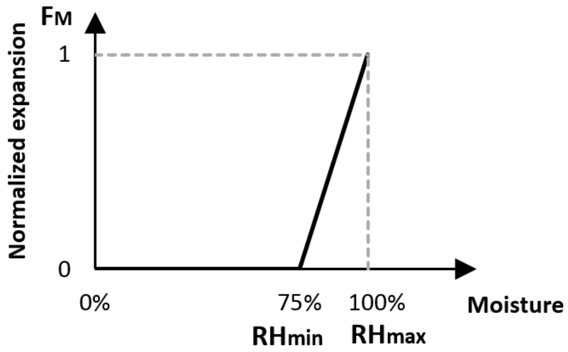

Figure 3.18: Parameter of RH influencing ASR concrete expansion, reproduced from [68]

where h_{min} is relative humidity threshold where ASR begins to appear, 0.75 by default. Other variables will be explained in the following text. The Fig. 3.19 shows example of average annual relative humidity during year.

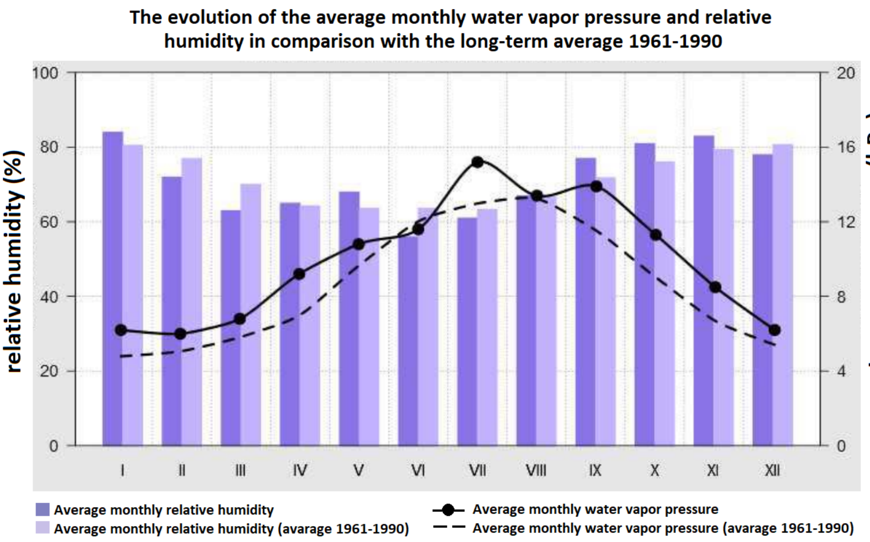

Figure 3.19: The left axis shows relative humidity RH with dark purple average monthly values in Praha-Karlov during year [111]

3.3.3 Prediction of free ASR swelling

$\varepsilon^{\infty}_{cal}$ [-] is the predicted volumetric expansion at infinity time obtained by model proposed previously [69] under no external restraint. It is calculated based on reactive aggregates, amount of reactive silica in the aggregates and value of measured stress-free expansion test done in Poyet's study [83], [57] on samples containing reactive particles only. $\varepsilon^{\infty}_{cal} = 3\varepsilon_{\beta}$, where ε_{β} is defined as follows:

$$\varepsilon_{\beta} = s \cdot p \cdot AC \cdot \varepsilon_F \cdot \frac{A_C}{A_R} \tag{3.41}$$

where ε_F [-/kg/m^3] is the maximal ASR expansion per kg of reactive silica of a mortar having an excess of alkali and containing only reactive particles of fraction F. Its value depends on the amount of aggregate, alkali content and fraction size, etc. For example, in a research performed by Poyet, ε_F ranges from 8.93×10^{-5} to 1.34×10^{-3} %/kg/m^3, see [83] for more details. The Multon lists values from 5.34×10^{-4} to 4.02×10^{-3} %/kg/m^3 in [69] and from 5.03×10^{-4} to

1.15×10^{-2} %/kg/m^3 in [71].

$$\varepsilon_F = \frac{\varepsilon_{MES}}{s \cdot p \cdot AC} \tag{3.42}$$

where ε_{MES} [-] is the measured ASR expansion of the mortar containing reactive particles of fraction F only. Mixtures and measured ASR expansions of mortars studied by Poyet presented in Tab. 3.5.

A_C [kg/m^3 Na$_2$O$_{eq}$] and A_R [kg/m^3 Na$_2$O$_{eq}$] are amounts of consumed and required alkali respectively. AC is total sand content in [kg/m^3]. One of the main assumptions of the model is that the maximum expansion of mortar is achieved if there is enough alkali to react with all the reactive silica of the mixture. This amount of required alkali content A_R is defined as:

$$A_R = r \cdot s \cdot p \cdot AC \tag{3.43}$$

where s is the proportion of quantity of soluble silica [-], p is the proportion of reactive aggregate [-], r states for the amount of required alkali per kg of reactive silica and it is a constant value r = 15.4 %. Value A_C is defined as min(A_R , A_A). A_A is the available amount of alkali for ASR reaction. A_A is defined as difference between initial amount of available alkali A_T [kg/m^3 Na$_2$O$_{eq}$] and alkali content threshold A_0 [kg/m^3 Na$_2$O$_{eq}$] when ASR reaction starts.

$$A_A = A_T - A_0 \tag{3.44}$$

It should be noted that this model does not consider any alkali flow through boundaries inside the structure during the service life. By default, A_0 is equal to 3.7 kg/m^3 Na$_2$O$_{eq}$ [83], but other values in range of 3 – 5 kg/m^3 Na$_2$O$_{eq}$ can be found in the literature [57]

Non-reactive sand (%)			Reactive sand (%)			Measured ASR expansion
F1	F2	F3	F1	F2	F3	ε_{MES} (%)
0	50	25	25	0	0	0.003
25	25	25	0	25	25	0.06
25	50	0	0	0	25	0.06
0	25	25	25	25	0	0.045
25	25	0	0	25	25	0.08

Table 3.5: Mixtures and ASR measured expansions of five mortars compositions studied by [83] and [69]. F1-F3 are size fractions 80 μm-3.15 mm

Value of p depends on the mix ratio of reactive aggregate. Value s depends on amount of reactive silica in aggregates, the moreover common values are: p = 11.1% [69] or 9.4% and 12.4% [70].

3.4 ASR material model

The expansion model [89] takes into account reaction kinetics, alkali content, reactive amount of aggregates, relative humidity and temperature. Due to ASR expansion, mechanical properties decay generally as well. The model has been validated on examples found in literature.

3.4.1 Degradation of material parameters due to ASR reaction

3.4.1.1 Material degradation based on Saouma and Perotti

Degradation of isotropic material parameters due to ASR reaction is based on Saouma and Perotti work [89]:

$$E(t,\theta) = E_0[1 - (1 - \beta_E)\xi(t,\theta)] \tag{3.45}$$

$$f_t(t,\theta) = f_{t,0}[1 - (1 - \beta_f)\xi(t,\theta)] \tag{3.46}$$

$$G_f(t,\theta) = G_{f,0}[1 - (1 - \beta_G)\xi(t,\theta)] \tag{3.47}$$

where $\beta_{E,f,G}$ are residual values of E/E_0, $f_t/f_{t,0}$, $G_f/G_{f,0}$. Default values are β_E=0.1 , β_f=0.6 [30] and β_G=0.6.

3.4.1.2 Material degradation based on Esposito and Hendriks

Degradation of material parameters due to ASR reaction based on Esposito and Hendriks work [30]. To keep the whole procedure simple, model assume isotropic reduction, although expansion may go differently in three orthogonal directions. Knowing ε_{ASR}, it is possible to calculate damage to each mechanical property. The model of Saouma and Perotti [89] suggested linear relationship with degree of reaction, however, experimental data from Esposito and Hendriks [30] testify that decay happens up to an ultimate deformation only. For this reason, we combine both relationships for the reduction of elastic modulus E, tensile strength f_t and fracture energy G_f as follows:

$$E^i = E_0[1 - d^i_E],\ E = \frac{E^1 + E^2 + E^3}{3} \tag{3.48}$$

$$f^i_t = f_{t0}[1 - d^i_f],\ f_t = \frac{f^1_t + f^2_t + f^3_t}{3} \tag{3.49}$$

$$G^i_f = G_{f0}[1 - d^i_G],\ G_f = \frac{G^1_f + G^2_f + G^3_f}{3} \tag{3.50}$$

$$d^i_{E,f,G}(\varepsilon_i) = \begin{cases} 0 & \varepsilon_i \leq \varepsilon_{cr} \\ (1 - \dfrac{\varepsilon_{cr}}{\varepsilon_u - \varepsilon_{cr}}(\dfrac{\varepsilon_u}{\varepsilon_i} - 1))(1 - \beta_{E,f,G}) & \varepsilon_{cr} < \varepsilon_i < \varepsilon_u \\ (1 - \beta_{E,f,G}) & \varepsilon_i \geq \varepsilon_u \end{cases} \tag{3.51}$$

where $\beta_{E,f,G}$ are residual values of E/E_0, $f_t/f_{t,0}$, $G_f/G_{f,0}$ when the expansion is beyond its ultimate value ε_u. Also note that damage occurs differently in three orthogonal directions and going from anisotropic material to isotropic material uses averaging according to Eq. 3.48, 3.49, 3.50.

Reaction extent coefficient ξ run independent on stress, which in the case of a constrained element causes a substantial material degradation, although the constrained conditions reduce the ASR reaction. To ensure the stress-depended kinetics, the ξ could be reduced by the ratio of the reduced and non-reduced volumetric strain from the previous step. This phenomena should be another point of future development.

3.4.2 Volumetric ASR strain

The general equation for the incremental volumetric ASR strain is based on Saouma study [89]-Eq. 5, expressed as:

$$\dot{\varepsilon}_V(t) = \Gamma_t(f'_t \mid w_c, \sigma_I \mid COD_{max})\Gamma_c(\overline{\sigma}, f'_c)F_M(h)\dot{\xi}(t,\theta)\varepsilon^{\infty}_{cal} \mid_{\theta=\theta_0} \tag{3.52}$$

modified and used in following form:

$$\dot{\varepsilon}_V(t) = \underbrace{\Gamma_t\Gamma_c(\overline{\sigma}, f'_c)F_M(h)\dot{\xi}(t)\varepsilon^{\infty}_{cal}}_{\text{Only considered}} + \Gamma_t\dot{\Gamma}_c(\overline{\sigma}, f'_c)F_M(h)\xi(t)\varepsilon^{\infty}_{cal} + ...\dot{\Gamma}_t, \dot{\Gamma}_c, \dot{f}'_c, \dot{F}_M, ... \tag{3.53}$$

where Γ_c reflects effect of compressive stresses by [89]-Eq. 10, Γ_t accounts for the influence of tensile cracking (assumed here as 1), F_M is the effect of relative humidity which is already accounted for in Eq. 3.30. For this reason equals to one. Eq. 3.53 considers further only the most relevant first term and is rewriten in incremental form as:

$$\Delta\varepsilon_V(t_i) = \Gamma_t\Gamma_c(\overline{\sigma}_{i-1}, f'_{c_{i-1}})F_M(h_{\bar{i}})\varepsilon^{\infty}_{cal}(\xi(t_i) - \xi(t_{i-1})), \quad \bar{i} = (i + (i-1))/2 \tag{3.54}$$

Reduction Γ_c due to compressive stress is considered as follows:

$$\Gamma_c = \begin{cases} 1 & if\ \overline{\sigma} \geq 0 \quad \text{Tension} \\ 1 + \dfrac{e^{\beta}\overline{\sigma}}{1 + (1 - e^{\beta})\overline{\sigma}} & if\ \overline{\sigma} < 0 \quad \text{Compression} \end{cases} \tag{3.55}$$

$$\overline{\sigma} = \frac{\sigma_I + \sigma_{II} + \sigma_{III}}{3|f_c'|} \tag{3.56}$$

where the shape factor β is -2 by default by [89, Tab. 2] and f_c is compressive strength.

Under constrained conditions, ASR expansion develops depending on the stress state. It is known that compressive stress beyond approximately -10 MPa stops ASR expansions, which needs to be reflected for strain redistribution into principal direction [12]. Similarly to Saouma [89, Fig. 5], weight factors are assigned to three directions. Let us assume that directions of principal stresses σ_I , σ_{II}, σ_{III} are known. Expansion is then assigned to each principal stress direction according to a weight factors W_1', W_2', W_3'. When compressive stress reaches -0.3 MPa, the weight factor decreases until maximum stress -10 MPa is reached in that direction. This situation is depicted in Fig. 3.20.

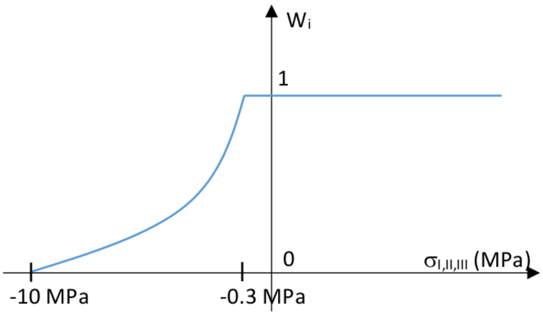

Figure 3.20: Weight factor for ASR expansion

For compressive stress σ_i under -0.3 MPa, the following decay function is used, according to [54] where $\sigma_L \approx$ -0.3 MPa and $\sigma_u \approx$ -10 MPa, see Fig. 3.20.

$$W_i(\sigma_i) = \begin{cases} 1 - \frac{1}{log\frac{\sigma_u}{\sigma_L} log(\sigma_i/\sigma_L)}, & \text{for } \sigma_i < -0.3 \text{ MPa} \\ 1, & \text{for } \sigma_i \geq -0.3 \text{ MPa} \end{cases} \tag{3.57}$$

The weight factors need to be normalized as:

$$W_i = \frac{W_i'}{\sum_{i=1}^{3} W_i'} \tag{3.58}$$

and three principal strains from ASR are assigned as

$$\Delta\varepsilon_{ASR,i} = W_i \Delta\varepsilon_V(t_i) \tag{3.59}$$

This new approach simplifies the procedure outlined by [89, Fig. 5] where several stress state cases were treated individually. The proposed model is derived from free expansion tests. The model works in 2D and 3D stress state by limiting expansion when compressive load is present in a principal direction. In case of hydrostatic compression lower than -10 MPa, no ASR expansion occurs. The majority of structures is exposed to thermal field hence ASR usually proceeds faster close to the surface due to the higher average temperature. Since the surface remains often unloaded and the stress vector on the surface is equal to zero, dominant expansion happens perpendicular to surface which induces small compressive load and delamination of layers.

3.4.3 Free ASR expansion in mortar prism

Presented validation compares experimental data proposed by Multon [69], [68] and results obtained by ASR model described in previous Chapter 3.3. ASR expansion was measured on mortar prisms with dimensions 20 × 20 × 160 mm and with different alkali contents; a) 6.2, b) 13.4 and c) 8.1 kg/m^3, see Tab. 3.6.

Variable	Symbol	Values for a), b), c)			Source
Required alkali per react. silica	r	15.4%			[83]
Reactive silica	s	12.4%	9.4%	11.1%	[69], [68]
Reactive particles in sand	p	30%			[69]
Sand mass	AC	1613.4 kg/m^3	1634.4 kg/m^3	1512 kg/m^3	[69], [68]
ASR measured strain	ε_F	0.0045%/kg/m^3	0.00055%/kg/m^3	0.0115%/kg/m^3	[69], [68]
Amount of required alkali	A_R	9.24 kg/m^3	7.01 kg/m^3	8.66 kg/m^3	calculated
Total alkali in mortar	A_T	6.2 kg/m^3	13.4 kg/m^3	8.1 kg/m^3	[69], [68]
Threshold alkali in concrete	A_0	3.7 kg/m^3			[83]
Characteristic time	τ_c	20 days	20 days	30 days	
Latency time	τ_L	20 days	20 days	10 days	

Table 3.6: Summarized parameters for validation of free ASR expansion

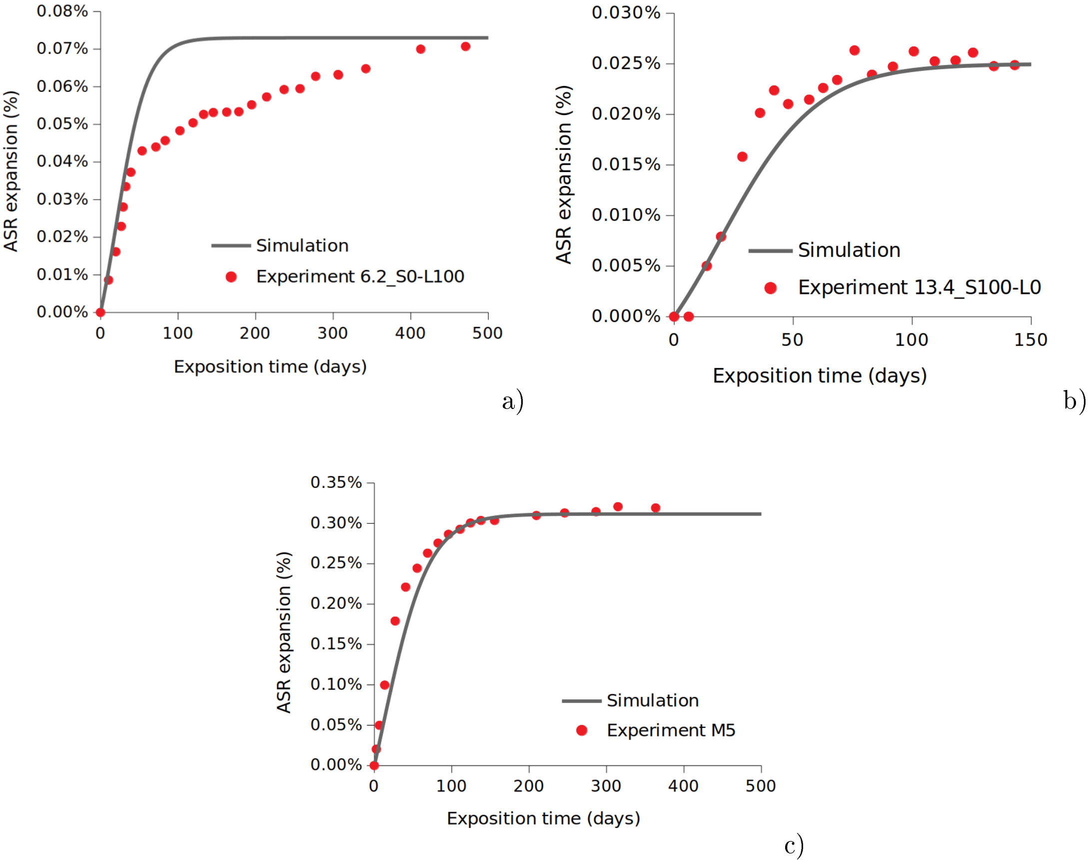

a)

b)

c)

Figure 3.21: Validated ASR expansion of mortars with alkali content 6.2 kg/m^3 Na$_2$O$_{eq}$ [70]a), alkali content 13.4 kg/m^3 Na$_2$O$_{eq}$ [70]b), alkali content 8.1 kg/m^3 Na$_2$O$_{eq}$ [71]c)

The particle size distribution of the samples was 70% of non-reactive aggregates and 30% of reactive aggregate with different fractions a) large aggregates 1.25-3.15 mm b) small aggregates 80-160 μm and c) medium aggregates 630-1250 μm.

Fig. 3.21 shows a simulated ASR expansion in time compared to the measured data. The model provides satisfactory and real ASR expansions with given parameters. The calculation procedure for variant b) is depicted in Eq. 3.60.

$$\begin{aligned}
\varepsilon_\beta &= s \cdot p \cdot AC \cdot \varepsilon_F \cdot \frac{A_C}{A_R} = 9.4\% \cdot 30\% \cdot 1613\ \mathrm{kg/m^3} \cdot 0.00055\% \cdot \frac{7.01\ \mathrm{kg/m^3}}{7.01\ \mathrm{kg/m^3}} = 0.025\% \\
\varepsilon_F &= \frac{\varepsilon_{MES}}{s \cdot p \cdot AC} = \frac{0.025\%}{9.4\% \cdot 30\% \cdot 1613\ \mathrm{kg/m^3}} = 0.00055\% \\
A_R &= r \cdot s \cdot p \cdot AC = 15.4\% \cdot 9.4\% \cdot 30\% \cdot 1613\ \mathrm{kg/m^3} = 7.01\ \mathrm{kg/m^3} \\
A_C &= min(A_T - A_0, A_R) = (13.4\ \mathrm{kg/m^3} - 3.7\ \mathrm{kg/m^3}, 7.01\ \mathrm{kg/m^3}) = 7.01\ \mathrm{kg/m^3}
\end{aligned} \tag{3.60}$$

3.4.3.1 Effect of aggregate size on ASR expansion

The mortar prism Fig. 3.60-b) is analysed with different fractions of reactive particles. The kinetics of the ASR expansions during 500 days are shown in Fig. 3.22. ASR expansion of mortar after 500 days with 30% of reactive particles of fracture 160-315 μm (M3) is 0.00057, 0.00316 for 315-630 μm (M4) reactive particles, 0.00328 for 630-1250 μm (M5) reactive particles and 0.00267 for 1250-2500 μm (M6) reactive particles.

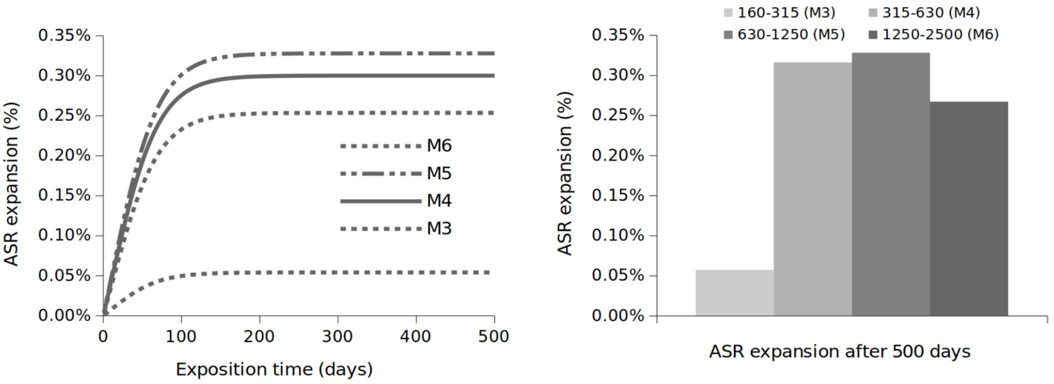

Figure 3.22: ASR-expansions of mortars containing 30% of reactive particles of size 160–315 (M3), 315–630 (M4), 630–1250 (M5), 1250–2500 μm (M6) and 70% of continuous 0–2500 μm non-reactive sand [68]

3.4.4 Material degradation during free expansion

In the past, several experiential studies have been carried out, focusing on the degradation of material parameters due to ASR reaction. Most of them show that the compressive strength is not decreasing, therefore it is not a reliable parameter to detect ASR swelling, e.g. [47, Fig. 2]. For this reason presented validations deal with degradation of stiffness and tensile strength in ASR affected concrete. The presented validations use measured data by Ahmad for mix B [1] compared with the selected models based on Saouma and Perotti [89] and Esposito and Hendriks [30], described in Chapter 3.4.

The specimens were tested in water at temperature 38°C. The Young's modulus is measured on cylindrical specimens with sizes of 150 × 300 mm. The splitting tensile strength is tested on cylindrical specimens with diameter 100 mm and height 100 mm.

ASR kinetics in Fig. 3.23 was fitted to measured data with the parameters presented in the Tab. 3.7.

The following Fig. 3.24, Fig. 3.25 and Fig. 3.26 compares experimental data of E and f_t degradation with results obtained by models based on Saouma and Perotti [89] and Esposito and Hendriks [30]. The following material parameters were used, summarized in the Tab. 3.7.

The used models provide good prediction of Young's modulus and tensile strength. The Esposito model also describes the initial delay and faster increase of degradation. On the other hand, formulation and implementation is a little bit complicated than the Saouma model.

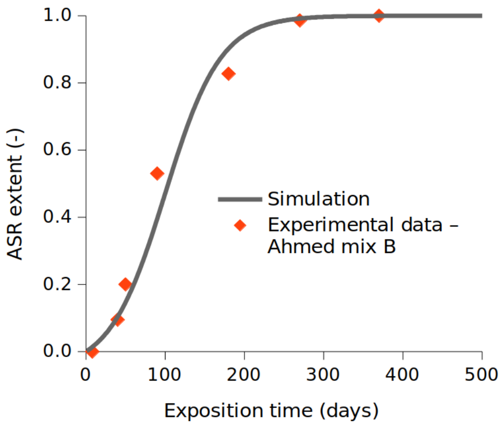

Figure 3.23: Validation of ASR extent proposed by Ahmed for the Mix B [1]

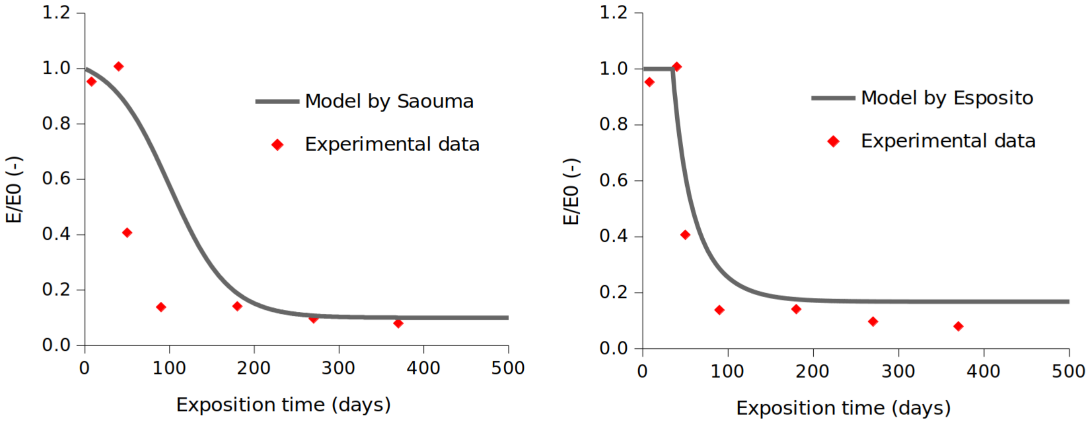

Figure 3.24: Validation of Young's modulus degradation in ASR-affected concrete during free expansion, [30]

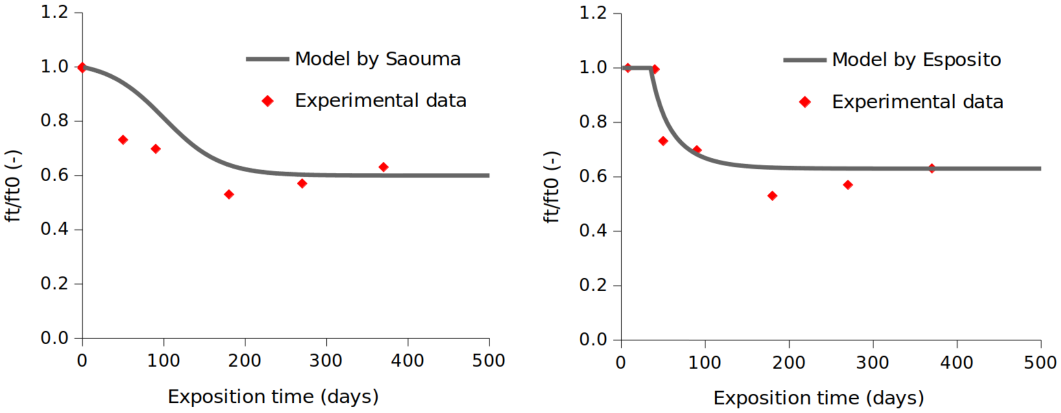

Figure 3.25: Validation of tensile strength degradation in ASR-affected concrete during free expansion, [30]

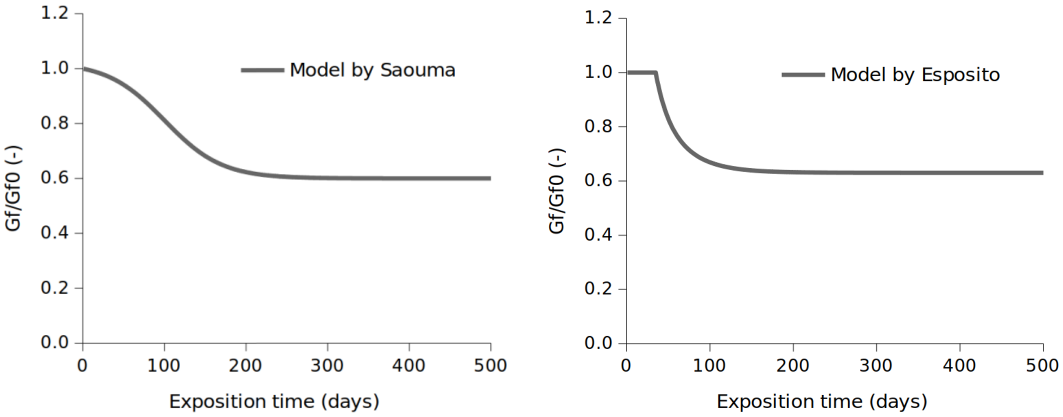

Figure 3.26: Prediction of fracture energy in ASR-affected concrete in free expansion (no validation data available)

Variable	Symbol	Value	Remarks [30]
Maximal ASR expansion	$\varepsilon_{cal}^{\infty}$	$0.0008\%/\mathrm{kg/m^3}$	[83]
Characteristic time	τ_c	35 days	
Latency time	τ_L	100 days	
Young's modulus	E_0	$21130\ \mathrm{N/mm^2}$	at 28 days
Tensile strength	$f_{t,0}$	$1.44\ \mathrm{N/mm^2}$	at 28 days
Compressive strength	$f_{c,0}$	$41.0\ \mathrm{N/mm^2}$	at 28 days
Fracture energy	$G_{f,0}$	$0.142\ \mathrm{N/mm}$	$G_{f,0}{=}0.073 f_{cm}^{0.18}$
Cracking strain	ε_{cr}	$6.81{\cdot}10^{-5}$	$\varepsilon_{cr} = \frac{f_{t,0}}{E_0}$
Ultimate strain	ε_u	$6.88{\cdot}10^{-3}$	$\varepsilon_u = \varepsilon_{cr} + \frac{G_{f,0}}{h f_{t,0}}$
Residual value of E/E_0	β_E	0.1	
Residual values of $f_t/f_{t,0}$, $G_f/G_{f,0}$	β_f, β_G	0.6	

Table 3.7: Summarized parameters for validation

3.4.5 Expansive pressure in concrete prism due to ASR reaction

The following example demonstrates ASR in combination with macroscopic external restraint generating macroscopic compressive stress. It is based on experimental data from [47]. Free expansion is measured in concrete prisms with dimensions 100 × 100 × 400 mm and various alkali contents. Expansive pressure of concrete prism is measured under various degree of restraint by apparatus where steel rods provide a certain stiffness during experiment. Scheme of concrete prism in apparatus is shown in Fig. 3.27.

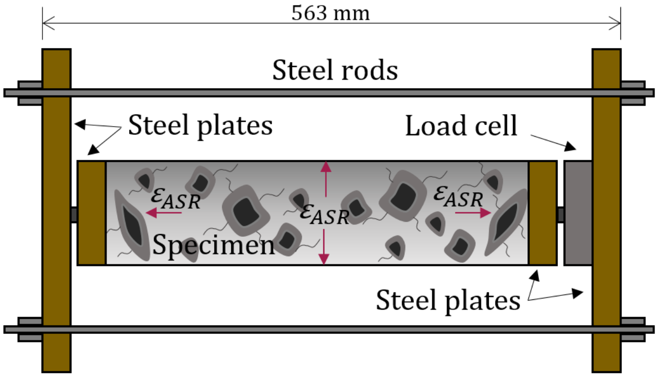

Figure 3.27: Apparatus for measuring of expansive pressure [47]

Different degree of restraints provides various A_s/A_c ratio given by different rod diameter (from 3 to 44 mm). The presented validation uses experimental data for A_s/A_c ratio equal to 30.4, where A_s is transversal sectional area of two steel rods and A_c is transversal sectional area of concrete prism, corresponds to apparatus stiffness of 1702.99 MN/m.

In the first step, the calculation of free ASR expansion is solved and compared with measured data [47]. Example uses general parameters based on Poyet's study [83] and measured ASR expansion proposed by Kagimoto [47].

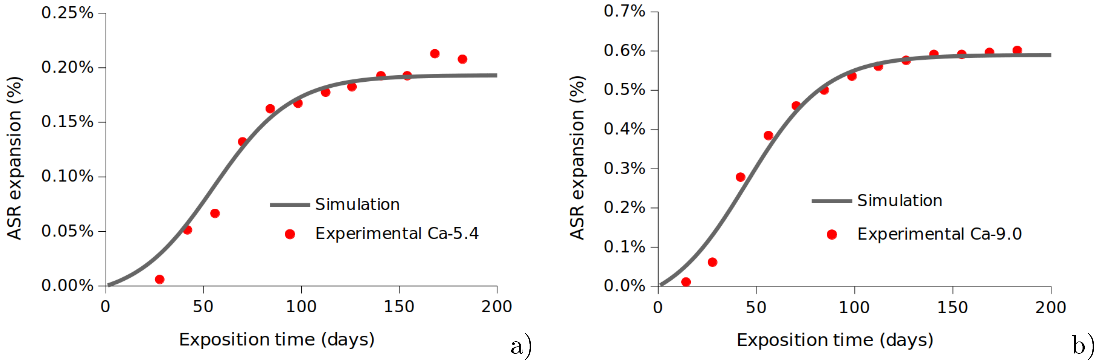

Figure 3.28: Free ASR expansion for alkali content Ca-5.4 a), for Ca-9.0 b) [47]

Fig. 3.28a) shows kinetics of ASR expansion for alkali content 5.4 kg/m^3 Na_2O_{eq} with final expansion 0.0019 after 200 days and Fig. 3.28b) shows kinetics of ASR expansion for alkali content 9.0 kg/m^3 Na_2O_{eq} with final expansion 0.0059 after 200 days. The following material parameters presented in Tab. 3.8 were used in simulation.

In the second step, structural model is set up with elements of dimensions 25 × 25 × 25 mm, see Fig. 3.29. Left side is fixed and the spring has stiffness of 3024.85 MN/m^2 (1702.99 MN/m / 0.563 m) on the right side to simulate the experimental mechanical boundary conditions.

Compressive stresses due to ASR expansion are shown in Fig. 3.30. For case of alkali content 9.0 kg/m^3 Na_2O_{eq} the model predicts realistic results 2.34 MPa after 200 days compared with measured 2.46 MPa, Fig. 3.30b), model output after 200 days in Fig. 3.31b). For second alkali content 5.4 kg/m^3 Na_2O_{eq} yields predicted pressure 0.977 MPa against measured 1.611 MPa (experiment

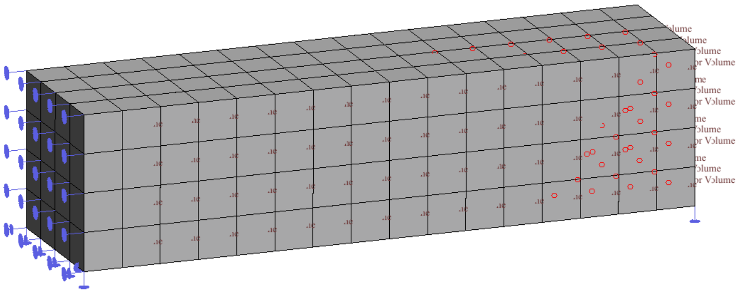

Figure 3.29: Model of concrete prism with fixed left side and spring on the right side (elements with dimensions of 25 × 125 mm).

is 1.65 × higher than the model). see Fig. 3.30a). Software output after 200 days is in Fig. 3.31a). A small pressure of -0.2 MPa was applied in experiment to fix concrete prisms in the frame [47].

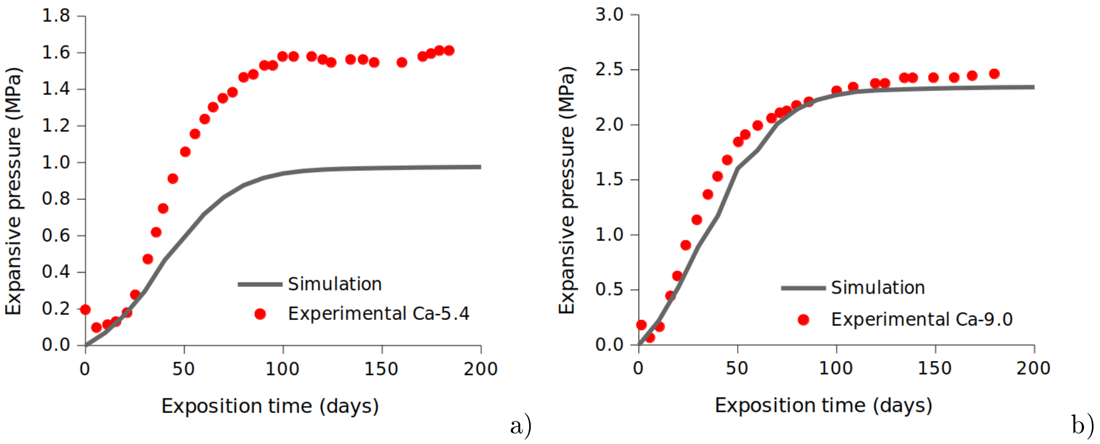

Figure 3.30: Evolution of compressive stress due to ASR expansion. For Ca-5.4 a), for Ca-9.0 b) [47]

Variable	Symbol	Value	Source
Required alkali per reactive silica	r	15.4%	[69]
Proportion of reactive silica	s	12.4%	[70]
Proportion reactive particles in sand	p	30%	[69]
Sand mass	AC	833 kg/m^3	[47]
ASR measured strain	ε_F	0.0525(0.0571)%/kg/m^3	[83]
Amount of required alkali	A_R	4.77 kg/m^3	[83]
Total alkali in mortar for Ca-5.4 (for Ca-9.0)	A_T	5.4 (9) kg/m^3	[47]
Threshold alkali in concrete	A_0	3.7 kg/m^3	[83]
Characteristic time	τ_c	20 days	
Latency time for Ca-5.4 (for Ca-9.0)	τ_L	55(45) days	
Elastic modulus	E	27 GPa	[47]
Compressive strength	f_c	26 MPa	[47]

Table 3.8: Summarized parameters for ASR modelling

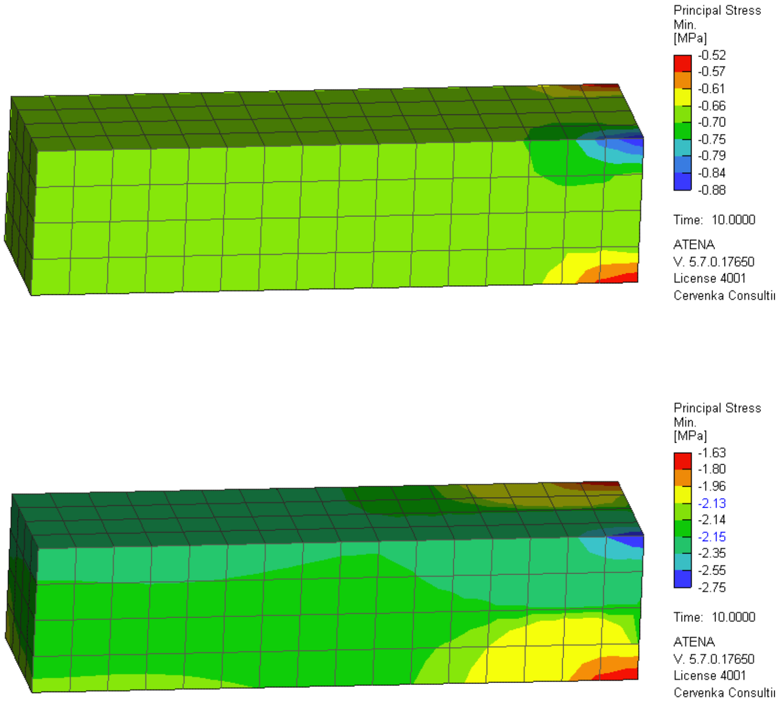

a)

b)

Figure 3.31: Modelled constrained ASR expansion after 200 days without applied pressure of 0.2 MPa. Stresses for alkali content 5.4 kg/m^3 a), stresses for alkali content 9.0 kg/m^3 b)

Kagimoto also provides degradation data of material parameters due to ASR. Fig. 3.32 compares the measured modulus of elasticity for alkali content 5.4 kg/m^3 and 9.0 kg/m^3 with the results obtained with Saouma model, see 3.45. This calculation uses the residual values $\beta_E = 0.9$ for alkali content 5.4 kg/m^3 and $\beta_E = 0.35$ for alkali content 9.0 kg/m^3.

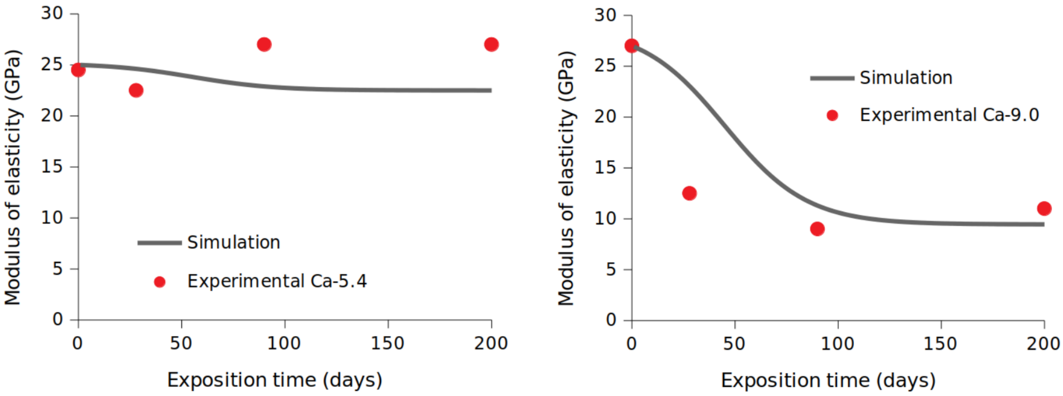

a)

b)

Figure 3.32: Degradation of elasticity modulus for different alkali contents. For Ca-5.4 a), for Ca-9.0 b) [47]

Kagimoto [47] provides data for mortars with varying amounts of alkali from 3.6 to 9.6 kg/m^3, where modulus of elasticity decreased with increasing amounts of alkali. “Compressive strength in concretes with alkali contents of 3.6 and 5.4 kg/m^3 increased with age up to 28 days, and even thereafter rose a little, but that of concretes with alkali contents greater than 6.6 kg/m^3 little rose or decreased with age. Especially, reductions in the modulus of elasticity in concretes with alkali contents greater than 6.0 kg/m^3 after 28 days were remarkable." [47]

The proposed model provides good prediction of elasticity modulus for mortars with higher alkali contents. In the case of mortars with a lower content, it is obvious that the modulus of elasticity is not reduced but rather increased.

3.4.6 Concept of durability modelling

The aim of this work is to develop a software tool combining the presented models for the development, assessment and design of various types of structures and their maintenance. The durability design is based on reliability theory like it is in structural design. The aim is to determine the probability of a given moment similarly to Fig. 2.17, e.g. the moment of concrete cover cracking. Our analysis is based on stochastic calculations using mean values in presented numerical models. This corresponds to the design approach of partial safety factor proposed in Fig 2.16.

Chapter 4

Performance of selected models for structures

Chemo-mechanical models from Chapter 3 are validated on three engineering structures suffering from chloride ingress and carbonation, i.e. a concrete strut of a prestressed bridge in Prague, Czech Republic, and Nougawa bridge, Japan. The models are applied for reinforced concrete bridge in Örnsköldsvik, Sweden. They are capable of predicting serviceability due to chloride ingress with regards to intrinsic and extrinsic factors.

Performance of ASR model is presented on a concrete gravity dam used in a benchmark study.

4.1 Chlorides and carbonation simulation workflow

Modelling workflow of real reinforced structure in Fig. 4.1.

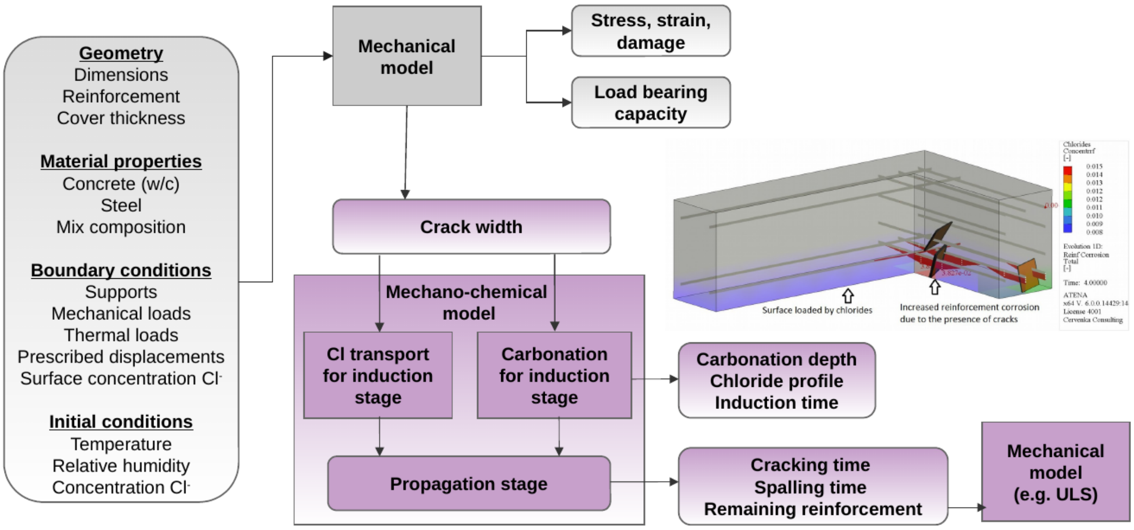

Figure 4.1: Modelling workflow for assessing corrosion and load-bearing capacity

First, the calculation uses a mechanical model where the structure is analysed, including all loads and boundary conditions. The main output of the mechanical calculation is the crack width, which is crucial for transport processes. In the mechano-chemical model, there begins the beneficial part of this work (in the scheme highlighted by purple color), degradation of concrete and reinforcement due to chloride ingress and carbonation affected by the crack width.

Calculation of carbonation depth uses Papadakis model [79] presented in Section 3.1.1. In the case of calculation of chloride profiles is employed DuraCrete model [72], presented in Section 3.2.3. Tang allege, some chlorides are “irreversibly combined into hydrated products by chemical reaction, and others can unbind as the free chloride concentration decreases” by corrosion reaction. This phenomenon is not yet fully understood. Therefore, calculation of chloride profile according to

DuraCrete model [72] does not include a specific description of chloride binding, but its effects is included implicitly in diffusivity. Both initiation models include the effect of cracking proposed by Kwon [52], [51].

Reaching the critical thresholds (critical chloride concentration or carbonation front in the place of reinforcement) determines the initiation time and activates the propagation model, where Liu and Weyer's model [58] is used to determine the corrosion current density i_{corr} in Eq.2.31. In the case of carbonation, value of corrosion current density ranges between 0.1-10 μA/cm^2 (passive corrosion-high corrosion), depends on the quality and the relative humidity of the concrete [76]. Calculation of the corrosion rate and the corroded depth is the same for both corrosion mechanisms, given by Eq. 2.30. The cracking and spalling time of the concrete cover is related to corroded bar depth proposed by DuraCrete model [72]. After spalling of concrete cover, the reinforcement corrodes in direct contact with environment according to [99]. The reinforcement area is reduced with consequences for load-bearing capacity and structure reliability.

4.2 Concrete strut of a pre-stressed bridge

Condition of a prestressed concrete bridge X-567 in Prague was evaluated after 32 years of service. The total width of the bridge is 12 m, the bridge is built as a precast V-frame with spans of 14 + 36 + 14 m. The reinforced concrete strut, marked in Fig. 4.2, is regularly attacked by chlorides from de-icing salts. Its lower part was analysed in order to assess reinforcement corrosion due to chloride ingress and carbonation.

Figure 4.2: Bridge view with the analysed strut

The concrete of the struts was classified as class C35/45. The estimated composition yields CEM I 42.5 N, 350 kg/m^3 and water content of 175 kg/m^3. The strut is reinforced by stirrups with a diameter of 12 mm and vertical bars, the latter with a diameter of 32 mm and the concrete cover of 35 mm.

4.2.1 Concrete strut loaded by carbonation

Validation of carbonation uses the same strut as in the previous example. The surface of the strut was exposed to carbonation with the parameters summarized in Tab. 4.1. The estimated amount of cement content C is 350 kg/m^3 and water content W is 175 kg/m^3. Relative humidity of air RH is given as 0.65, based on data provided by CHMI in Prague-Karlov 3.19. Volumetric fraction of CO_2 in surrounding environment for outdoor air is equal to $3.9{\cdot}10^{-4}$ [-].

The four struts support the bridge on each side (a total of eight struts). The carbonation depth of 15 mm (P2) was measured on the strut from the previous chloride validation and the same value of 20 mm (P1) on the other three struts. The test was carried out by mixed acid-base indicator provided by company GERMANN - Rainbow indicator, its use at test site P1 of the bridge is demonstrated in Fig. 4.3.

The four scenarios for different crack widths were taken; concrete without cracks, maximum crack width of 0.05 mm and 0.1 mm. The Fig. 4.4 shows evolution of carbonation depth for these three scenarios.

Parameters	Concrete strut	Source
C	350 kg/m^3	Estimated composition
W	175 kg/m^3	Estimated composition
RH	0.65	CHMI data 3.19
ρ_c	3150 kg/m^3	Estimated from composition
CO_2	0.00039	

Table 4.1: Input parameters for carbonation

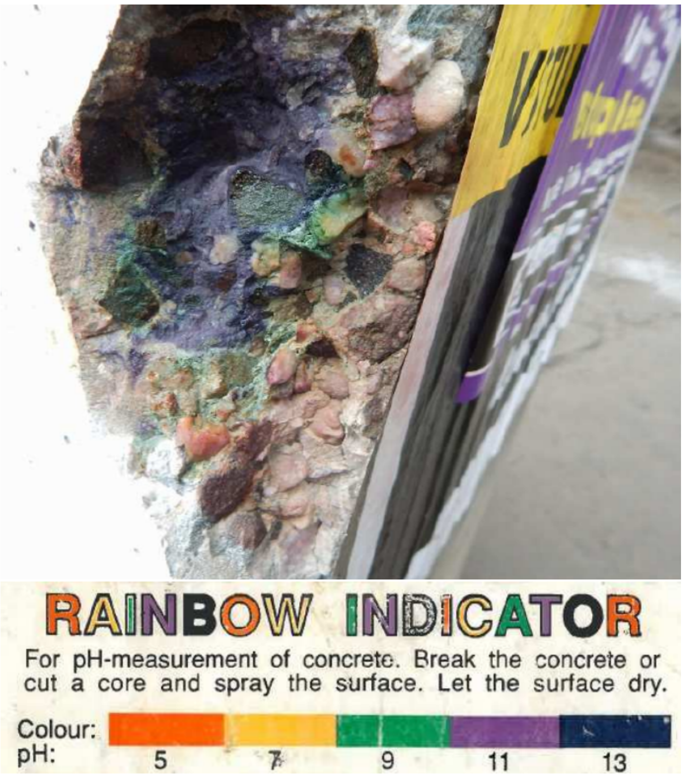

RAINBOW INDICATOR

For pH-measurement of concrete. Break the concrete or cut a core and spray the surface. Let the surface dry.

Figure 4.3: Characteristic evolution of carbonation, test site P1 with measured carbonation depth 20 mm. Rainbow indicator 0-15 mm with pH 5, 15-20 mm with pH 9 and >20 mm with pH 11-13 [46]

For the first case of concrete without cracks, the carbonation depth reaches 12 mm after 32 years. Carbonation would reaches the place of reinforcement after 271 years. In the second case, with the maximum crack width 0.05 mm, the carbonation depth 19 mm corresponds to reaching reinforcement after 110 years. The last scenario of maximum cracks width 0.1 mm reaches carbonation depth 22 mm after 32 years and the induction time in this case is 75 years.

The following Figs. 4.5 - 4.10 show graphical outputs from the analyses for individual crack widths, with corresponding induction times and carbonation depths. The cracks and their maximum widths are artificially created by three point bending to represent their influence on the acceleration of the carbonation process.

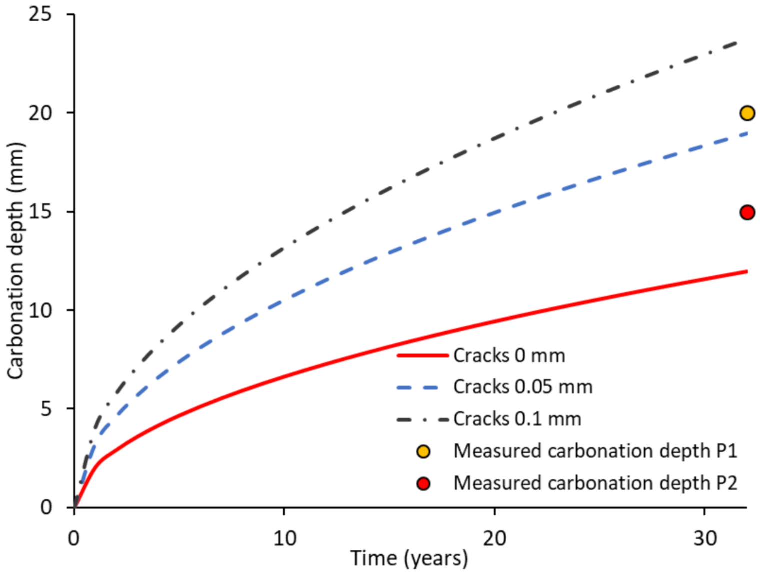

Figure 4.4: Carbonation depths for three scenarios compared with measured data. Measured carbonation depth P2 for strut used in validation and measured carbonation P1 for other struts

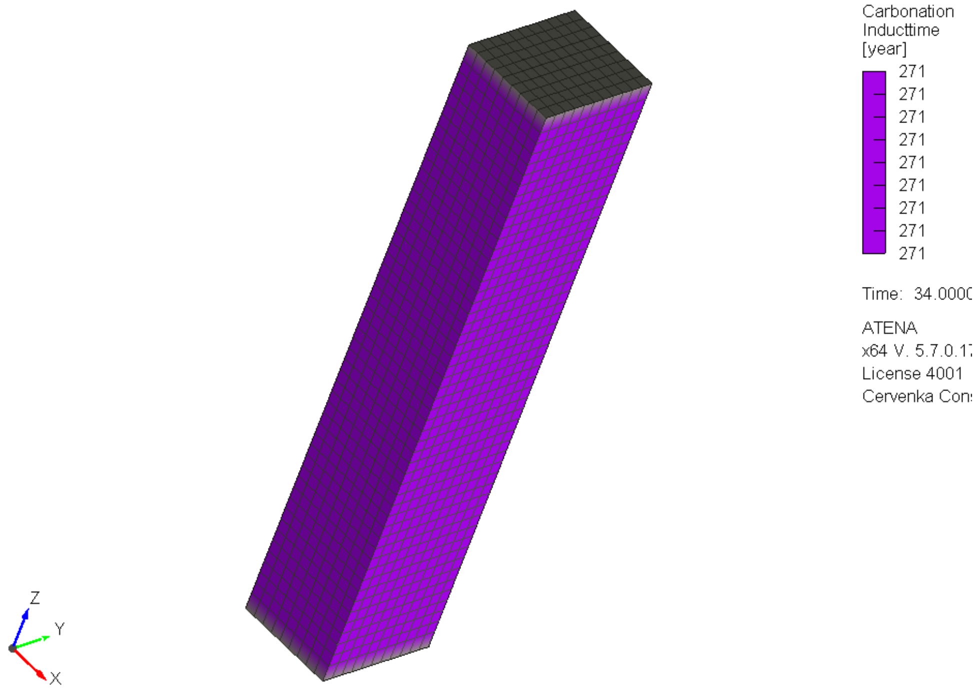

Figure 4.5: Carbonation - induction time for strut with concrete cover 35 mm and crack widht 0 mm

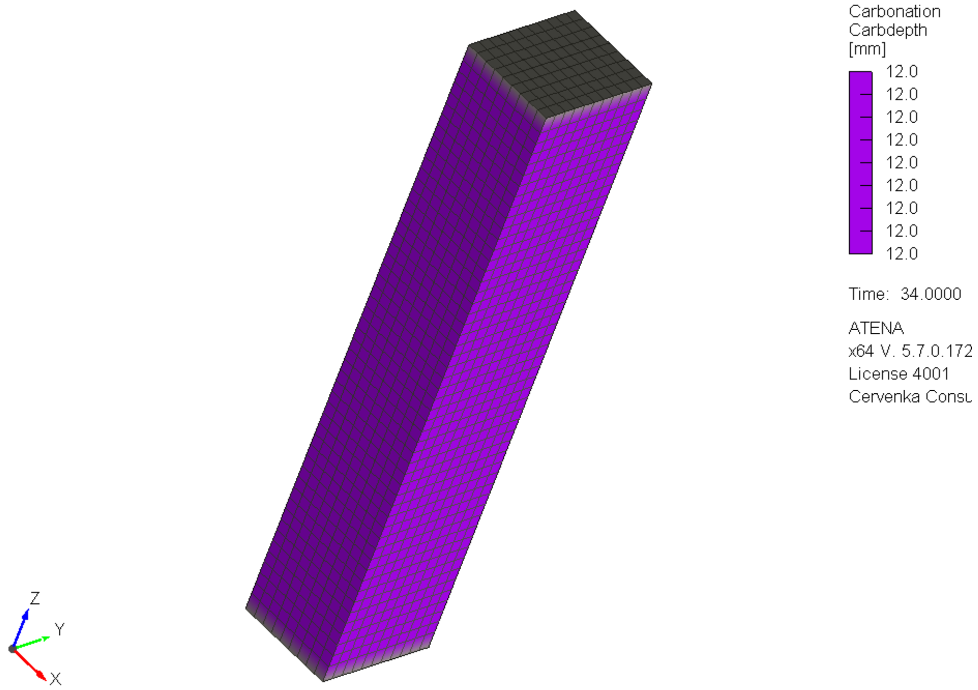

Figure 4.6: Carbonation depth after 32 years for strut with concrete cover 35 mm and crack width 0 mm

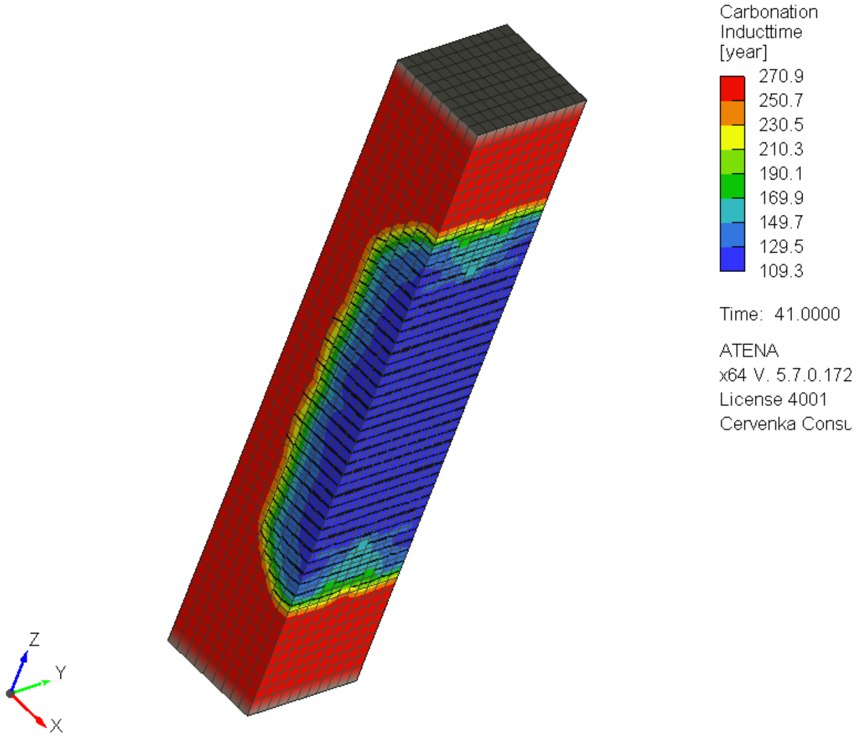

Figure 4.7: Carbonation induction time for strut with concrete cover 35 mm and artificially-induced cracks in three-point bending, maximum crack width 0.05 mm

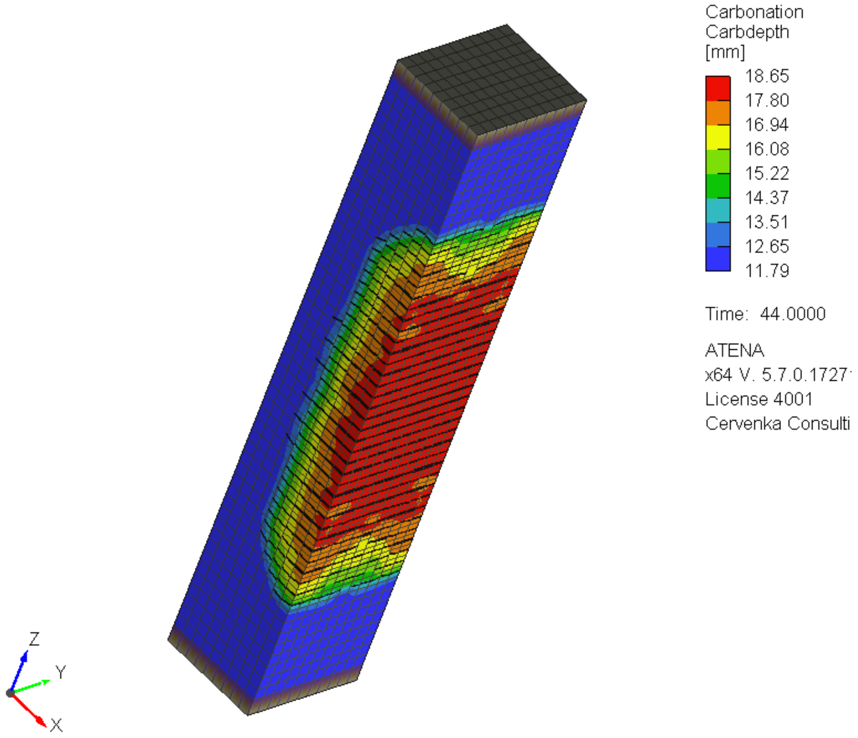

Figure 4.8: Carbonation depth after 32 years for strut with concrete cover 35 mm and maximum crack width 0.05 mm

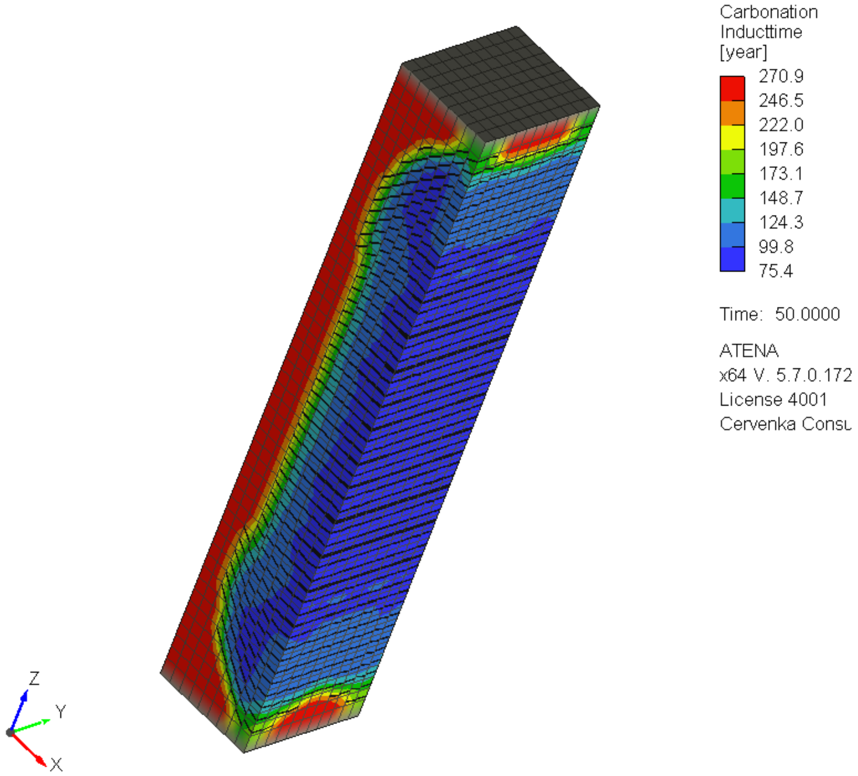

Figure 4.9: Carbonation induction time for strut with concrete cover 35 mm and artificially-induced cracks in three-point bending, maximum crack width 0.1 mm

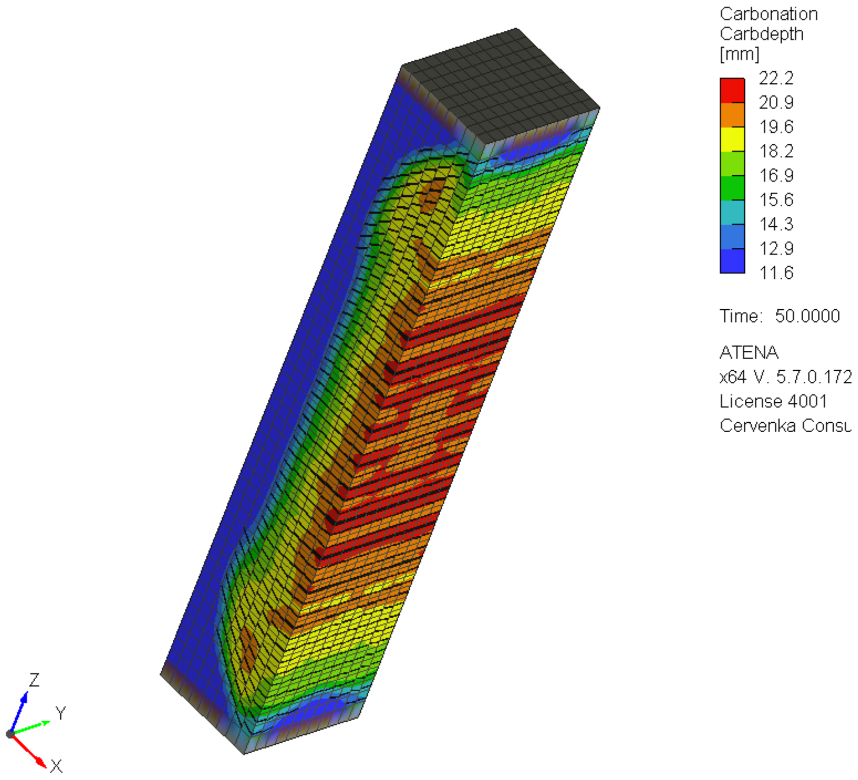

Figure 4.10: Carbonation depth after 32 years for strut with concrete cover 35 mm and maximum crack width 0.1 mm

4.2.2 Concrete strut loaded by chlorides

The surface of the strut was exposed to chlorides with the parameters summarized in Tab. 4.2. According to the DuraCrete model [72, Tab. 8.6], the decay rate factor for concrete in a tidal and splash zone corresponds to $m = 0.37$. The surfaces are loaded by a measured chloride concentration of 1.7% by the binder mass. Chloride measurement was performed with the RCT (Rapid Chloride Test) set provided by company GERMANN - it serves for approximate determination of the chloride ingress in dependence on depth. During the survey, 3 samples from different depths were taken at 12 test sites. In total, 36 concrete samples were taken for chemical analysis. Test sites were usually selected in areas with more pronounced leakage (leaks, binder leaching, cracking etc.) that are the source of increased ingress. A view of tested strut with spalled concrete cover is in Fig. 4.11.

Figure 4.11: Investigation of reinforcement corrosion at the strut with spalled concrete cover [46]

The critical level for corrosion is 0.4% per binder, as required by EN 206-1. The parameters a_1, a_2, a_3 used in Eq. 2.41 are estimated from [72]. Corrosion rate for direct contact with the environment assumes category C3 (coastal and industrial environment) according to table in Fig. 2.26.

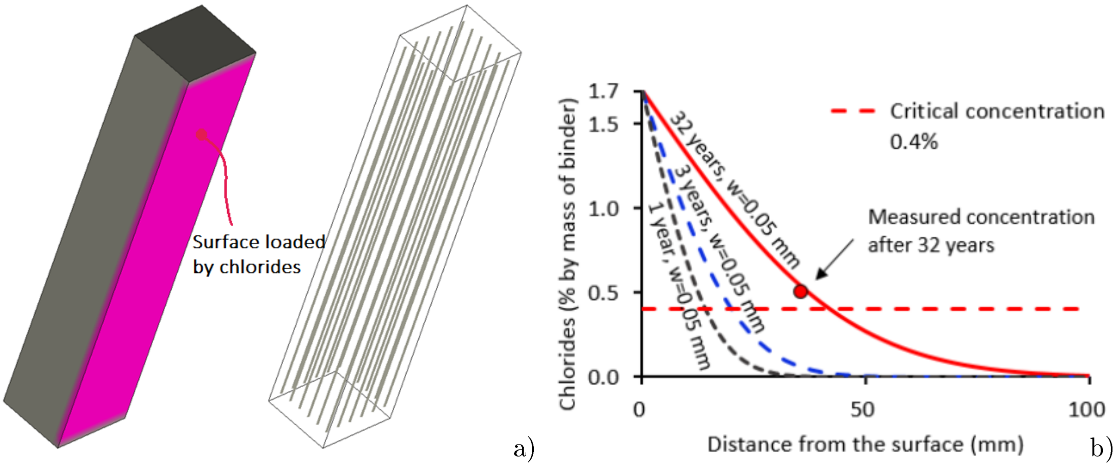

Figure 4.12: Geometry (0.6 × 0.6 m) of the bridge strut with a chloride profile and reinforcement a), chloride profile of the bridge strut for the surface measured concentration of 1.7 % by mass of binder and crack width 0.05 mm b)

Fig. 4.12a) shows the geometry and chloride exposition of the modelled strut. Chloride profiles for the crack width of 0.05 mm are given in Fig. 4.12b). It turned out that a sound concrete

Parameters	Concrete strut	The Nougawa bridge	Source
D_{ref}	$3.95 \cdot 10^{-8}$ m^2/day	$1.2 \cdot 10^{-7}$ m^2/day	Fig. 3.8
m_{coeff}	0.37	0.65	Duracrete [72, Tab. 8.6]
C_s	1.7 % by mass of binder	4 % by mass of binder	Measured values
Cl_{crit}	0.4 % by mass of binder	0.6 % by mass of binder	Duracrete [72, Tab. 8.7]
$f_{t,ch}$	3.2 MPa	2.6 MPa	Estimated from f_c
R_{corr}	2	3	According to [37]
C_{loss}	30 μm/year	35 μm/year	According to category C3 [99]

Table 4.2: Input parameters for chloride ingress

without cracks would yield an unrealistically long induction time, therefore, assumptions of crack widths 0, 0.05 and 0.1 mm were tested further.

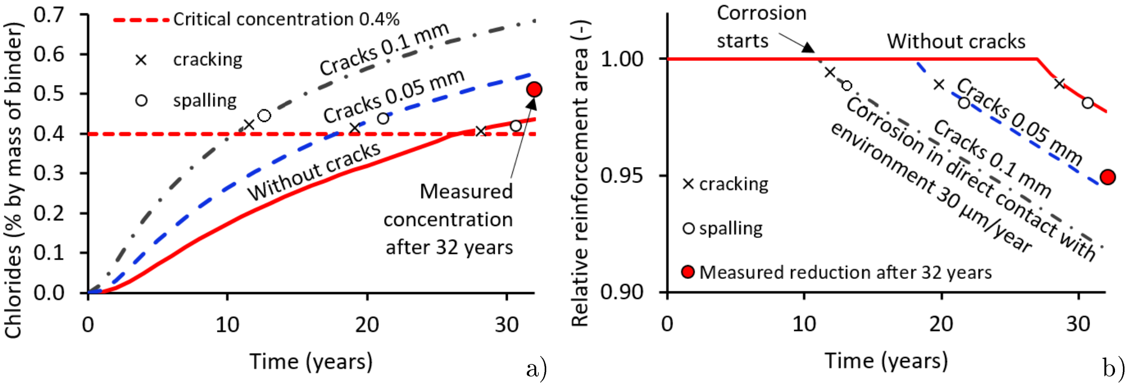

Figure 4.13: Chloride concentrations at the reinforcement depth, concrete cover = 35 mm a), reduction of the reinforcement area during service life b)

Those scenarios are demonstrated in Fig. 4.13. The most realistic assumption favours a crack width of 0.05 mm. In this particular case, the corrosion of reinforcement starts after 18 years, followed by the spalling of the concrete cover after another three years. The concentration of chlorides reaches 0.551% after 32 years at the reinforcement depth while the measured concentration is 0.51% at locations without spalling, depicted in Fig. 4.12b).

The remaining area fraction of reinforcement reaches 0.944 after 32 years of service. This value is in good agreement with the measured value of 0.95, see Fig. 4.13b). Our analysis showed that a crack width of 0.05 mm decreases the initiation time by approximately 1.6 times and the reduction of the reinforcement area is 2.4 times higher compared with a sound concrete where reinforcement corrosion would start after 27 years.

The following Figs. 4.14 - 4.25 show graphical outputs from an analysis of particular crack widths, including corresponding induction time, chloride concentration and corrosion state. The cracks and their maximum widths in Figs. 4.18 - 4.25 are artifically induced by three-point bending in order to demonstrate their influence on the acceleration of chloride ingress.

Our simulation considers a computational time step corresponding to one year. In the case of crack width 0, 0.05 and 0.1 mm, spalling of concrete cover occurs after 12, 22 and 31 years.

The crack width also significantly decreases the period from corrosion initiation to spalling time. The presence of cracks 0.1 mm leads to spalling of concrete cover after 2 years, this is 2 times shorter compared to sound concrete (after 4 years). The direct corrosion with environment take place, leads to the reduction of the reinforcement area 3.7 times higher compared with a sound concrete.

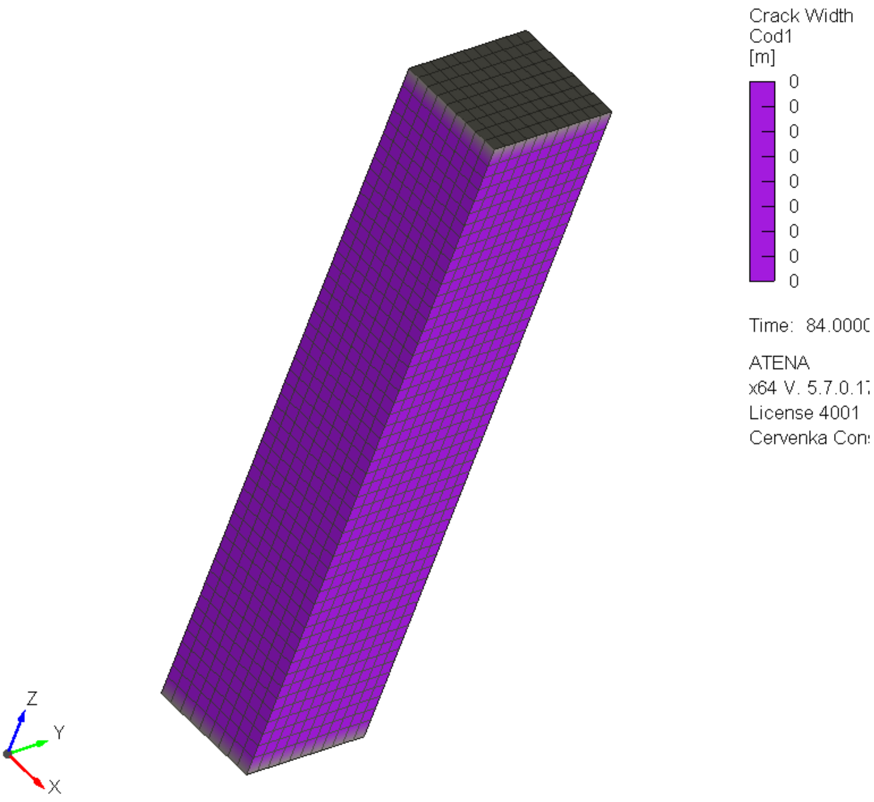

Figure 4.14: Concrete strut with crack width 0 mm

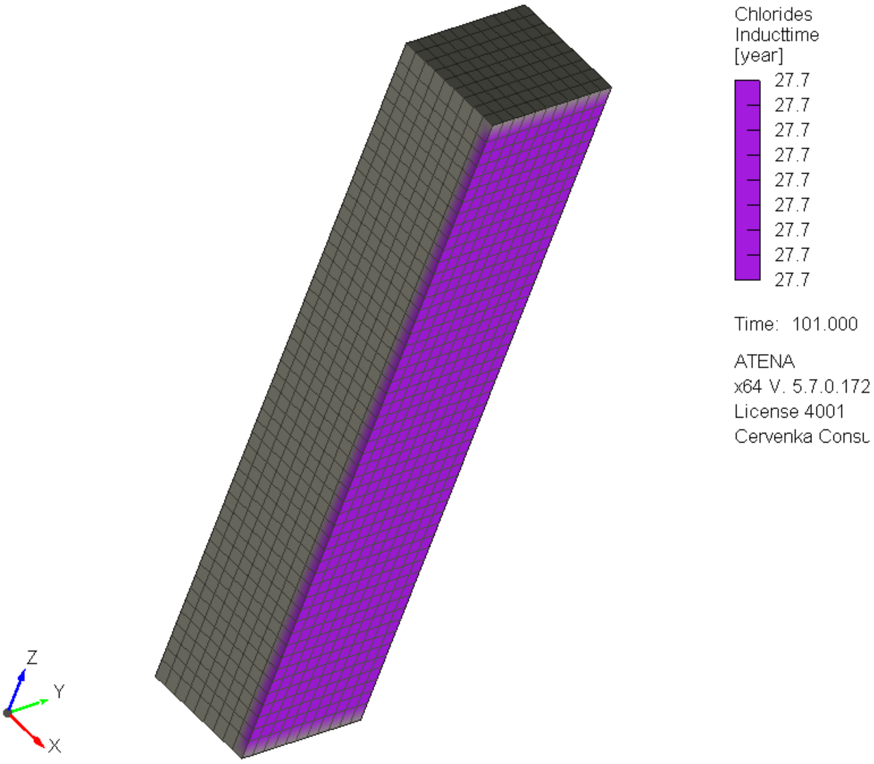

Figure 4.15: Induction time for strut with concrete cover 35 mm and crack width 0 mm

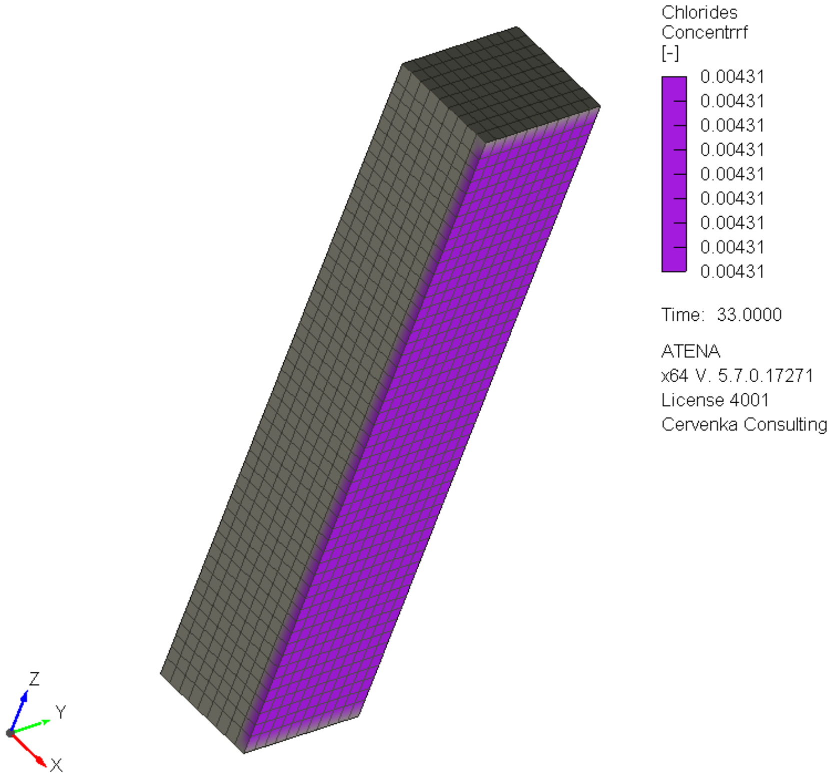

Figure 4.16: Concentration of chlorides (by mass of binder) in the place of longitudinal reinforcement after 32 years for strut with concrete cover 35 mm and crack width 0 mm

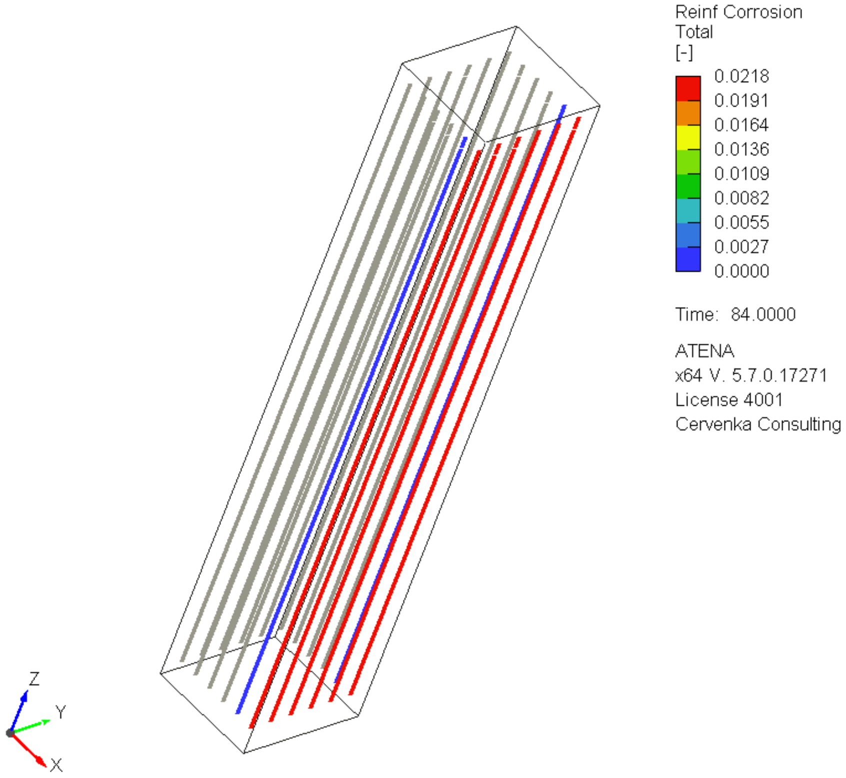

Figure 4.17: Corresponding corrosion of reinforcement after 32 years for crack width 0 mm

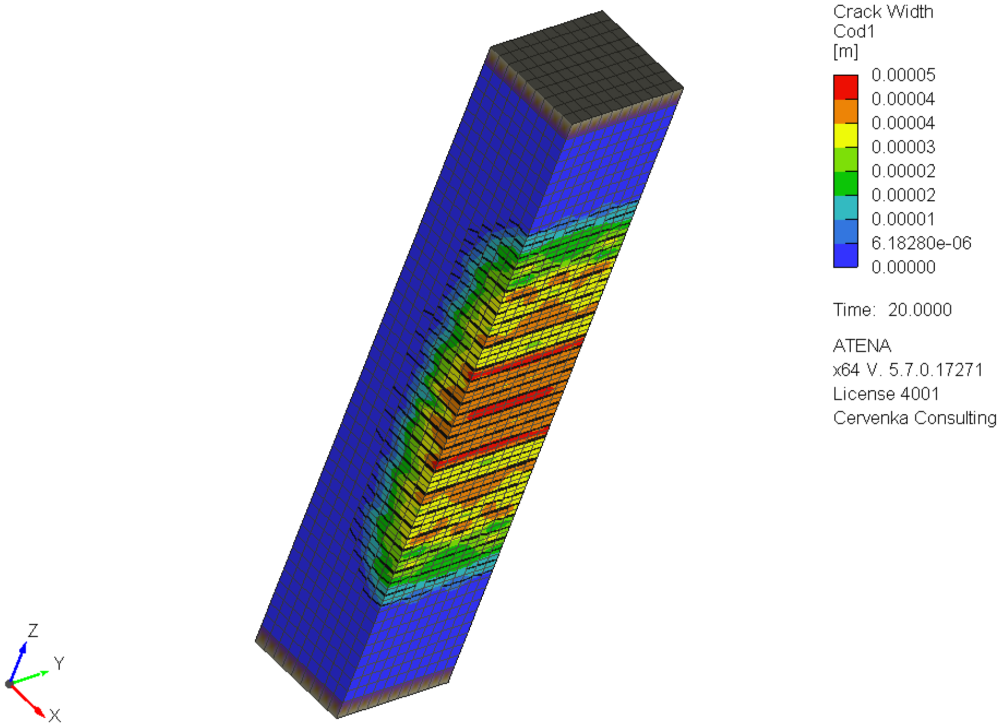

Figure 4.18: Concrete strut with artificial-induced cracks in three-point bending, maximum crack width 0.05 mm

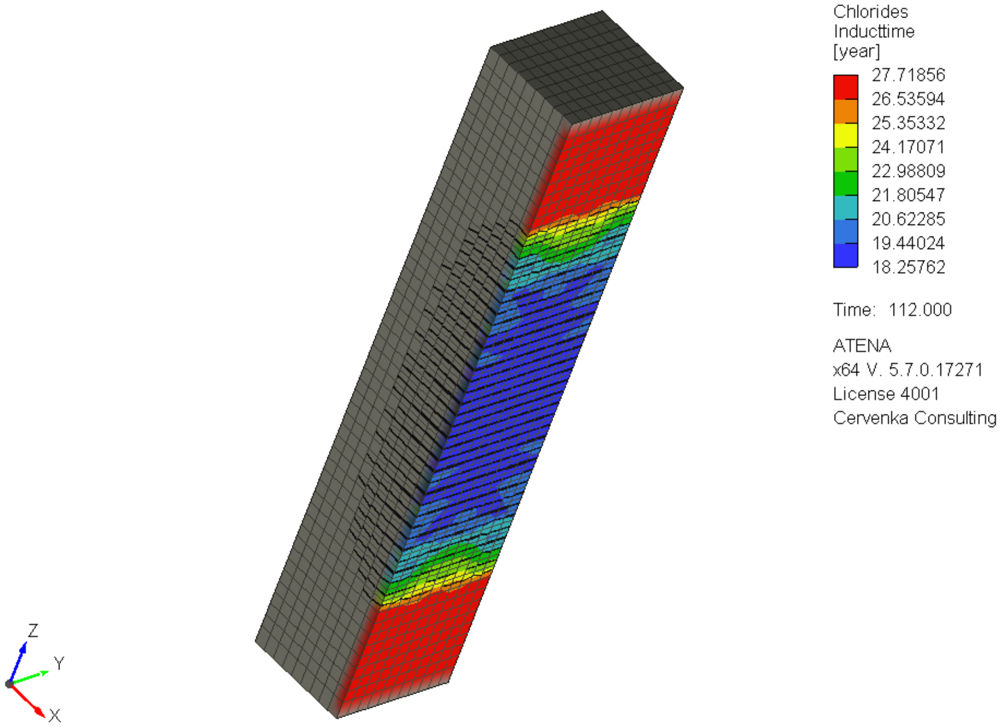

Figure 4.19: Induction time for strut with concrete cover 35 mm and maximum crack width 0.05 mm

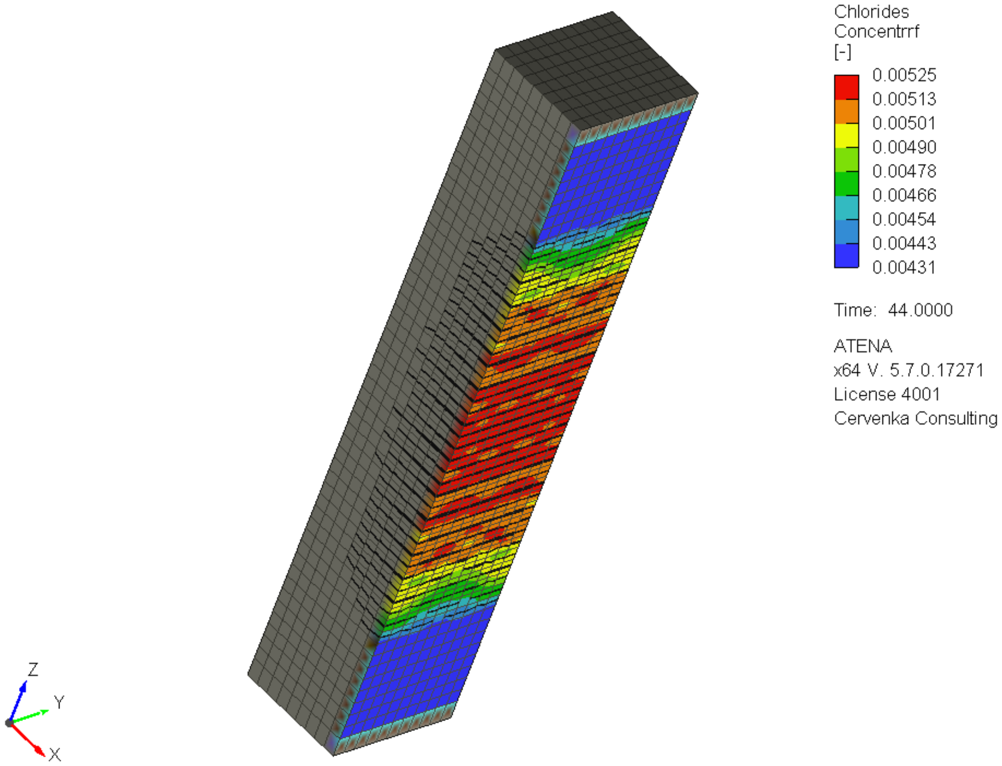

Figure 4.20: Concentration of chlorides (by mass of binder) in the place of longitudinal reinforcement after 32 years for strut with concrete cover 35 mm and maximum crack width 0.05 mm

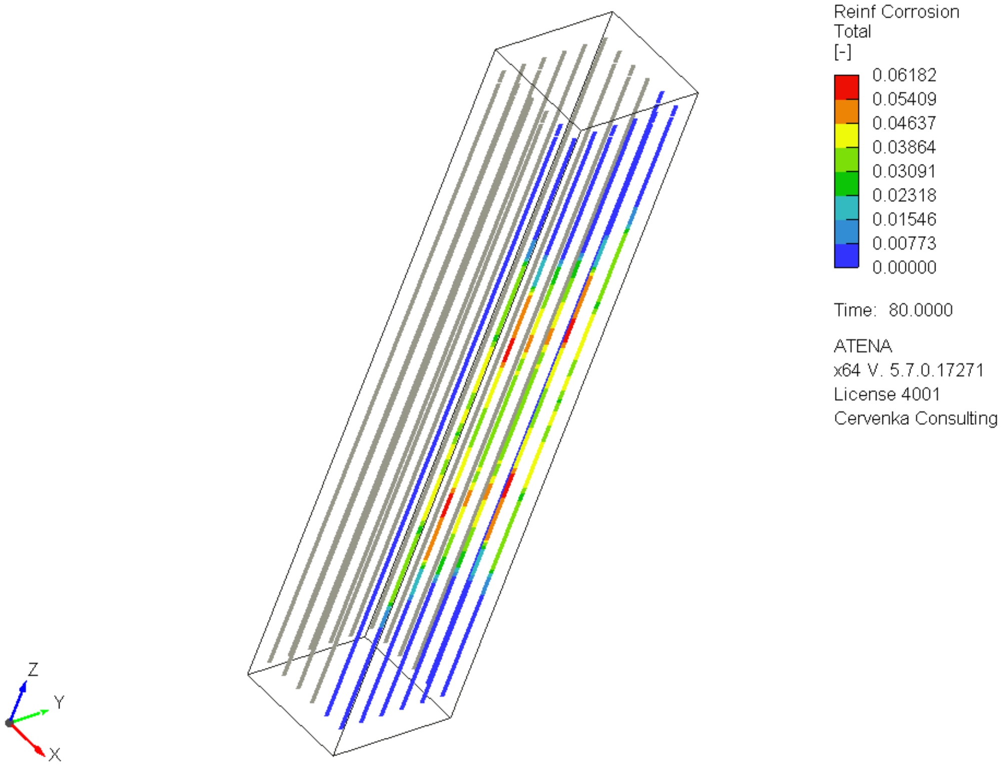

Figure 4.21: Corresponding corrosion of reinforcement after 32 years for maximum crack width 0.05 mm

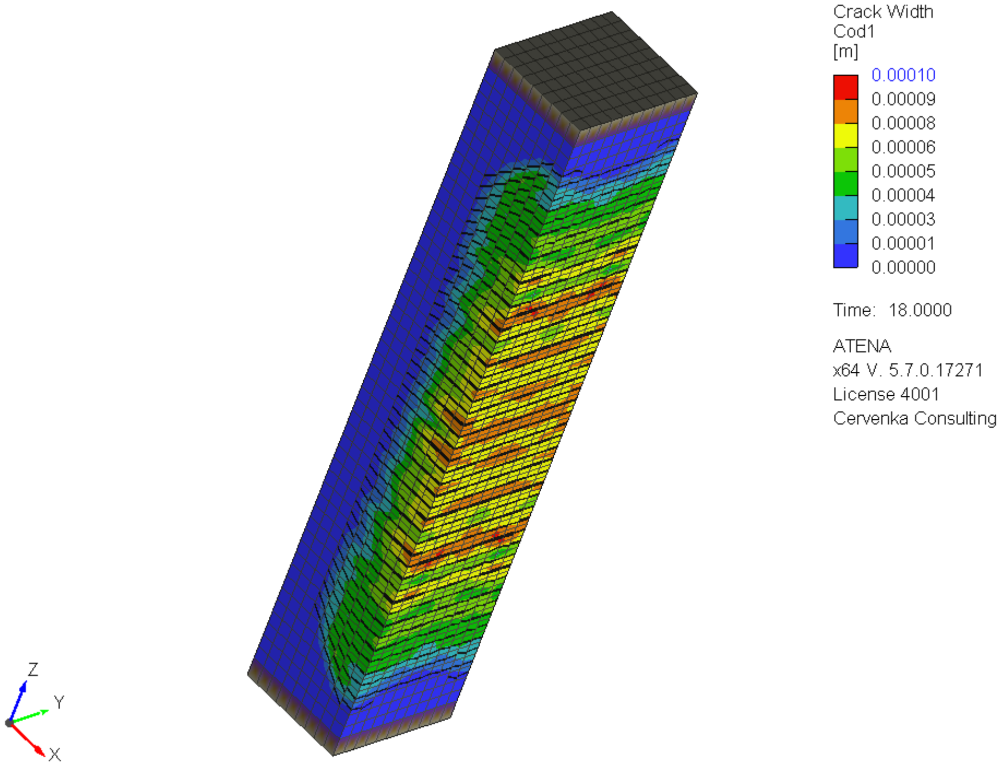

Figure 4.22: Concrete strut with artificially-induced cracks in three-point bending, maximum crack width 0.1 mm

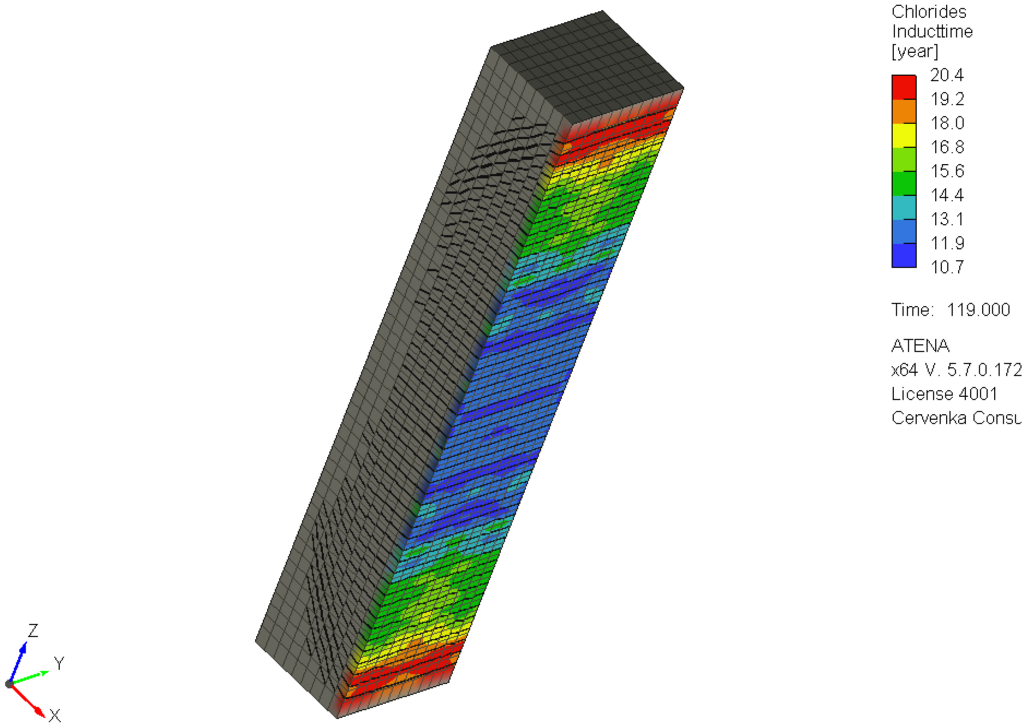

Figure 4.23: Induction time for strut with concrete cover 35 mm and maximum crack width 0.1 mm

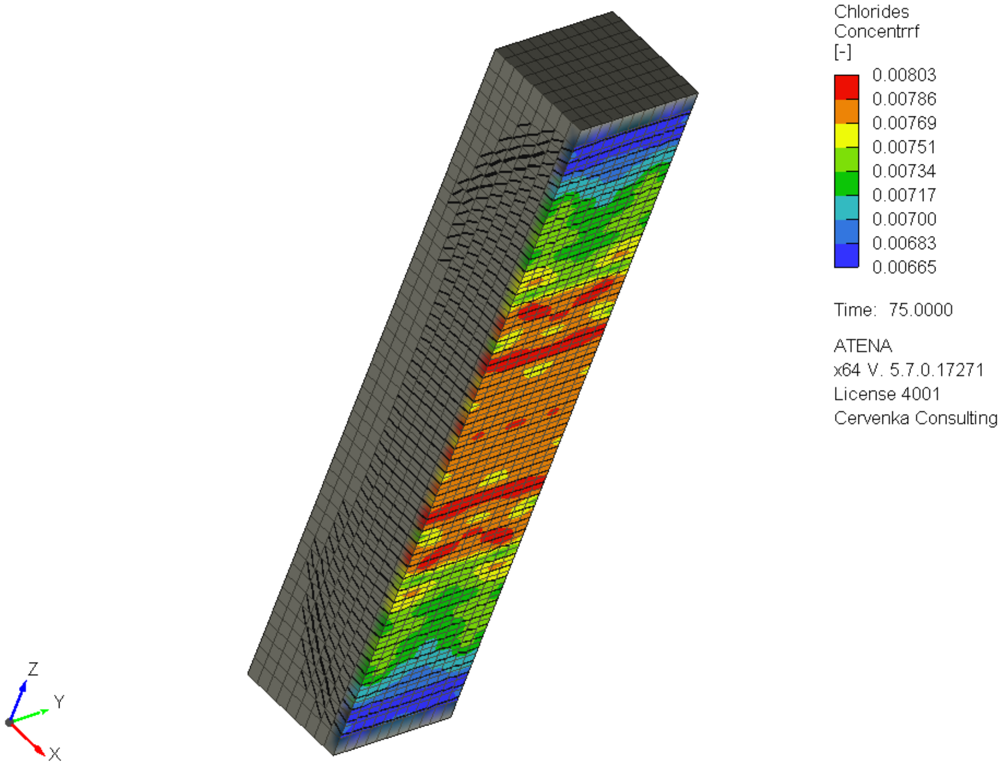

Figure 4.24: Concentration of chlorides (by mass of binder) in the place of longitudinal reinforcement after 32 years for strut with concrete cover 35 mm and maximum crack width 0.1 mm

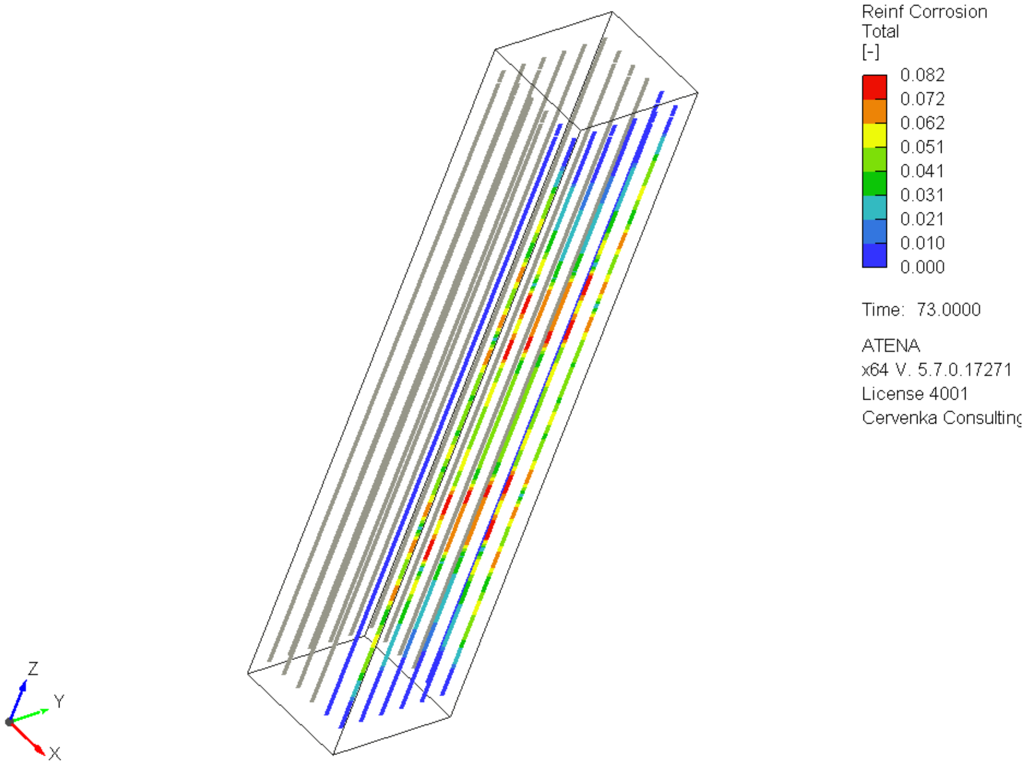

Figure 4.25: Corresponding corrosion of reinforcement after 32 years for maximum crack width 0.1 mm

4.2.3 LCC (life-cycle cost) analysis of bridge struts

This chapter demonstrates several variants of the corrosion protection or its prevention for structures attacked by chlorides. This analysis shows the suitability, the economic side and the applicability of the chemo-mechanical model. The choice of corrosion precaution influences the initial construction design or planning of the long-term investment plan in terms of economic and environmental impact.

The analysis contains four scenarios. Three variants of the construction treatments, design and the materials used to prevent the corrosion process and one variant to repair the damage caused by the corrosion of reinforcement.

- In the first variant (V1), the concrete cover thickness of the bridge struts is designed to resist chlorides during the planned lifetime of the structure (100 years). The concrete cover thickness ensures that critical concentration is not reached in the place of reinforcement. This requirement fulfills the increase of the concrete cover to 0.07 m from the original 0.035 m (new induction time 118 years).
- The second option uses stainless steel (V2). This material does not corrode in contact with chlorides.
- In the third variant (V3), the surface of concrete struts is treated with an anti-chloride coating. Such protective layer prevents chloride entering to the structure and further to the reinforcement. The protective layer (KEIM Concretal) is renewed after every 25 years, which declares the lifetime of the coating.
- Repeated repairs of the concrete cover layer after the predicted initiation period (time when corrosion of reinforcement stars) is the last variant (V4). This variant includes demolishing work of concrete cover.

The LCC analysis contains prices of material, work of concrete casting, reinforcing, formwork and scaffolding, etc. The material and work prices used in the analysis are based on data proposed by Czech Statistical Office [26]. Life-cycle costs are calculated for all bridge struts. The prices used in the analysis are summarized in the Tab. 4.3. Life-cycle cost analysis cannot ignore the impact of individual variants on efficiency, planning work and practicability. Therefore, the parameter of the suitability of the solution is also considered in the final evaluation presented in the Tab. 4.4.

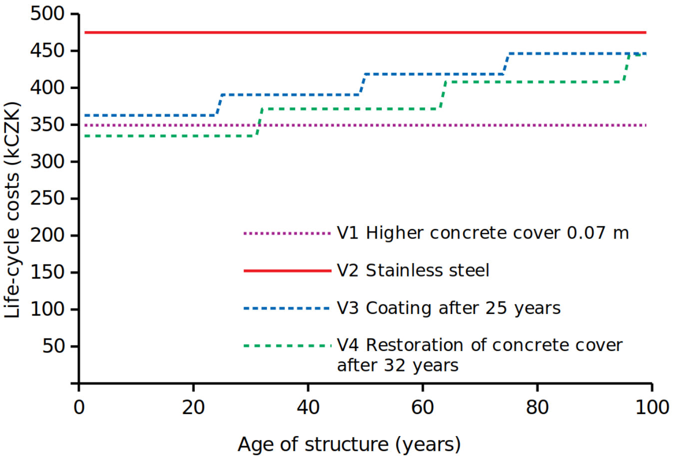

Figure 4.26: Life-cycle costs of concrete struts for different solutions

Fig. 4.26 shows the comparison of presented variants. The variant V1 of higher concrete cover is the best from the economical point of view. In this case, the total costs reaches 350 kCZK. This scenario causes higher dead-weight and dimensions that are not visually welcome. We can not neglect the negative impact of the higher concrete production (5.8 m^3, 35% more than other variants V2 and V3) and transport on the environment. The final costs of the third and fourth variant are similar. In the case of coating after 25 years (V3) it is 446 kCZK and in the case of restoration of concrete cover (V4) it is 445 kCZK. Using of stainless steel (V2) is on the last position with price of 480 kCZK, which is not a significant difference from the variant V3 and V4, but the difference between the initial costs is 112 kCZK (31%) compared with V3 (coating).

Work type and materials	Unit price	Amount	Notes (periods)
Concrete	2000 CZK/m^3	16.8 m^3	Volume 22.6 m^3 for case V1
Steel reinforcement	55 CZK/m	1120 m	
Stainless steel	175 CZK/m	1120 m	
KEIM Concretal	225 CZK/m^2	98 m^2	Period 25 years for case V3
Concrete casting	300 CZK/m^3	16.8 m^3	Volume 22.6 m^3 for case V1
Formwork set up	220 CZK/m^3	16.8 m^3	Volume 22.6 m^3 for case V1
Formwork remove	80 CZK/m^3	16.8 m^3	Volume 22.6 m^3 for case V1
Reinforcing	210 CZK/m	1120 m	
Coating	60 CZK/m^2	98 m^2	Period 25 years for case V3
Concrete demolish	300 CZK/m^3	2.52 m^3	Period 32 years for case V4

Table 4.3: Table of work and material prices

Due to the growing importance of the construction impact on the environment is crucial to reduce the amount of used materials. This mainly concerns the realisation of a higher concrete cover and restoration of concrete cover. Therefore, the suitability mark M_S, which includes the impact of produced material and waste on the environment, is assigned by a weight factor (W_S) of 5. The economic mark M_E is assigned by a weight factor (W_E) of 4. Weighted averages are calculated according to Eq. 4.1 from marks and weight factors in bracket and sorted in the Tab. 4.4.

$$\text{Weighted average} = \frac{M_E W_E + M_S W_S}{W_E + W_S} \tag{4.1}$$

Variant	Total costs	Economic mark	Mark of suitability	Weighted average	Position
V1	350 kCZK	1(4)	4(5)	2.67	**2.**
V2	480 kCZK	5(4)	1(5)	2.78	**3.**
V3	446 kCZK	4(4)	1(5)	2.33	**1.**
V4	445 kCZK	4(4)	4(5)	4	**4.**

Table 4.4: Final results and positions of the scenarios for the struts corrosion protection or prevention (weight factors in bracket)

The second position occupies the variant of higher concrete cover with the lowest costs. When analysis leaves the economic side and takes into account suitability parameter, the variant of the strut coating after each 25 years goes to the first position. This variant is recommended as the best corrosion protection for analysed struts attacked by de-icing salts. The protective layer can be applied by coating or squirting, which is simple technology. The difference in final costs between coating and high concrete cover is significant 95 kCZK (21%), difference on the initial costs is 13 kCZK (2.9%).

4.3 Nougawa bridge, Japan

Nougawa bridge was built in 1930 in a Japanese coastal area. The bridge is a three span reinforced concrete structure with the total length of 131 m without prestress. Due to high chloride presence in the air and fast corrosion, the bridge was repaired in 1959, 30 years after its erection by patching lost cover with mortar. In 2009 (79 years after the erection), two beams from the bridge were cut out and further investigated, Fig. 4.27. The concrete cover spalled almost everywhere and the reinforcements were heavily corroded.

Figure 4.27: Cut-out, validated Nougawa bridge beam [101]

The beams had stirrups with the diameter of 9.5 mm, each beam contained 8 simple longitudinal bars with a diameter of 25.4 mm covered with 47 mm of concrete. Cross section view of Nougawa bridge is shown in Fig. 4.28. The concentration of chlorides and the loss of reinforcement in the mid-spans were experimentally measured and used in the validations. Carbonation depth was found to be nearly zero everywhere.

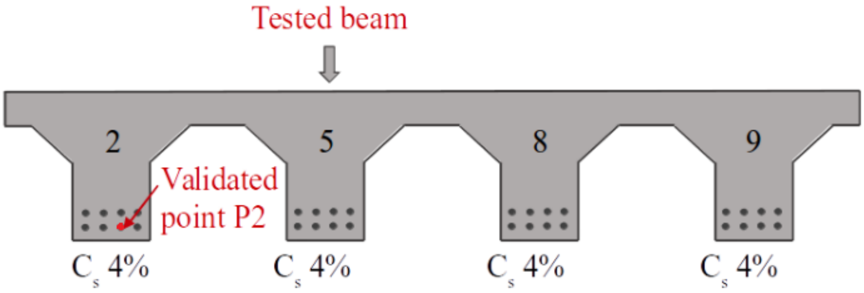

Figure 4.28: Cross section of Nougawa bridge [101]

The calculation consists of three stages, see Fig. 4.1. First, the bridge was mechanically loaded by the dead-weight and the corresponding design life load. Stresses, strains and cracks were calculated in the mechanical part. The following material parameters of the beams were adopted from experimental values; concrete compressive strength of 26 MPa and Young's modulus of 25 GPa at 79 years [101]. Cracks up to 0.39 mm emerged due to the load in the middle span.

Computational steps of the analysis and the associated loading were as follows:

1. Dead-weight of the load-bearing structure, (steps 1...10)
2. Load 135% of the dead-weight of the bridge and 150% of the traffic load of the bridges according to ULS ČSN EN 1991-2, (steps 11...27)
3. Chlorides loading for 79 years, (steps 28...105)

The second stage activated the mechano-chemical model with the prediction of the cracking time, spalling time and remaining reinforcement. The surfaces of the beams were exposed to chlorides with the parameters summarized in Tab. 4.2. According to the DuraCrete model [72,

Tab. 8.6], the decay rate factor was $m = 0.65$ for the atmospheric loading environment. The surfaces were loaded by a measured chloride concentration 4% by mass of binder which fitted the values of a tidal and atmospheric zone [72, Tab. 8.5]. The critical level for corrosion was 0.6% by binder mass [72, Tab. 8.7]. The reinforcement area loss was assumed from category C3 (coastal and industrial environment) according to table in Fig. 2.26,[99].

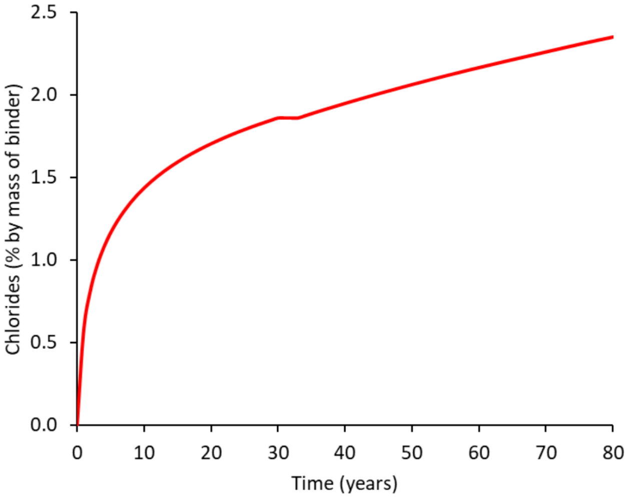

Figure 4.29: Evolution of chloride concentration at point P2

The Fig. 4.29 shows evolution of chloride concentration at the point P2 in time, including restoration of concrete cover after 30 years. The final value is used for validation presented in the Fig. 4.30a).

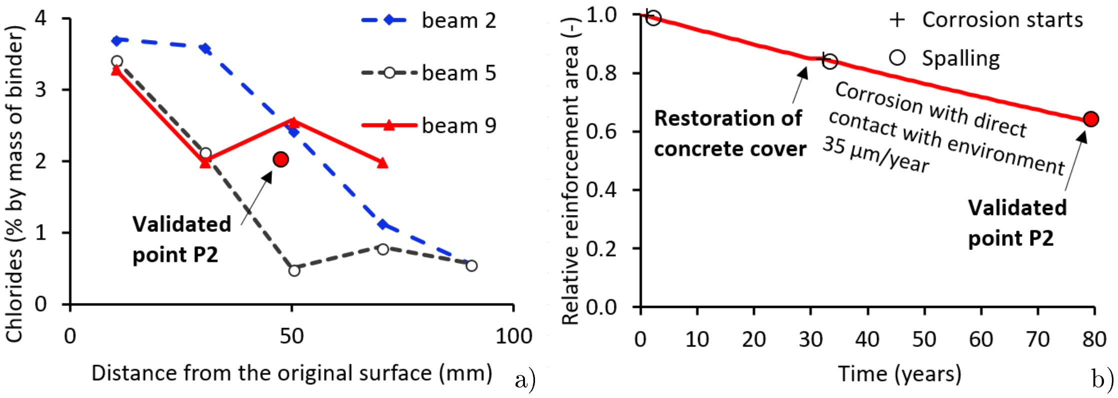

Figure 4.30: Profile of chloride concentrations for beams 2, 5, 9 in 79 years. Evolution of reinforcement loss at point P2 in 79 years a), Beam positions are marked in Fig. 4.28

Fig. 4.30a) shows the validation of the chloride concentration at point P2 at 79 years of service with measured mid-span values. Fig. 4.30b) shows the evolution of the relative reinforcement area at point P2, including the concrete cover restoration. The concrete cover spalled very soon in this case, after 2 years. The predicted relative reinforcement area of 63.6% agrees well with the measured value of 62.5%. After refilling the concrete cover, the initiation time becomes 1.88 times longer due to the concrete cover without cracks.

The Fig. 4.31 shows the crack width after 2 years of chloride loading. The initiation time in the next Fig. 4.32 shows the transport acceleration of the chloride ions in the cracks area, i.e the reduction of the initiation time.

The following Figs. 4.33, 4.36, 4.39 show the chloride concentration after 2, 30 and 79 years in the place of longitudinal reinforcement. Note that the beams were simply supported on the left side and clamped on the right side to mimic the last span of a continuous beam. Figs. 4.34, 4.37, 4.40 show the corresponding corrosion state of reinforcement after 2, 30 and 79 years. The parameter

Reinf Corrosion in figures represents relative reduction of reinforcement area (value 1 means no corrosion, while value 0 signalizes total loss). The details show the mid-spans with higher corrosion due to crack presence.

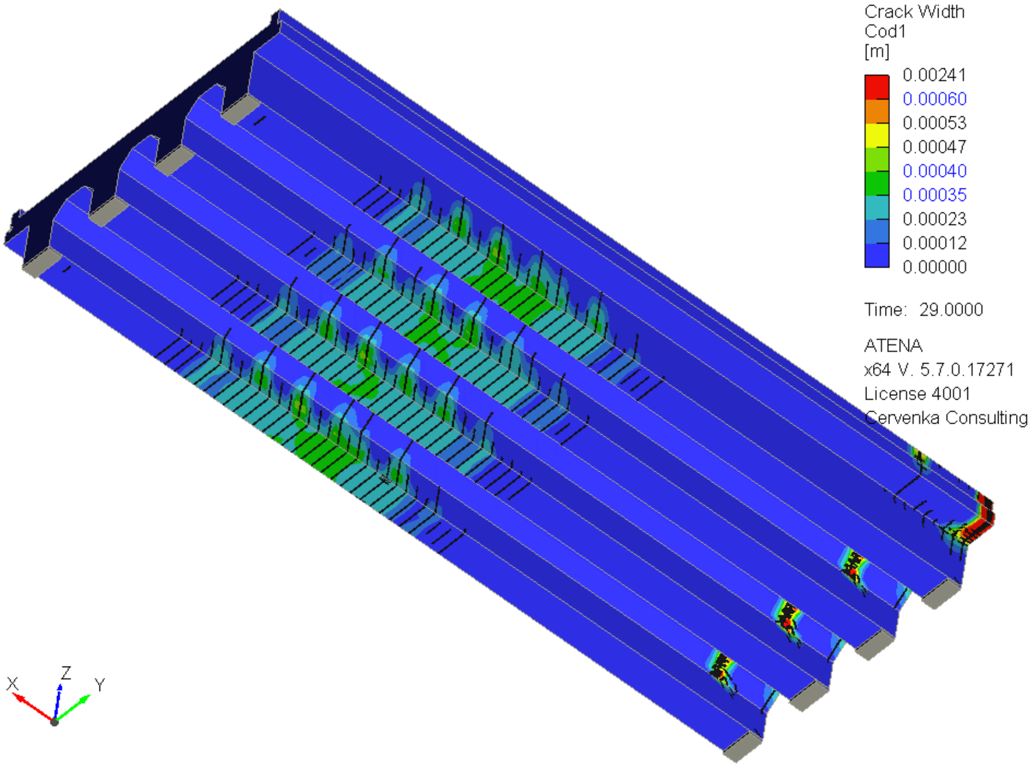

Figure 4.31: Crack width after loading by dead-weight and the traffic load

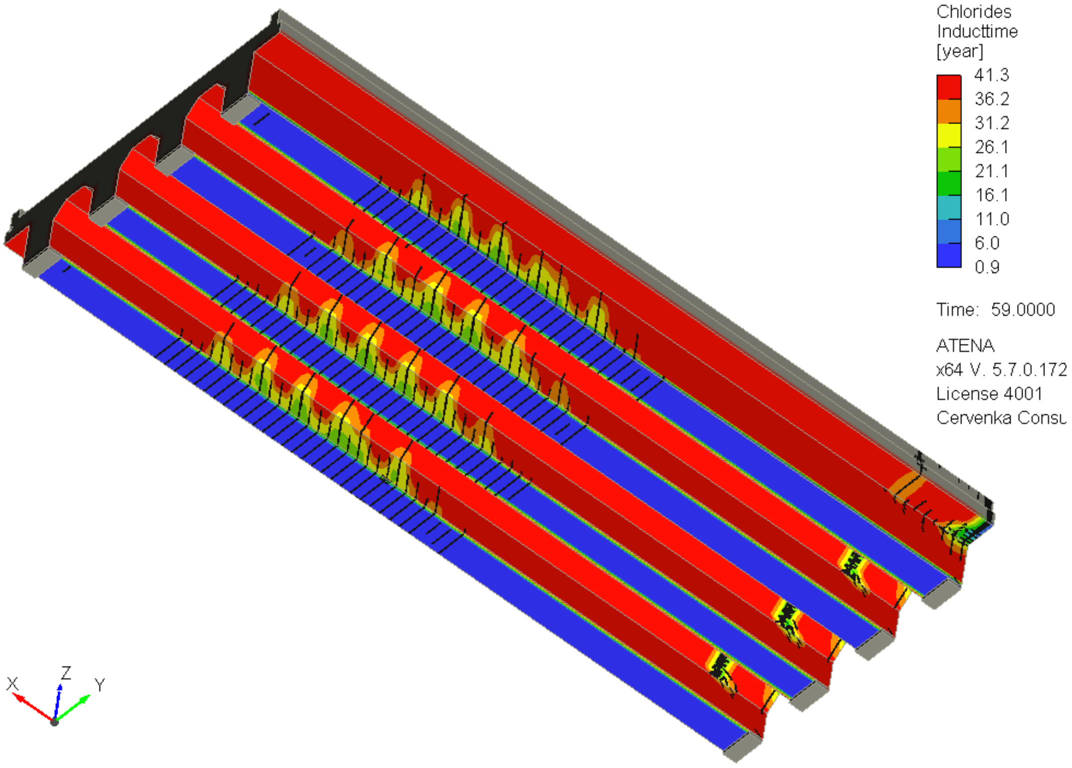

Figure 4.32: Influence of crack width on induction time

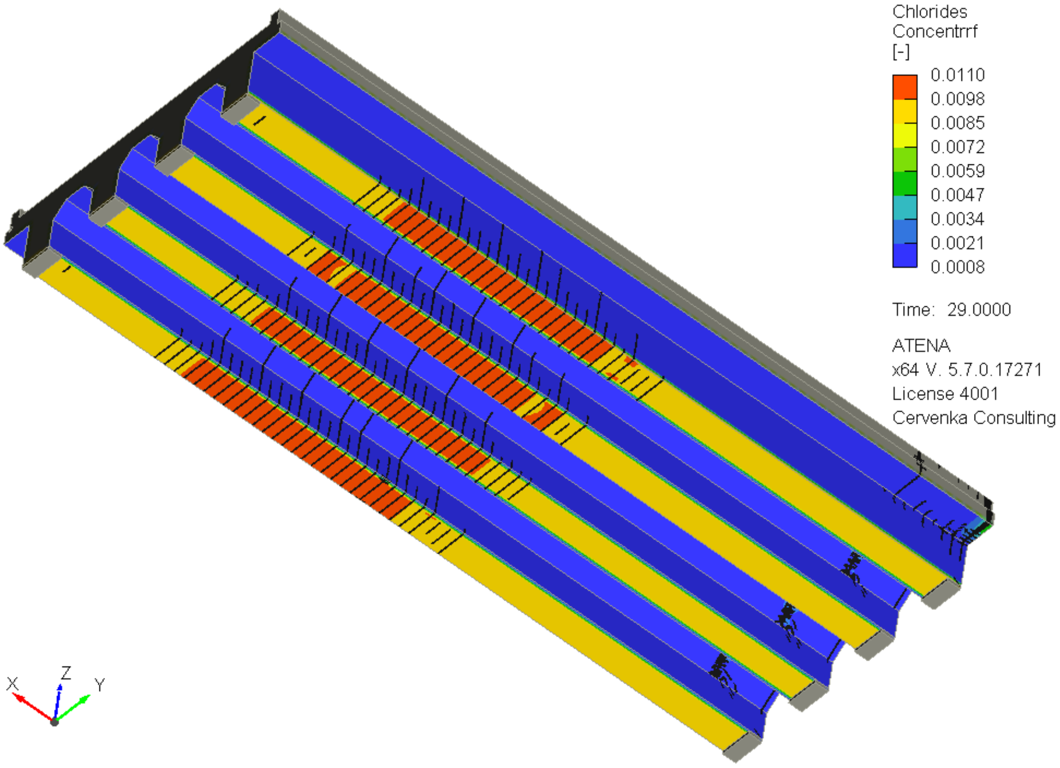

Figure 4.33: Concentration of chlorides (by mass of binder) in the place of longitudinal reinforcement after 2 years

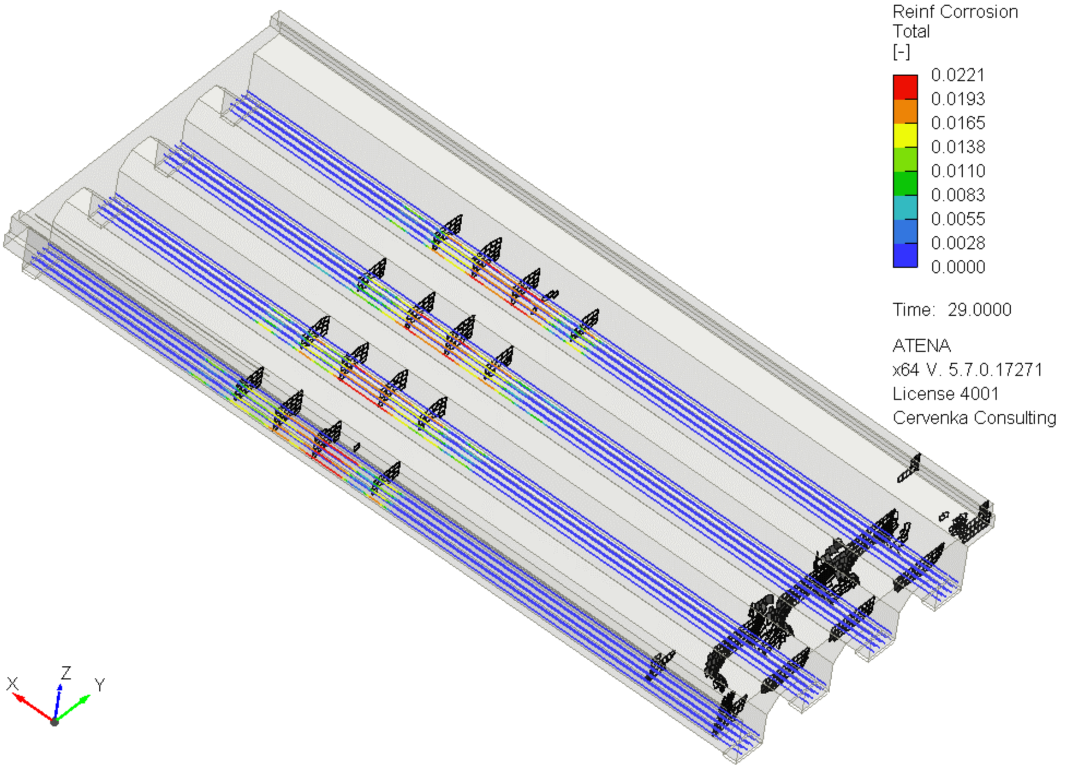

Figure 4.34: Corresponding corrosion of reinforcement after 2 years (2006)

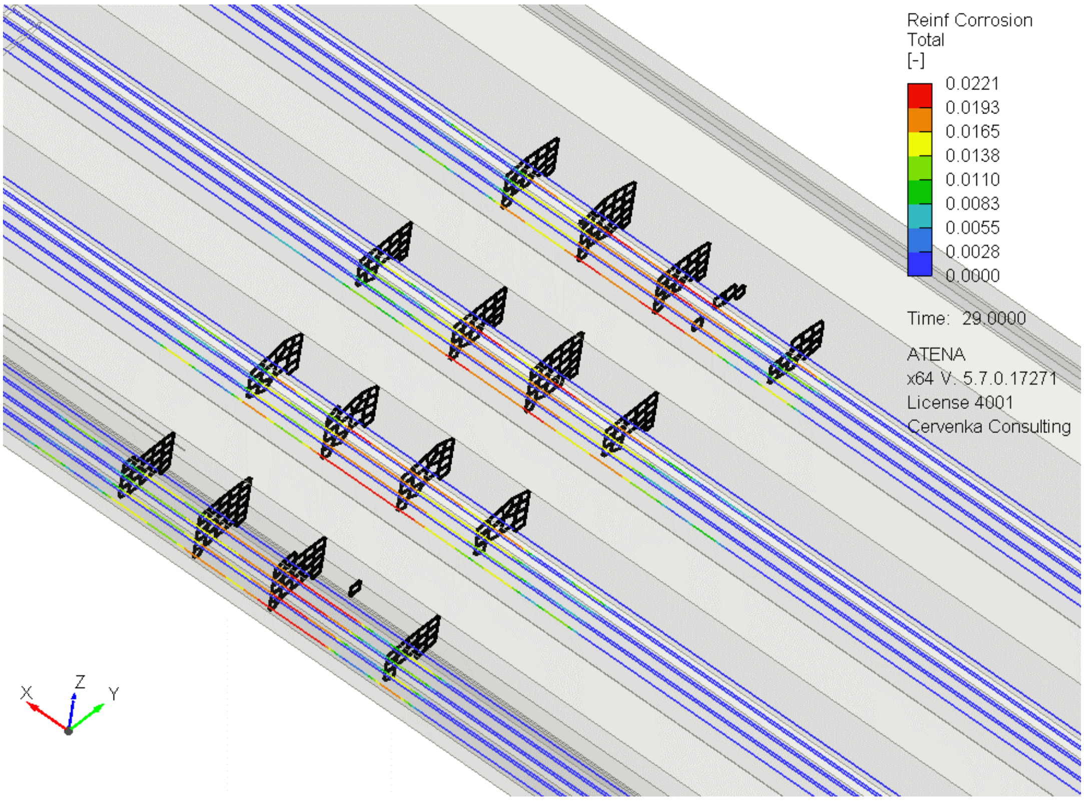

Figure 4.35: Corresponding corrosion of reinforcement after 2 years (2006), the detail shows the mid-span with higher corrosion due to crack presence

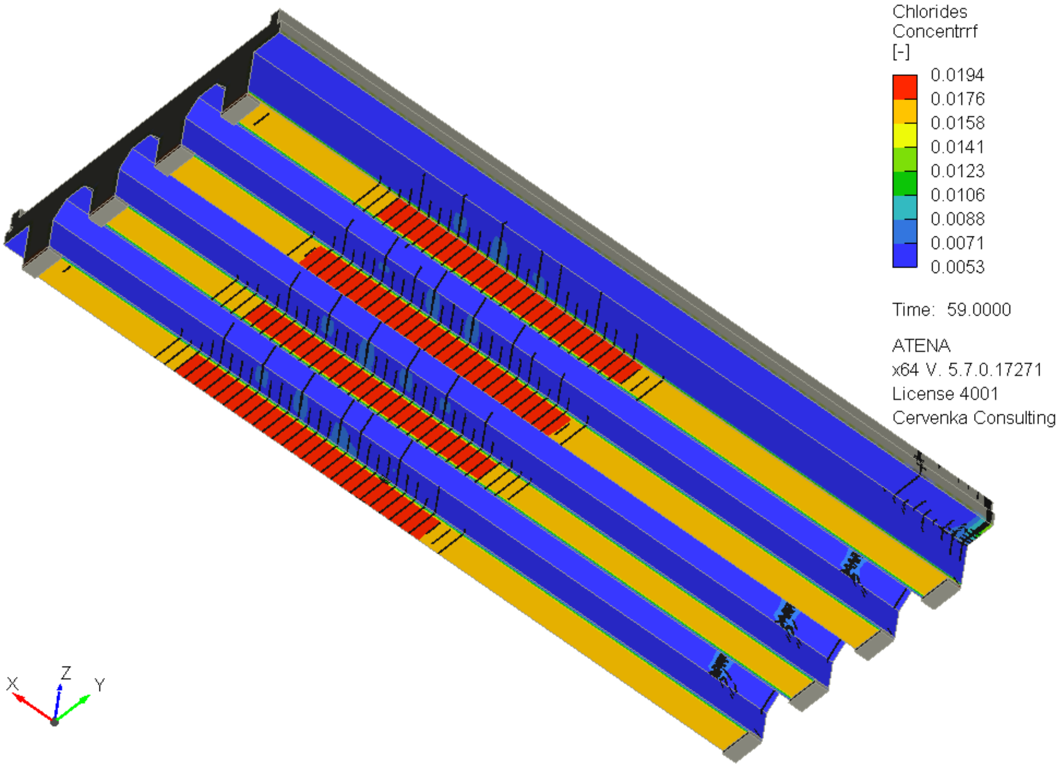

Figure 4.36: Concentration of chlorides (by mass of binder) in the place of longitudinal reinforcement after 30 years

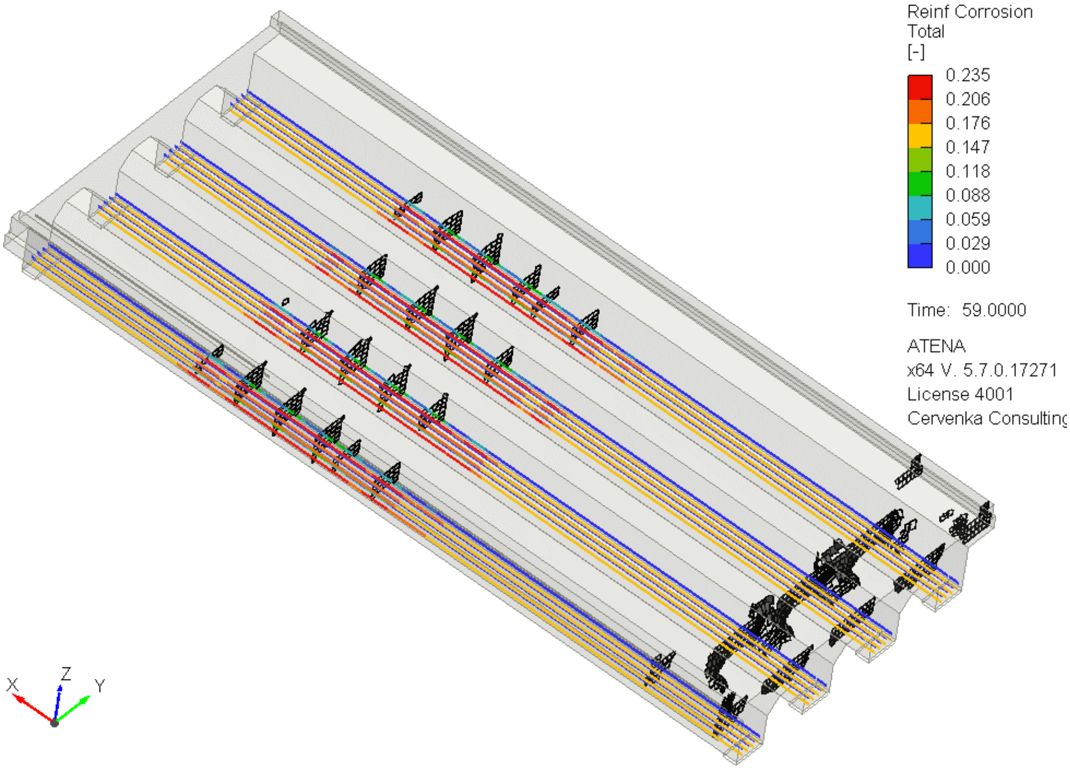

Figure 4.37: Corresponding corrosion of reinforcement after 30 years (2006)

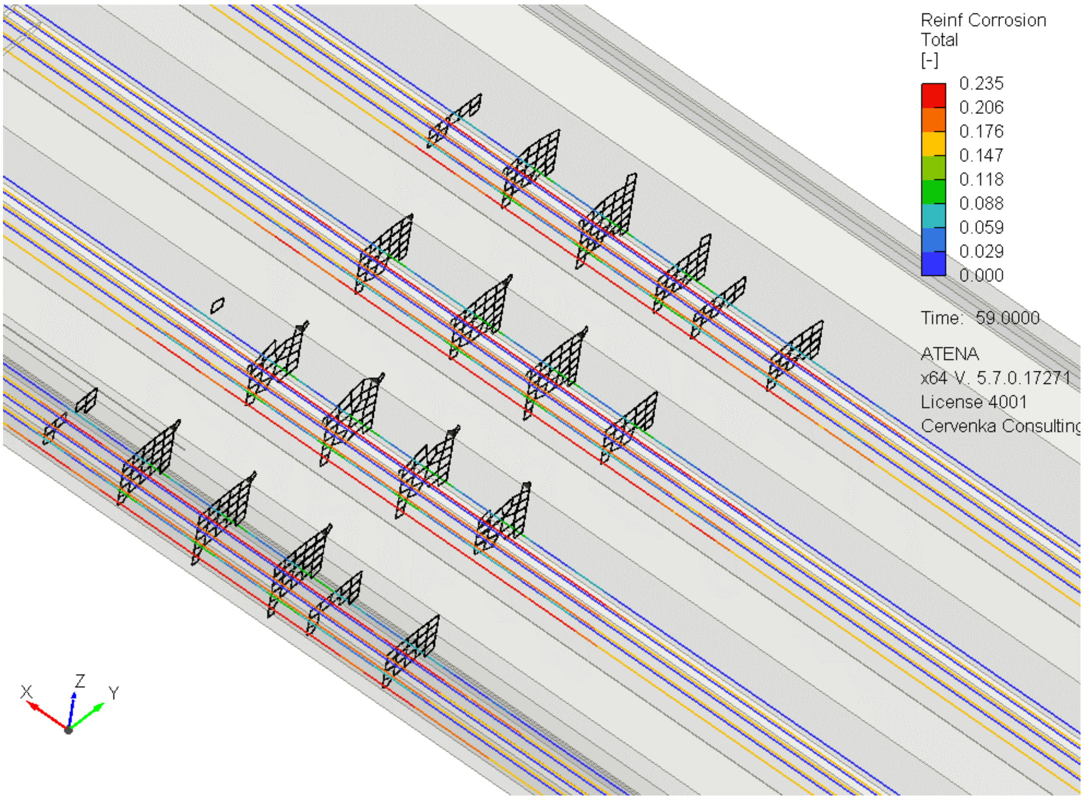

Figure 4.38: Corresponding corrosion of reinforcement after 30 years (2006), the detail shows the mid-span with higher corrosion due to crack presence

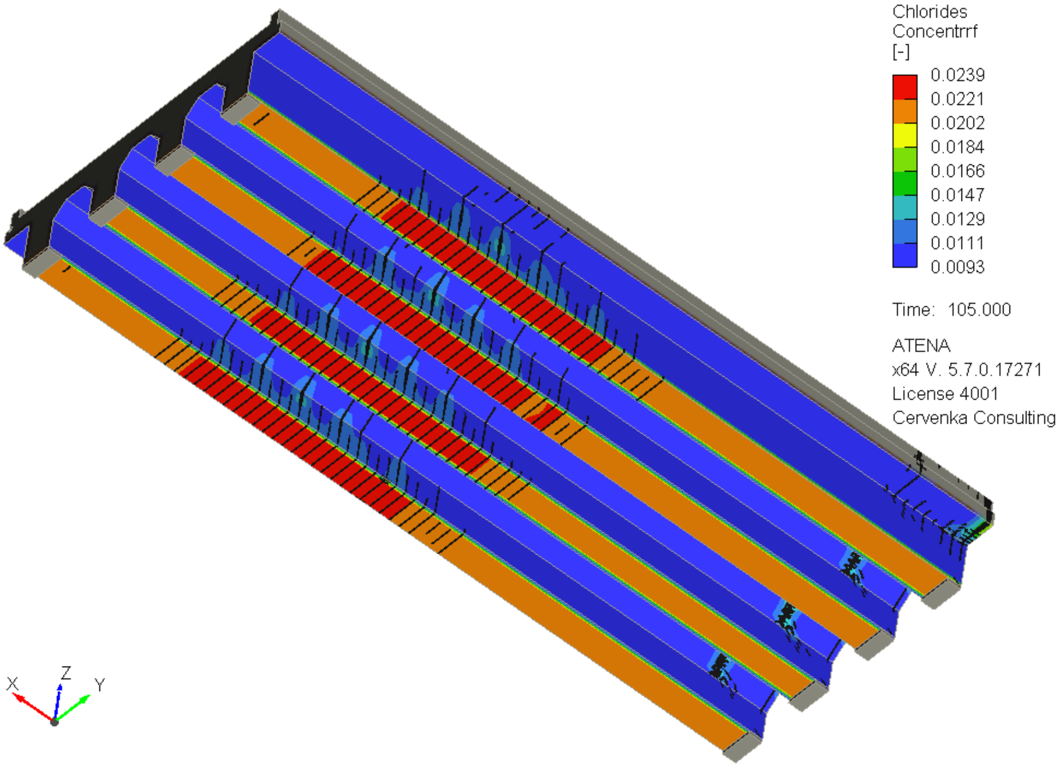

Figure 4.39: Concentration of chlorides (by mass of binder) in the place of longitudinal reinforcement after 79 years

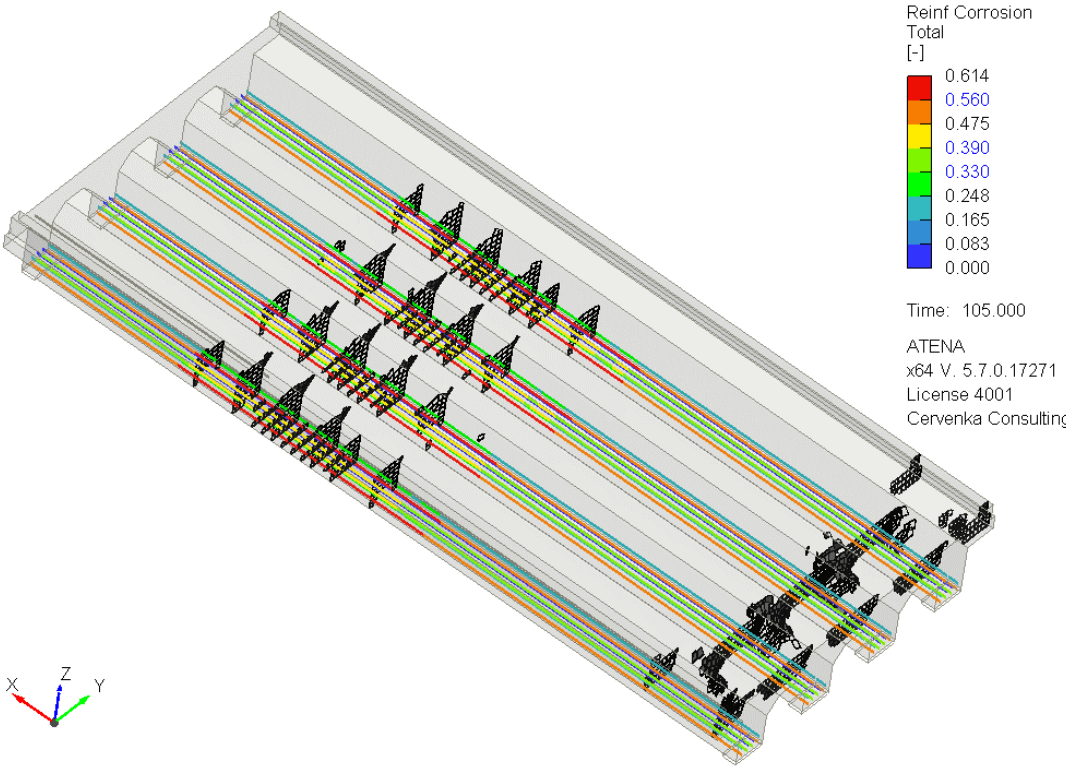

Figure 4.40: Corresponding corrosion of reinforcement after 79 years (2006)

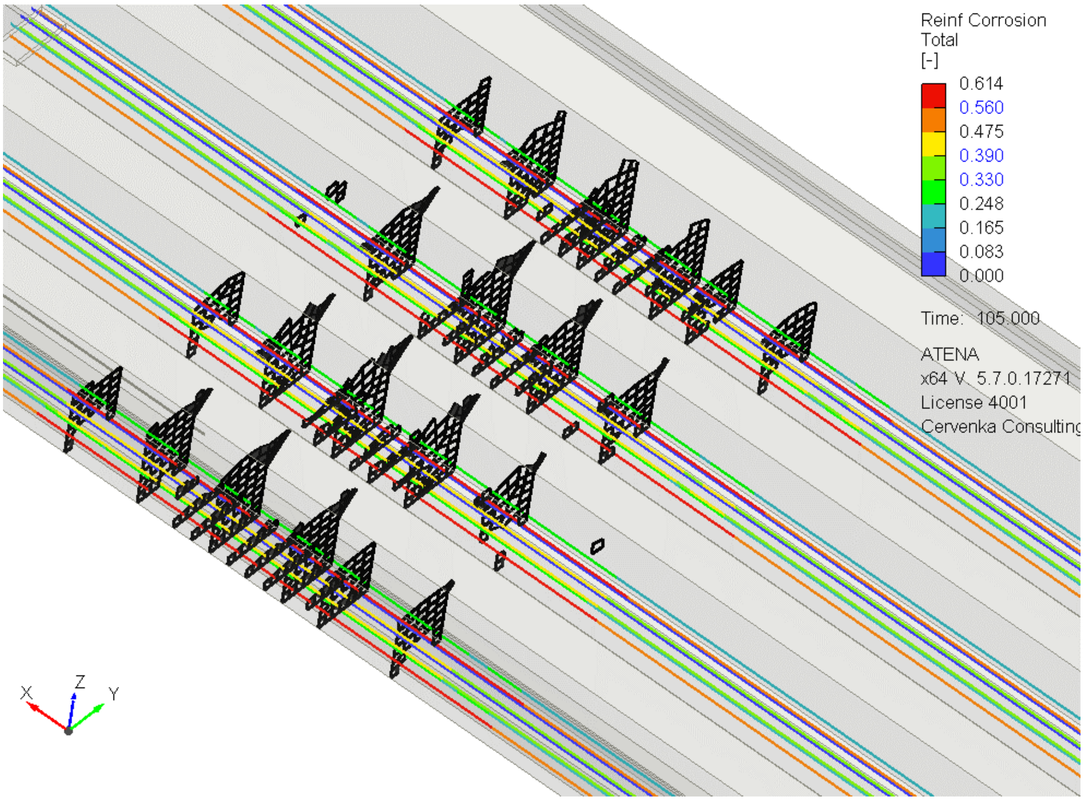

Figure 4.41: Corresponding corrosion of reinforcement after 79 years (2006), the detail shows the mid-span with higher corrosion due to crack presence

4.3.1 Ultimate limit state analysis of Nougawa bridge's beam

Ultimate limit state analysis (ULS) presents the third and the last modelling stage. The experiments determined the load bearing capacity from a cut-out beam. The four-point loading, depicted in Fig. 4.42a), recorded the mid-span deflection and applied loading forces. A high level of corrosion and complete destruction of the concrete cover caused that rebar A in Fig. 4.42b) detached from the beam. For this reason, this bar was removed in the computational model.

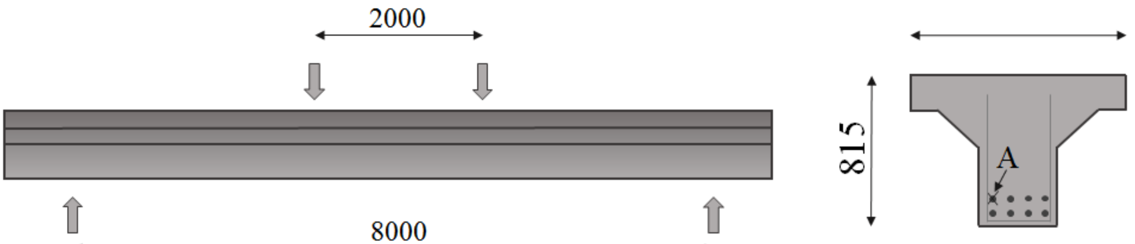

a) b)

Figure 4.42: Experimental setup a) and cross section of the beam b) [101]

The cut-out beam was modelled and loaded by the same way as the whole span, by dead-weight, design life load and chlorides, Fig. 4.43. Additional extra load increment was applied up to failure of the bridge.

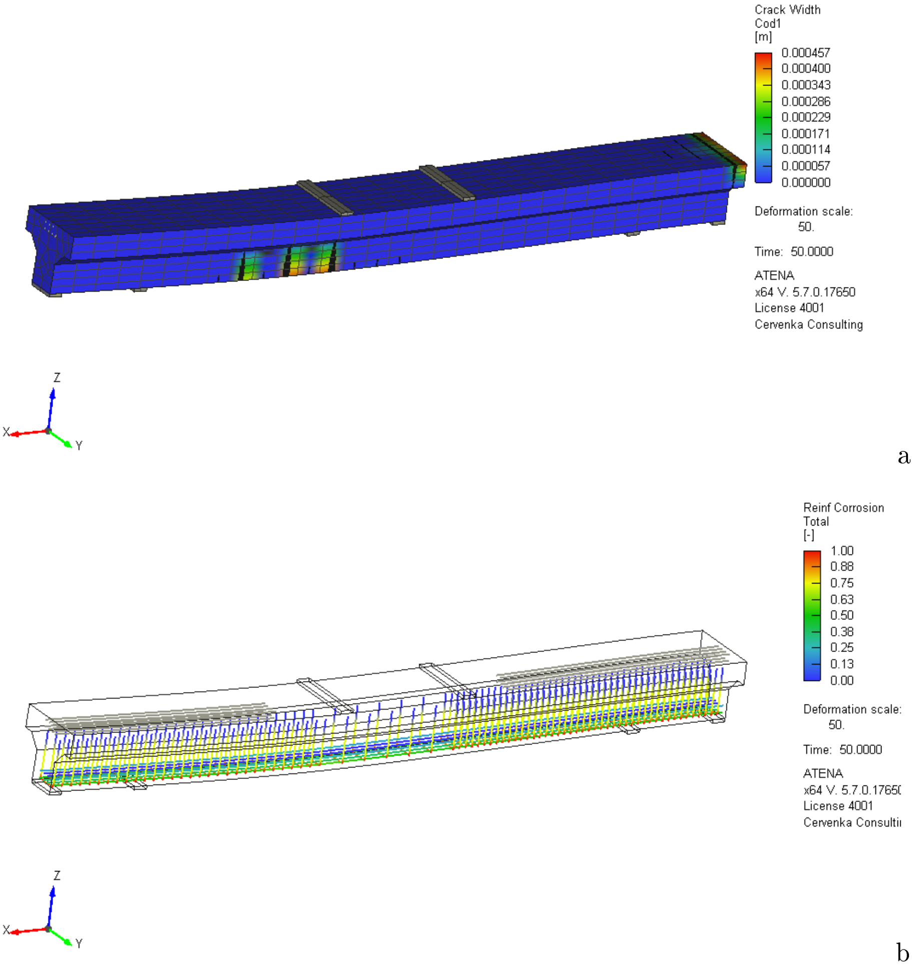

a)

b)

Figure 4.43: The cut-out beam after loading by dead-weight, design life and chlorides. Crack width a), *Reinf Corrosion* b)

Fig. 4.44 shows the mesh of the finite element model for ULS analysis. During four-point loading, tensile fracturing occurred in the middle part and it propagated as long as the beam increased deflection.

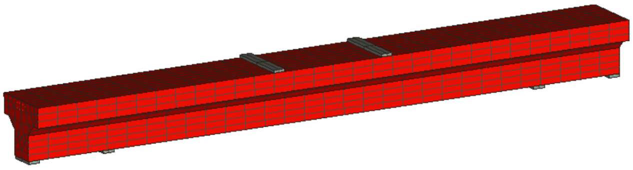

Figure 4.44: Simulated beam with two supports and load points

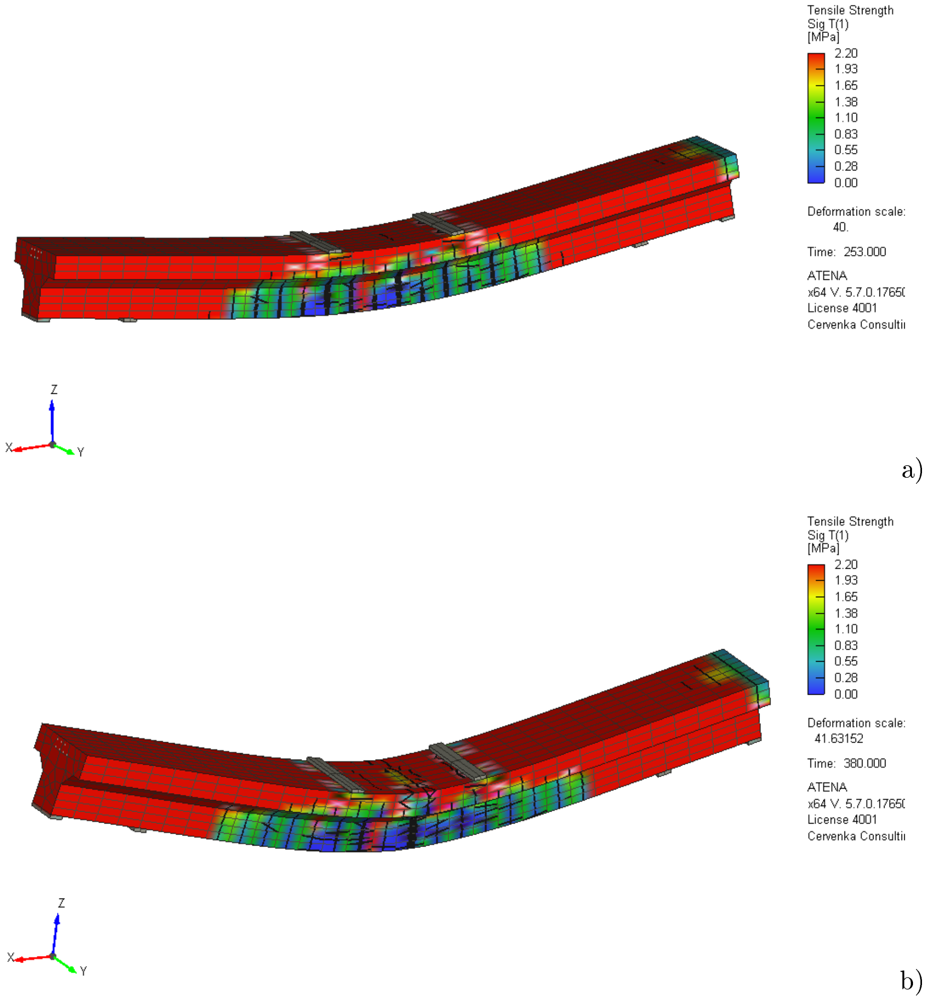

Figure 4.45: Residual tensile strength during ULS analysis. ULS analysis at 85% of the peak load a), ULS analysis at maximum deflection at 0.07 m b)

Fig. 4.46a) evaluates analytically the maximum load from a known, reduced reinforcement area. After the erection, the maximum load corresponded to 340.6 kN and decreased to 193.9 kN at 79 years. Fig. 4.46b) shows the ULS simulation at 79 years. The maximum force of 200.9 kN (depicted by blue point in Fig. 4.46a)) from the simulation (deflection of 0.04 m) drops down to 136 kN due to the rupture of the lower reinforcement layer. No shear failure occurred in the 3D simulation although the stirrups area loss was 55% near the lower surface. ULS simulation ends by the rupture of the remaining reinforcement.

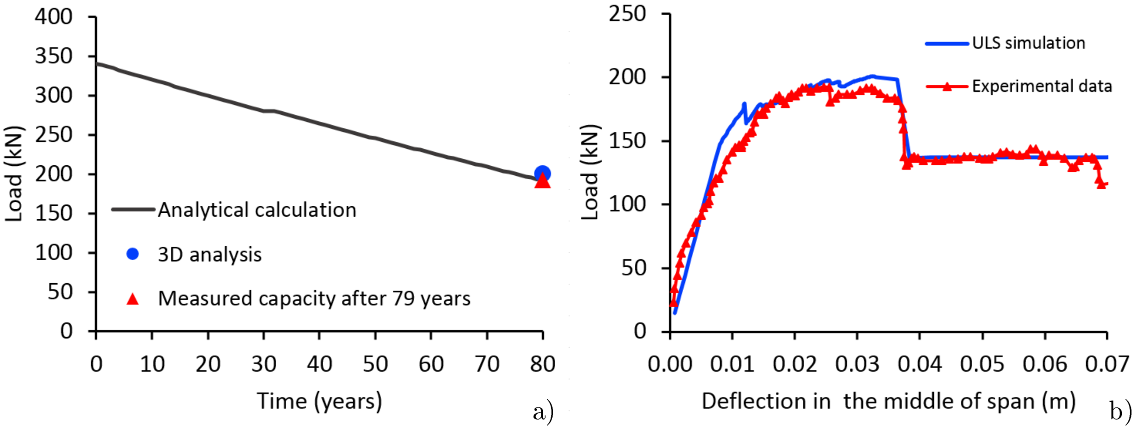

Figure 4.46: Analytical calculation of load bearing capacity up to 79 years a), evolution of load bearing capacity after 79 years compared with experimental data [101]b)

4.3.2 LCC bridge analysis

The analysis of Nougawa bridges' LCC uses the same scenarios of the corrosion protection or prevention as in Section 4.2.3. The total costs are calculated by the same way and from the same work and material prices summarized in Tab. 4.3.

- In the first variant (V1), the concrete cover thickness of the bridge struts is designed to resist chlorides during the planned lifetime of the structure (100 years). The concrete cover thickness ensures that critical concentration when corrosion starts is not reached in the place of reinforcement. This requirement fulfills the increase of the concrete cover to 0.12 m from the original 0.047 m (new induction time is 108 years).
- The second option uses stainless steel (V2). This material does not corrode in contact with chlorides.
- In the third variant (V3), the surface of concrete struts is equipped with a anti-chloride coating, this protective layer prevents chloride entering to the structure and further to the reinforcement. The protective layer (KEIM Concretal) is renewed after each 15 years, period is adapted due to high corrosion aggression of coastal zone.
- Repeated repairs of the concrete cover layer after 5 years is the last variant (V4). This scenario includes demolish work of concrete cover.

The analysis of life-cycle costs contains prices of material, work of concrete casting, reinforcing, formwork and scaffolding, etc.

Fig. 4.47 shows comparison of presented variants. The variant V1 of higher concrete cover is the best from the economic point of view. In this case the total costs reach the price of 2026 kCZK. This scenario also brings an increase of the load on the structure and massive members. We can not neglect the negative impact of the higher concrete production (30 m^3, 10.3% more than other variants V2 and V3) on environment caused by higher concrete production and transport. The third variant of coating after 15 years with total price of 2167 kCZK, following the second variant of stainless steel with final costs 2375 kCZK. On the last position is case V4 of restoration of concrete cover, price reaches 3769 kCZK. According to the modelled prediction, the concrete cover without cracks from the static load of the bridge, spalled after approximately 4 years. Repeated repairs are planned with period of 5 years and despite are the most financially demanding. Replacement of the concrete cover at the bottom surface of the entire structure means an increase in concrete production by 140 m^3 (50% more than origin volume).

LCC analysis cannot ignore the impact of individual variants on the environment, efficiency, planning work and practicability. As in the previous LCC analysis of bridge struts, the suitability mark M_S, which includes the impact of produced material and waste on the environment, is assigned by a weight factor (W_S) of 5. The economic mark M_E is assigned by a weight factor

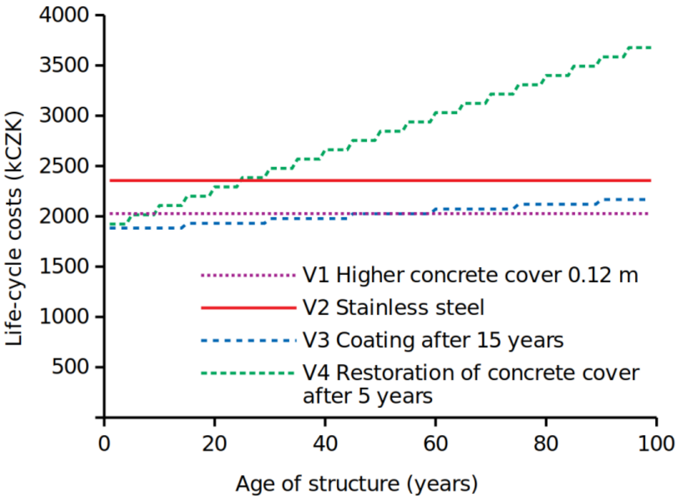

Figure 4.47: Life-cycle costs of Nougawa bridge for different solutions

Variant	Total costs	Economic mark	Mark of suitability	Weighted average	Position
V1	2026 kCZK	1.5(4)	4(5)	2.89	**3.**
V2	2375 kCZK	2.5(4)	1(5)	1.67	**1.**
V3	2167 kCZK	2(4)	2(5)	2	**2.**
V4	3769 kCZK	5(4)	5(5)	5	**4.**

Table 4.5: Final results and positions of the scenarios for the bridge corrosion protection or prevention (weight factors in bracket)

(W_E) of 4. Weighted averages are calculated according to Eq. 4.1 from marks and weight factors in bracket and sorted in the Tab. 4.5.

When analysis leaves the economic side where the variant of higher concrete cover is the best and takes into account suitability parameter, the variant of stainless steel reinforcement is in the first position. This variant is recommended as the best corrosion protection for analysed bridge in coastal area attacked by chlorides. The difference in the total costs between stainless steel reinforcement and coating after 15 years is significant 207 kCZK (8.7%), but this variant solves corrosion problem for the whole life time and next repairs are unneeded.

4.4 Analysis of a reinforced concrete bridge

The present model can be used for a wide range of structures from civil engineering. This is documented on an assessment of a reinforced concrete bridge in Örnsköldsvik, Swedish [44]. It is beyond the scope of this work to present detailed results from this analysis and hence, only the most important global results and results related to the presented durability analysis of the bridge are given.

The bridge was erected in 1955. The structure is depicted in Fig. 4.48. The bridge consists of two arches, having spans 12 + 12 m.

The analysis of the bridge consists of three stages. The first analysis contains loading of the numerical model by dead-weight and traffic load.

The second part is devoted for durability study (loading by chlorides and carbonation). The last part presents ULS analysis, loading of the bridge up to failure. Applied steps of the analysis and the associated loads were as follows:

1. Dead-weight, load 135% of the top layers weight of the bridge and 150% of the traffic load of the bridges according to ULS ČSN EN 1991-2, (steps 1...10)
2. Chlorides loading for 150 years, (steps 11...161)

Figure 4.48: View of the bridge [44]

3. Loading by predescribed displacement in the mid-span up to failure of the bridge, (steps 161...400)

Summary of the boundary conditions and loads is shown in Fig. 4.49. The surfaces, loaded by chlorides, are signed by red lines and carbonation by yellow color.

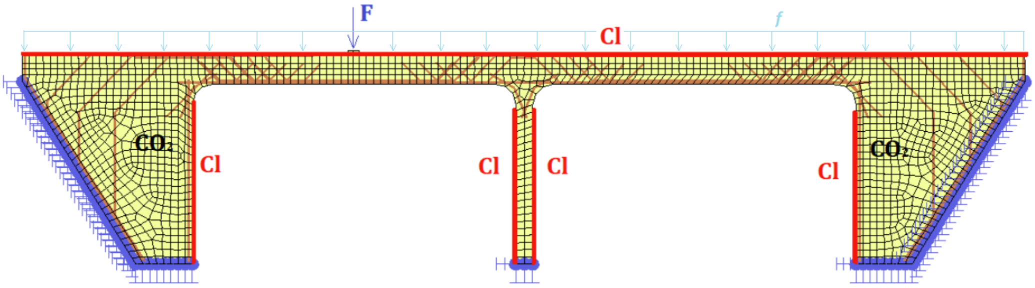

Figure 4.49: Boundary conditions of model with force load F for ULS analysis

Crack development at the 11^{th} step at bridge with two monitored points P1 and P2 is depicted in Fig. 4.50. The crack width at P1 is approximately 0.1 mm.

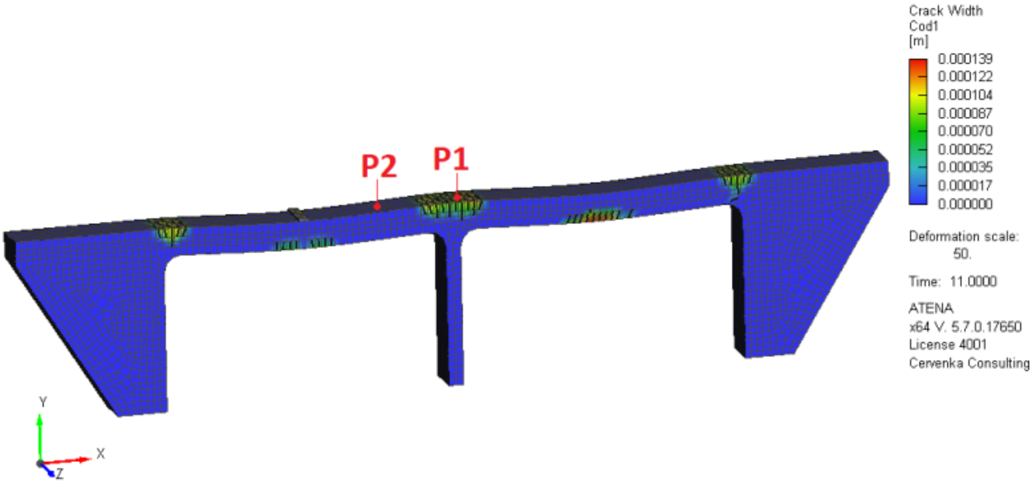

Figure 4.50: Crack development at the 11^{th} step with two monitored points P1 and P2, before loading by chlorides and carbonation

According to bridge documentation, the concrete was classified as C40/45. An estimated composition yields CEM 42.5 350 kg/m^3 and water content 175 kg/m^3. Concrete bridge was loaded on its surface by carbonation and chlorides as described below. This analysis restarted from the step 11, (i.e. from the level of design load) and carbonation and chlorides load was applied for another 150 years simultaneously. The chlorides and carbonation loads uses the parameters presented in Tab. 4.6. Progressive period uses the following cracking parameters of concrete cover $a_1 = 7.44 \cdot 10^{-5}$m, $a_2 = 7.3 \cdot 10^{-6}$ m, $a_3 = -1.74 \cdot 10^{-5}$ m/MPa and $w_d = 0.001$ m.

Carbonation parameters	Values	Chloride parameters	Values
C	350 kg/m^3	D_{ref}	6.67e-8 m^2/day [Fig. 3.8]
W	175 kg/m^3	m_{coeff}	0.37 [72]
RH	0.6 3.19	C_s	7.76% by mass of binder [72]
CO_2	0.00036 [78]	Cl_{crit}	0.06% by mass of binder [72]
$f_{t,ch}$	4 MPa	$f_{t,ch}$	4 MPa
R_{corr}	1 [37]	R_{corr}	3 [37]
C_{loss}	30 μm/year	C_{loss}	30 μm/year, category C3 [99]

Table 4.6: Parameters used in durability part

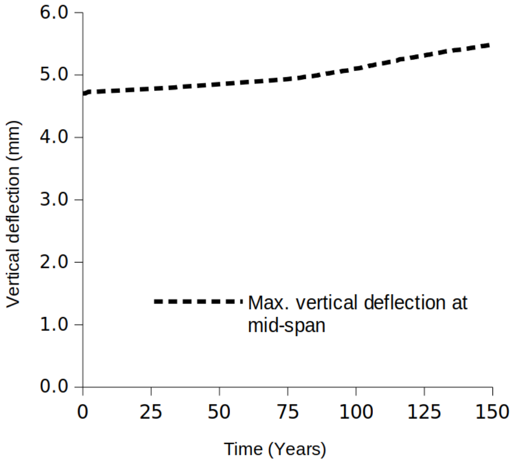

Figure 4.51: Maximum deflection of the bridge due to reinforcement corrosion

Fig. 4.51 shows maximum vertical displacement of the bridge deflection vs. age of the structure, monitored at mid-span of the left arch. Note that the increase of the deflection is due to reinforcement corrosion only as creep is neglected in computation and the force load is kept constant.

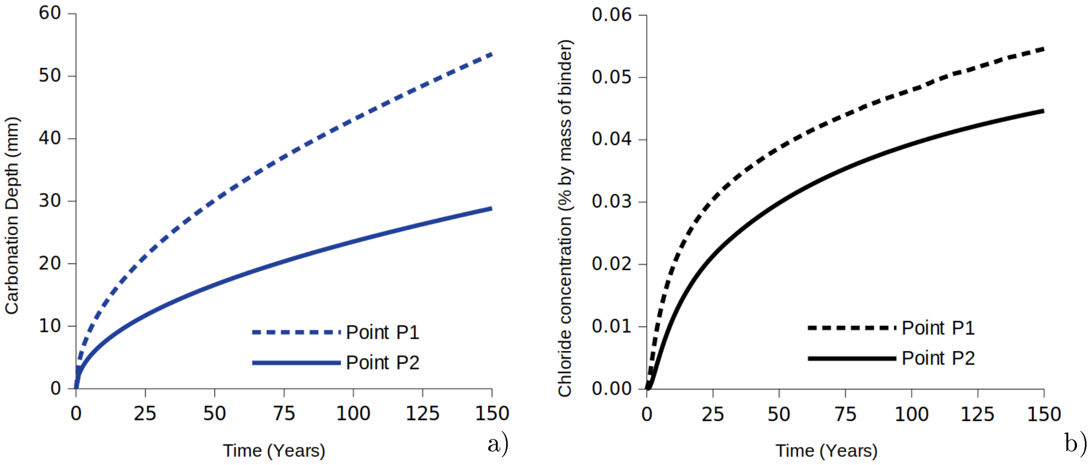

Figure 4.52: Characteristic carbonation depth a) and chloride concentration b) at 40 mm from exposed surface with the influence of cracks

Fig. 4.52a) shows that carbonation depth is 29 mm for 150 years on uncracked concrete (P2) and 54 mm at the place of crack (P1). The carbonation depth in the place of longitudinal reinforcement for the modelled structure after 150 years shows the Fig. 4.54. Fig. 4.52b) shows that chloride concentration is 4.5% on uncracked concrete (P2) after 150 years and 5.5% at the place of crack (P1). chloride concentration in the place of longitudinal reinforcement at the whole structure after 150 years shows Fig. 4.55.

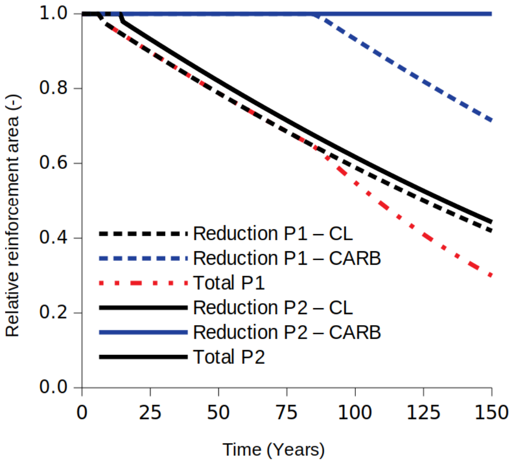

Figure 4.53: Computed reduction coefficient for a reinforcement, concrete cover 40 mm with the influence of cracks

Induction period for chlorides is much shorter, for the top layer approximately 7 years with uncracked concrete cover 40 mm and 2.2 years at the crack area. Induction time 126 years on vertical surfaces is caused by higher concrete cover 120 mm, shown in Fig. 4.56. Carbonation causes corrosion of reinforcement only on the top layer during modelled 150 years (after 82 years), see Fig. 4.57.

As far as steel corrosion is concerned, Fig. 4.53 depicts calculated reduction coefficient at points P1 and P2 for a reinforcement with concrete cover 40 mm. Reduction coefficient 1 means no corrosion, while value 0 signalizes total loss. For the first 6 years, the reinforcement does not corrode at all. Corrosion due to chlorides starts after 6 years at point P1 and after 15 years at point P2. Corrosion due to carbonation begins after 85 years at point P1 only. Carbonation depth does not reach the place of reinforcement at point P2 during modelled 150 years.

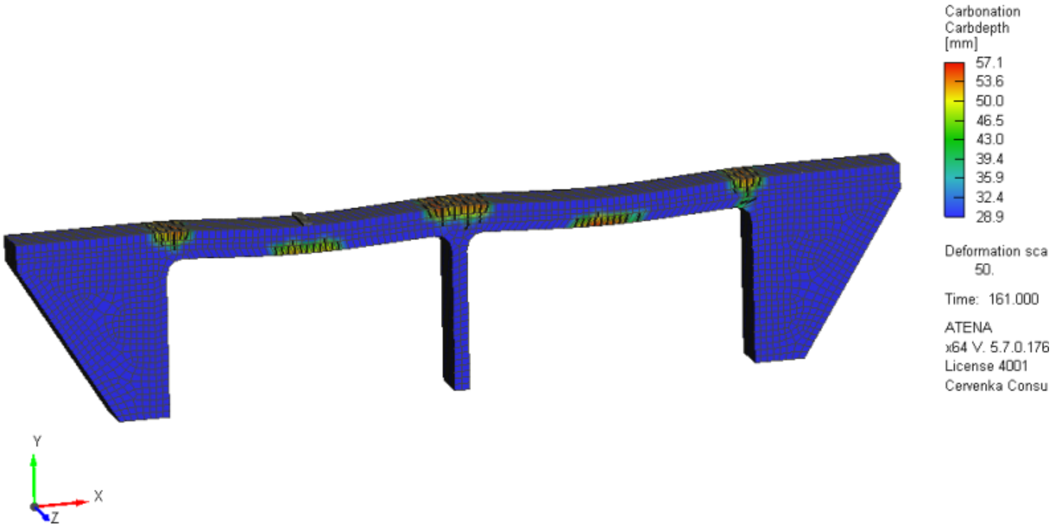

Figure 4.54: Carbonation depth in the place of longitudinal reinforcement after 150 years

At the age of 75 years about 30% of the reinforcement has corroded at point P1 and at 150 years there is only about 30% of the original reinforcement. Reinforcement at point P2 is reduced on approximately 45% due to chlorides. The visible spalling of concrete cover on the structure will occur after 16 years in the area of point P2 and after 9 years in the area of point P1. As expected, the effect of chlorides is much more devastating than that of carbonation. This is also documented by Fig. 4.58, 4.59, which show total relative reduction factor of reinforcement (sum of chlorides and carbonation) for the reinforcement at age of 75 and 150 years and reduction caused by carbonation at age 150 years is shown in Fig. 4.60.

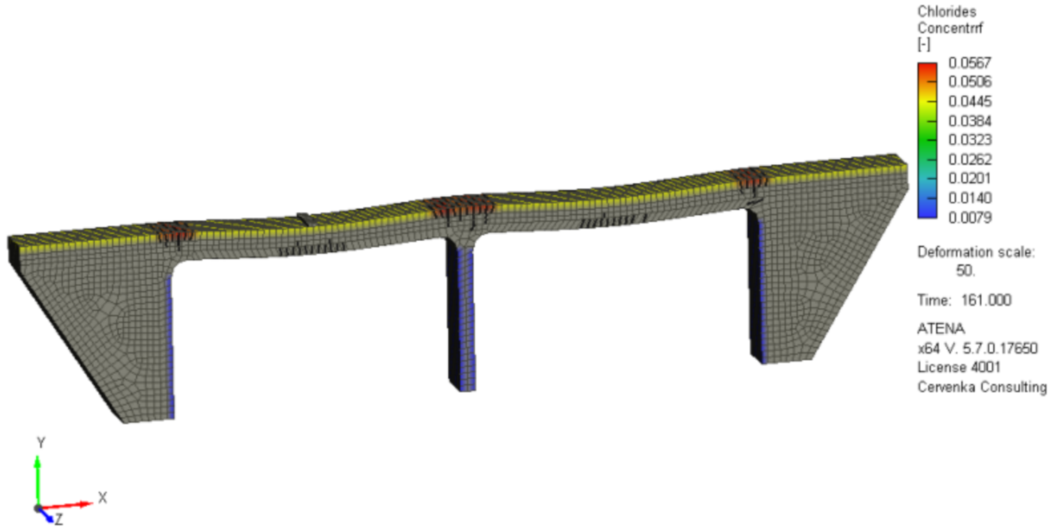

Figure 4.55: Chlorides concentration in the place of longitudinal reinforcement after 150 years

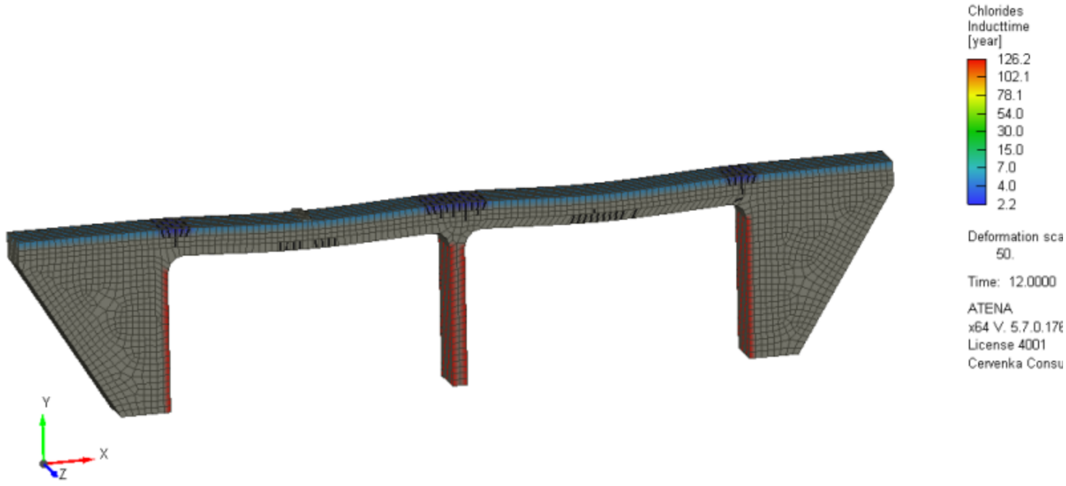

Figure 4.56: Influence of crack width on chlorides induction time

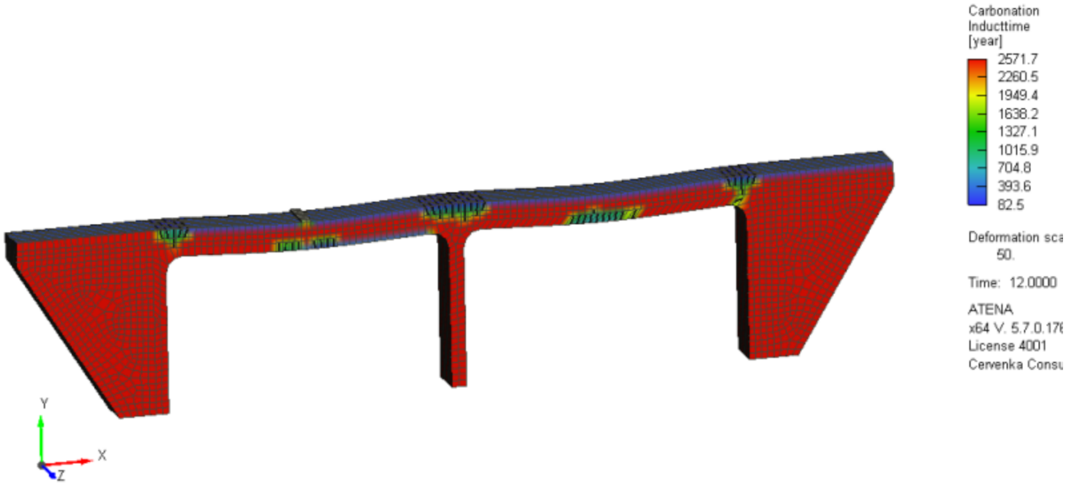

Figure 4.57: Influence of crack width on carbonation induction time

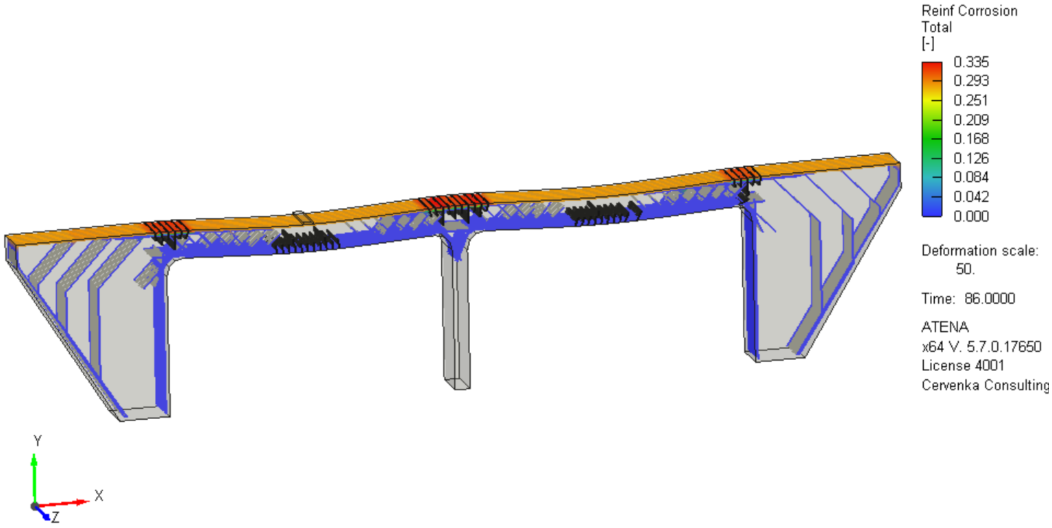

Figure 4.58: Total *Reinf Corrosion* at 75 years

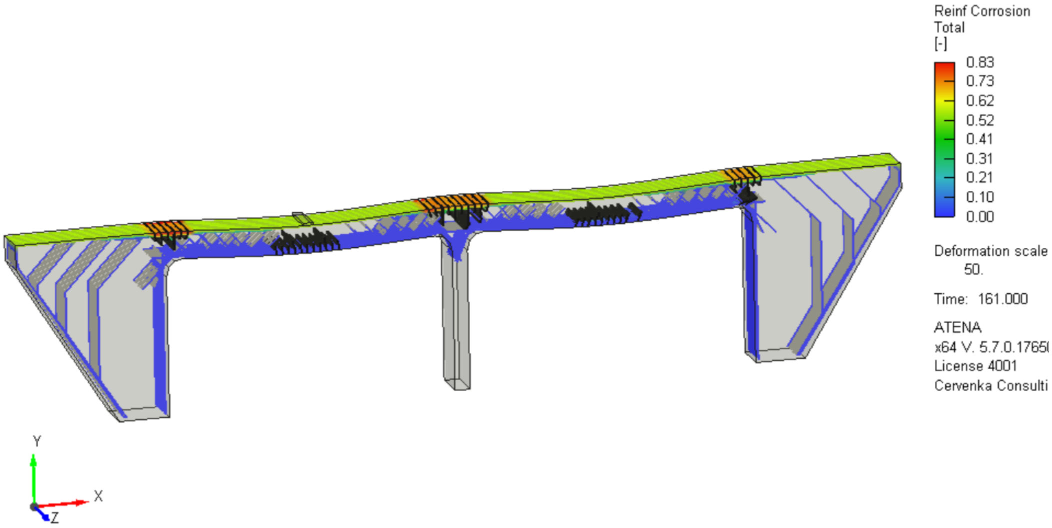

Figure 4.59: Total *Reinf Corrosion* at 150 years

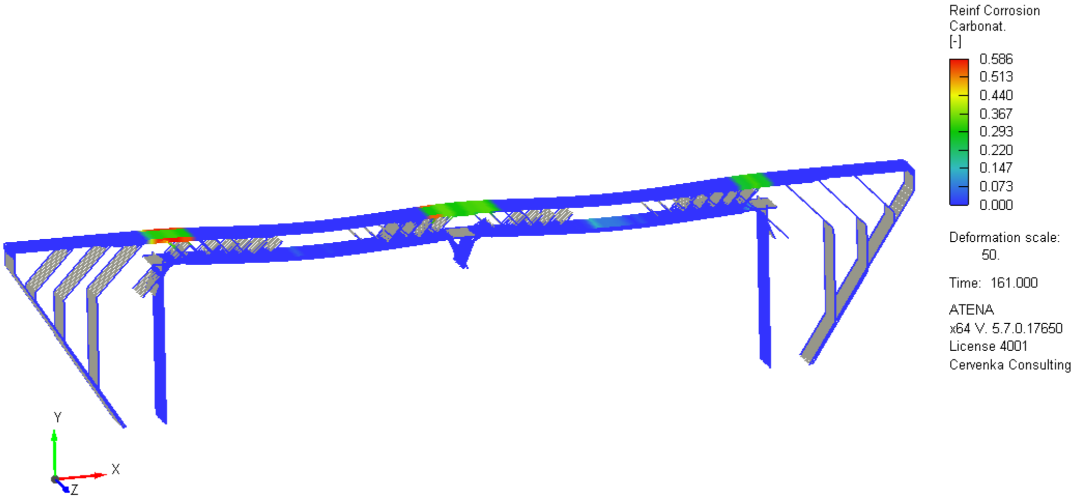

Figure 4.60: *Reinf Corrosion* due to carbonation for reinforcement at 150 years

4.4.1 Ultimate limit state analysis of Örnsköldsvik bridge

The following ULS analysis is performed for three moments. The first of them is the state before loading by chlorides and carbonation, the second and third is the state of the structure after 75 and 100 years of chloride and carbonation attack.

Load-deflection displacement diagram of the ULS analysis for centre of the left arch of the bridge is shown in Fig. 4.61. The structure is loaded by displacement and corresponding force is measured in the same point, marked by red arrow in Fig. 4.49. The maximal reached force after 75 years is 8.79 MN, reduction about 2.8% from the original force 9.05 MN, Fig. 4.62. In the second case of loading after 150 years, the reduction is about 5.3% to 8.5 MN. Reached stresses and decreased tensile strength near to structure failure from ULS analysis is shown in Figs. 4.63, 4.64. The ULS analysis does not prove a significant reduction of the load bearing capacity, this can be caused by excessive reinforcement and also by the fact that corrosion occurs only near the top layer of the concrete bridge. The presented analysis does not show substantial impact of corrosion caused by carbonation and chlorides on durability.

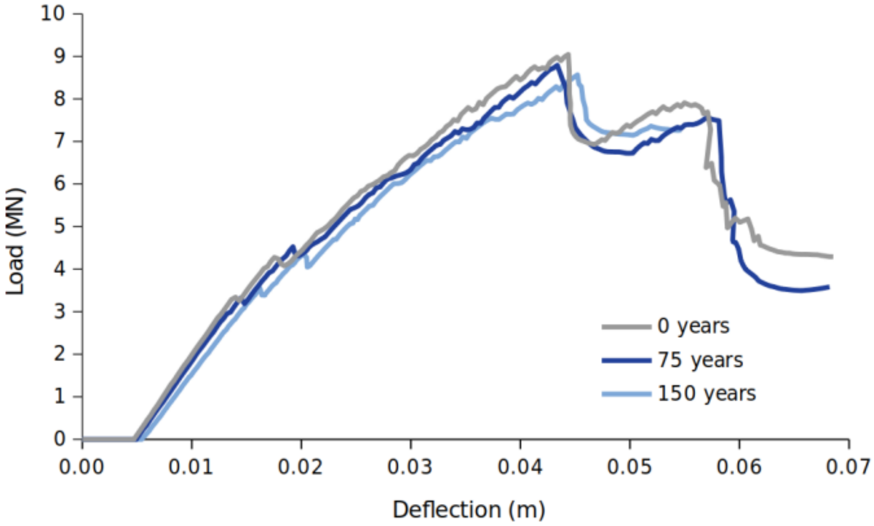

Figure 4.61: Force-displacement diagram of the ULS analysis - center of the left arch.

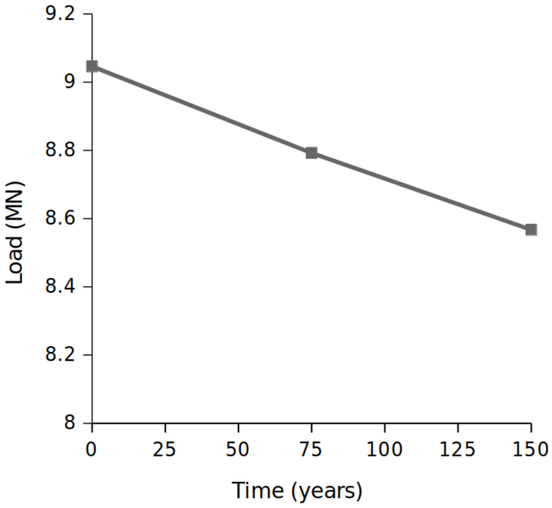

Figure 4.62: Force-time diagram of the ULS analysis - center of the left arch.

Figure 4.63: Reached stresses before the failure

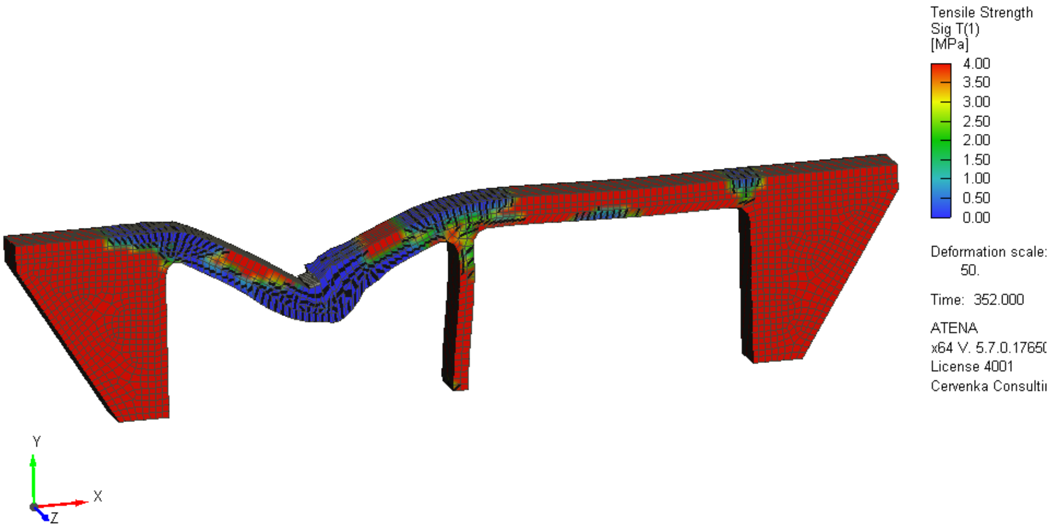

Figure 4.64: Residual tensile strength near to failure

4.5 Summary of ASR simulation workflow

The second area of this thesis addresses chemo-mechanical expansion for ASR. This section describes the modelling workflow for ASR including models presented in Chapter 3. Performance of these models is demonstrated on a concrete gravity dam, set as a benchmark example.

Modelling workflow of real structures attacked by ASR in Fig. 4.65.

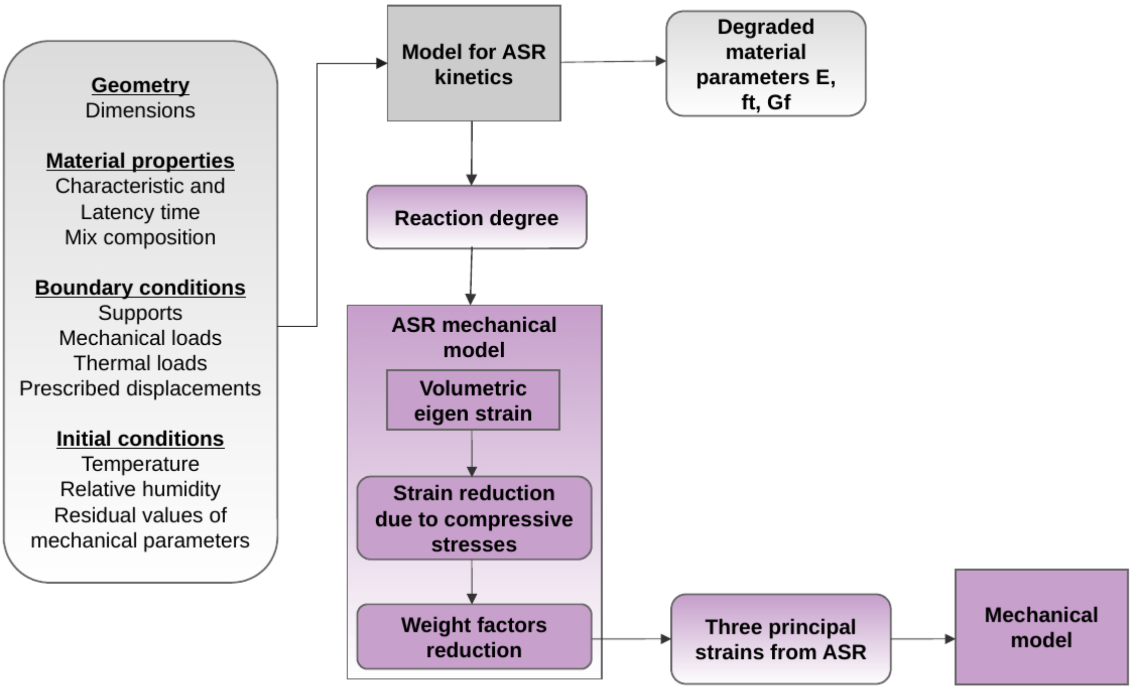

Figure 4.65: Modelling workflow for ASR

The combination of ASR models in Fig. 4.65 is implemented in a FEM software. Therefore, the non-linear structural analysis can assess deterioration due to ASR of large structures from real engineering practise.

The first model uses temperature, humidity and concrete composition for calculation of ASR kinetics, based on Ulm approach [110]. Calculated ξ evolution determines the direct isotropic degradation of the material parameters independent on the stress state in Eq. 3.45, Eq. 3.46, Eq. 3.47, where Saouma's model [90] is employed.

The volumetric strain ε_{ASR} from Eq. 3.53 which loads the material is obtained in the ASR mechanical model based on Saouma [90] in combination with Poyet's study [83], where reactive aggregates and amount of reactive silica in the aggregates play the biggest role. The volumetric strain is in the case of fixed element reduced due to formation of compressive stresses, see Fig. 3.55. The expansion is assigned to three directions. When the compressive stress reaches -0.3 MPa, the second strain reduction by weight factors occurs, according to Leger [54], Fig. 3.57.

4.6 Concrete Gravity Dam

Apart from the ASR kinetics model, Ulm also represents the use of its model on two structures [110]. The case study of the typical Concrete Gravity Dam was used to compare the ASR material model presented in this work, see Chapter 3.4 with results of Ulm's thermo-chemo-mechanical analysis [110]. The comparison uses available data of ASR extent and plastic strains after 7, 8 and >10 years.

Performance of ASR model on Concrete Gravity dam with a width of 41 m and a height of 52 m follows. The averaged water temperature 8°C is prescribed on the left site of the dam and the averaged air temperature 15°C on the right side.

The plotted field in Fig. 4.66 shows that temperature changes in a zone 13 m from the right surface, loaded by temperature of 15°C (θ_s = 288 K). Ulm describes this zone by "characteristic

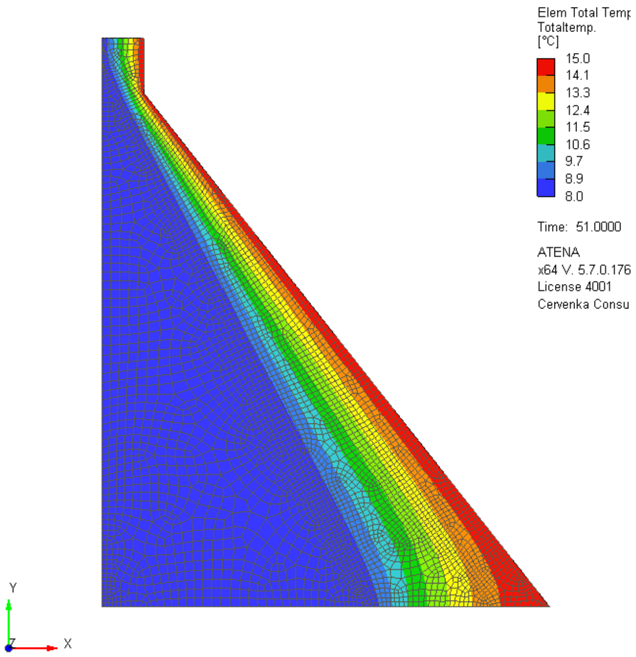

Figure 4.66: Temperature field used in the mechanical simulation

ASR Heat Diffusion Length" l_L [110]:

$$l_L = \sqrt{D_0 \tau_L(\theta_s)} \sim 13 \text{ m}, \quad \tau_L(\theta_s) = 2200 \text{ days} \tag{4.2}$$

The ASR reaction in Concrete Gravity dam is simulated in 151 steps on a model with 7510 hexahedra elements and parameters summarized in the Tab. 4.7. The model is treated as statically determinate, simply supported at two bottom points. The kinetics of the ASR reaction slows down at a lower temperature, as can be seen from the following Figs. 4.67, 4.69, 4.71. Therefore, the temperature evolution is substantial in the modelling of massive structures attacked by ASR. The loading of material by ASR-expansion induced strains leads to cracking after exhaustion of tensile strength. The first cracks are formed at the top of dam where is the thinnest area, see Fig. 4.70. As the expansion increase, cracking occurs along the reaction zone and crack propagation further into the structure, Fig. 4.72. ASR causes the surface delamination and damage of the rest structure, see Fig. 4.74.

Variable	Symbol	Value	Remarks
Maximal ASR expansion	$\varepsilon_{cal}^{\infty}$	0.0015%/kg/m^3	[110]
Thermal diffusivity	D_0	0.08 m^2/day	[110]
Characteristic time (T$_0$=38°C)	τ_c	50 days	[110]
Latency time (T$_0$=38°C)	τ_L	200 days	[110]
Thermal activation constant	U_C	5400 K	[110]
Thermal activation constant	U_L	9700 K	[110]
Poisson's ratio	ν	0.2	
Thermal dilatation coefficient	α	$1{\cdot}10^{-5}$ K^{-1}	[110]
Young's modulus	E	22 GPa	[110]
Tensile strength	$f_{t,0}$	2 MPa	[110]
Compressive strength	f_c	25 MPa	[110]

Table 4.7: Summarized parameters for validation proposed by Ulm study

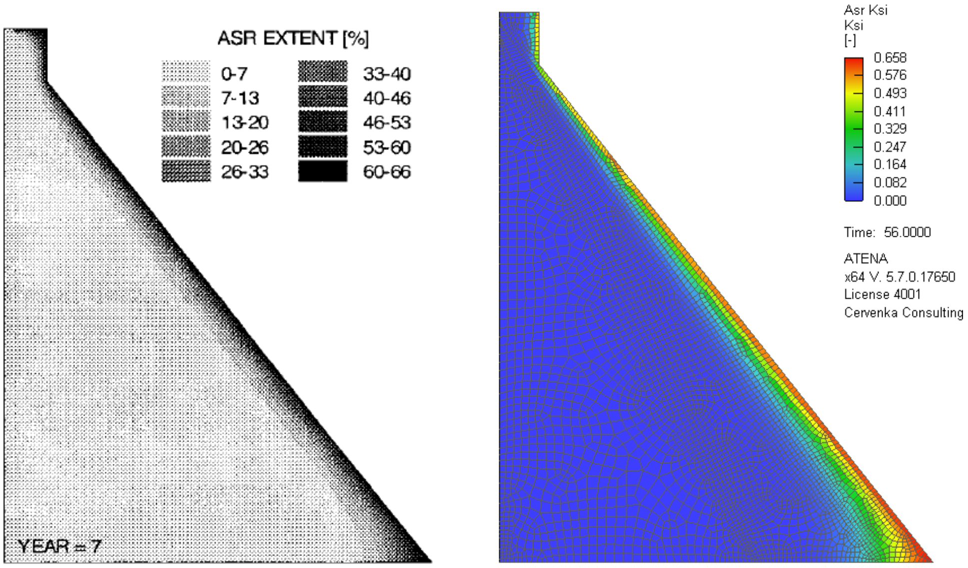

a) b)

Figure 4.67: ASR extent in modelled dam after 7 years b) compared with data proposed by Ulm [110] a)

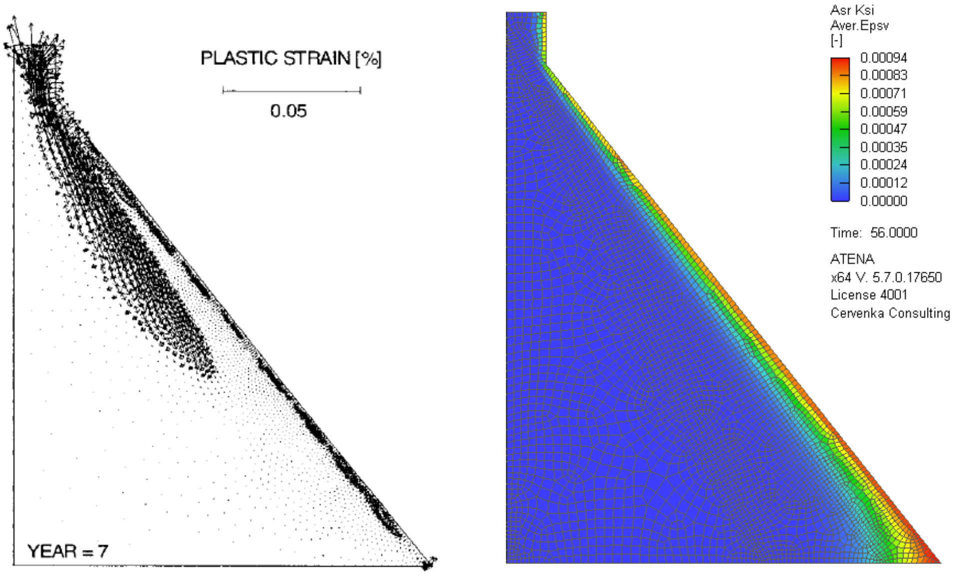

a) b)

Figure 4.68: Plastic strains proposed by Ulm [110] a) and modelled ASR expansion in Concrete Dam after 7 years b)

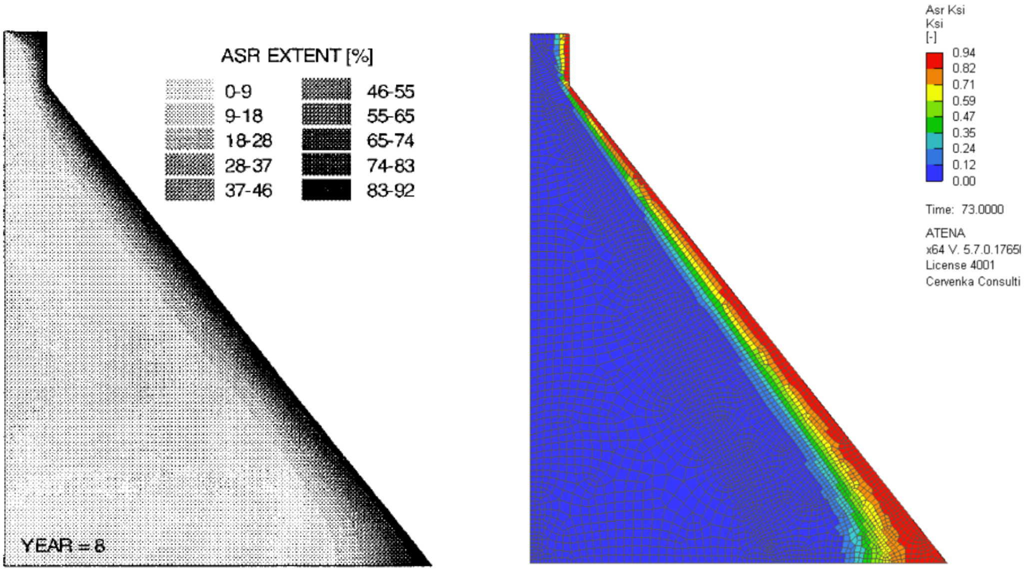

a) b)

Figure 4.69: ASR extent in modelled dam after 8 years b) compared with data proposed by Ulm [110] a)

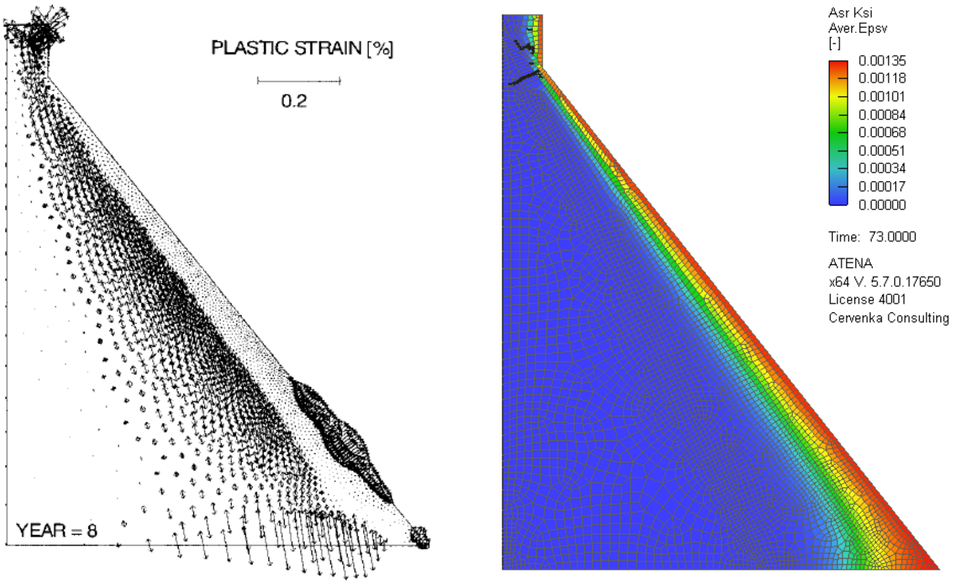

a) b)

Figure 4.70: Plastic strains proposed by Ulm [110] a) and modelled ASR expansion with cracking zones in Concrete Dam after 8 years b)

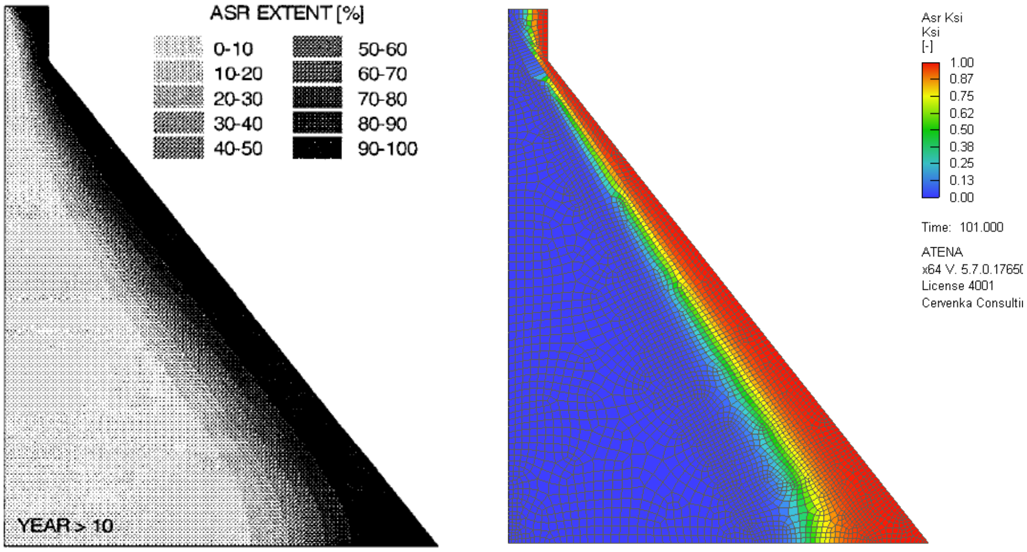

a) b)

Figure 4.71: ASR extent in modelled dam after 11 years b) compared with data proposed by Ulm [110] a)

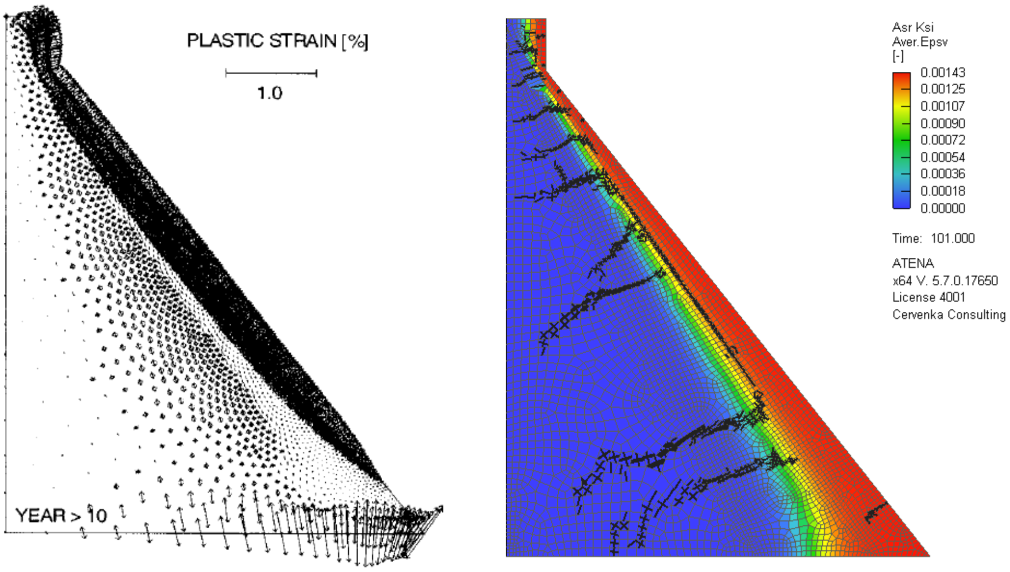

a) b)

Figure 4.72: Plastic strains proposed by Ulm [110] a) and modelled ASR expansion with cracking zones in Concrete Dam after 11 years b)

The Ulm's simulation in Fig. 4.68a), 4.70a) shows generation of large plastic strains at the top thinnest area of the dam. The same phenomenon is observed in our simulation in form of crack. ASR swelling causes the compression balanced by tensile stresses. When these tensile stresses reach tensile strength and the first crack is formed after 8 years, see Fig. 4.70b). Fracture and plastic strains with formed cracks after 8 years is shown in Fig. 4.73.

Stresses induced by ASR swelling behind the ASR front (i.e., at the surface) are depicted in Fig. 4.73a). The surface delamination occurs due to the restrained in-plane expansion as can be seen in Fig. 4.72b). Similar behaviour shows Ulm's simulation in Fig. 4.72a).

The performed simulation proves a common phenomenon, which is seen in dams attacked by ASR. Thanks to the use of the fracture-plastic model in our simulation, it is possible to predict the time of crack formation together with degradation of material parameters due to ASR.

As mentioned in the description of the ASR model used in our simulation 3.4. Our analysis considers the degradation of material parameters depending on ASR extent as shown in Fig. 4.76. To achieve more accurate results, it would be necessary to reduce them depending on the stress state. In this case, the strengths would be higher in the constrained elements (e.g. in the place where delamination occurs).

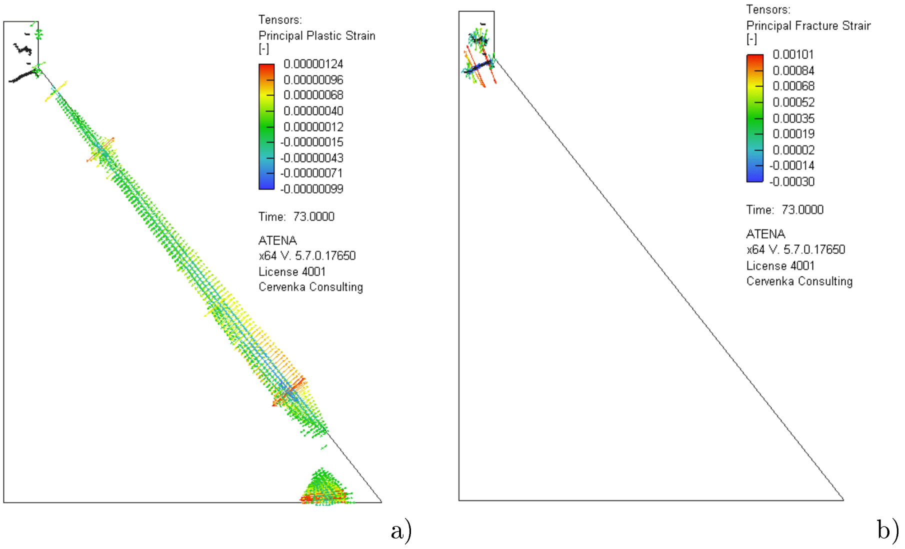

Figure 4.73: Crack formation in Concrete Dam after 8 years. Principal Plastic strains a) and Principal Fracture strains b)

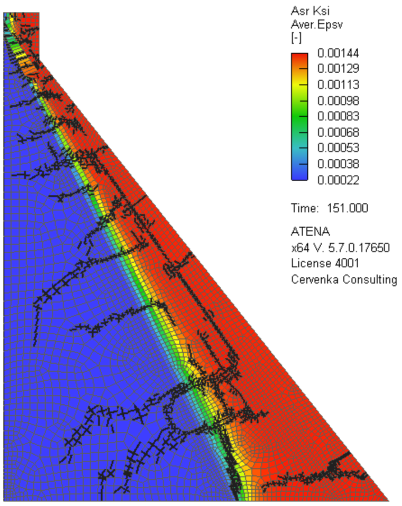

Figure 4.74: ASR expansion with crack zones in modelled dam after 15 years

Crack development in Concrete gravity dam after 11 and 15 years shows Fig. 4.75 with maximal crack width 8.8 mm after 15 years of ASR loading. The tensile strength is reduced in the place of cracks and due to direct reduction given by ASR extent near to the surface, see Fig. 4.76.

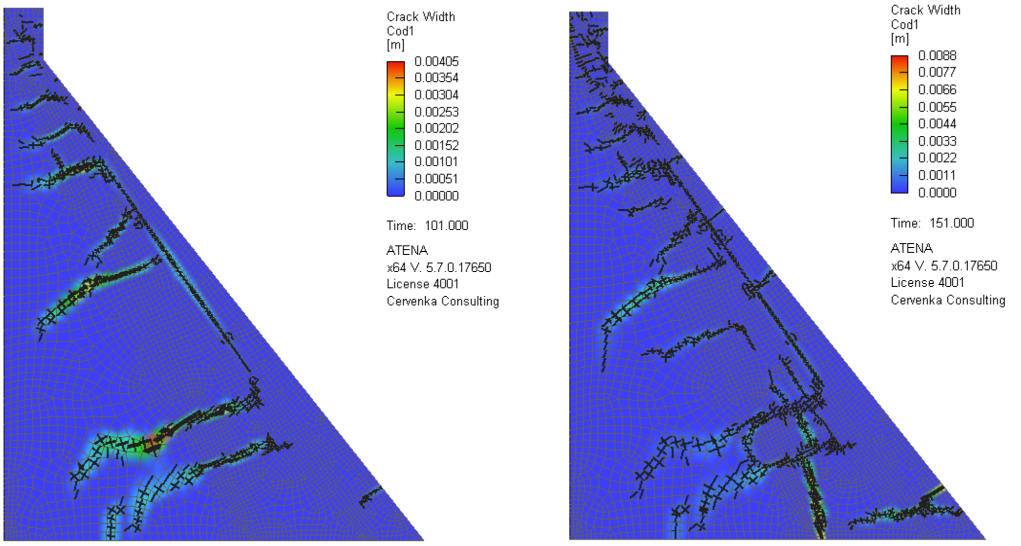

a) b)

Figure 4.75: Crack development in modelled Concrete Gravity Dam after 11 years a) and 15 years b)

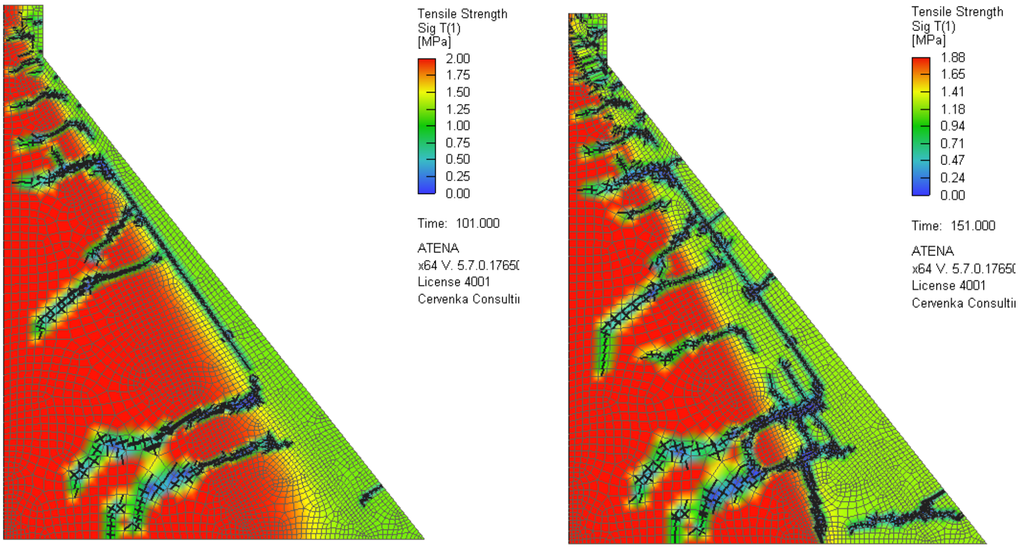

a) b)

Figure 4.76: Residual tensile strength due to ASR degradation after 11 years a) and 15 years b)

Chapter 5

Conclusion

5.1 Conclusion for chloride ingress and carbonation

This work presents a chemo-mechanical model, which allows the simulation of the most important stages during the service life of a steel reinforced concrete structure, i.e. initiation period, time of concrete cover cracking, time of concrete cover spalling and direct corrosion of reinforcement for chloride ingress and carbonation.

The initiation period is strongly affected by the critical chloride concentration and the concrete cover, concrete diffusivity becomes influenced by the cement type and porosity. An effective diffusivity for CO_2 given by mix proportions and relative humidity play the biggest role in initiation period calculation for carbonation. The amalgamated models take into account diffusion acceleration due to crack presence contributing to faster transport of CO_2 and chlorides.

The validation of concrete strut demonstrates that a crack width of 0.1 mm decreases the initiation time 2.6 times as compared to uncracked concrete for chloride ingress. In the case of carbonation, the induction time is decreased 3.6 times compared to uncracked concrete. For this reason, preventing deep macrocrack formation is a crucial factor for durable concrete. This can be facilitated by e.g. proper mix design or fully prestressed concrete structures.

The loss of the concrete cover and progressive corrosion still allows the serviceability of several concrete structures. This was demonstrated on Nougawa bridge, Japan, where spalling after 2 years and restoration after 30 years kept the bridge in service for 79 years in total. The load-bearing capacity decreased to 56.9 % but still kept the bridge in service. Simple diagnostic tools with the help of computational models allow estimating the load-bearing capacity of aging structures.

5.2 Conclusion for ASR

The presented chemo-mechanical model allows simulation of ASR expansion and associated concrete deterioration for free and constrained members with impact on structure integrity.

The main parameters influencing the modelled effect of ASR are experimentally measured expansion strains, relative humidity and temperature, especially in massive structures. Reduction of relative humidity below 75% in massive concrete structures is difficult to achieve. Thus, controlled temperature evolution, which most affects the ASR kinetics, may decrease the concrete deterioration and impact of ASR on structure stability.

The simulation of concrete gravity dam shows considerable deterioration during 11 years caused by ASR expansion. The ASR reaction leads to delamination of the surface which is exposed to the temperature gradient together with the extensive damage of the core part.

However, the description of the ASR should still be investigated and improved. A newly proposed split of volumetric strain needs further validation and refinement.

5.3 Future work

Several improvements and refinements of proposed models are possible:

- Improvements of presented models, e.g. reduction of the ASR extent depending on the stress, chloride binding isotherms, accurate determination of the surface chloride concentration, evolution of chloride diffusivity or a wick action. Chloride ingress is a partially reversible process which can be mitigated by electro-osmosis, reducing the level of chloride concentrations below critical levels,

- Benchmarks combining temperature, humidity, mechanics together with deterioration due to ASR are needed. Some stresses, temperatures and ASR strains data for material level and structures were proposed by Saouma and Hariri-Ardebili [90] in work “MERLIN Validation & Application of AAR Problems”. Ulm, in addition to Concrete gravity dam used in our simulation, also provides a bridge box girder [110]. Comi in arcticle “Two-phase damage modeling of concrete affected by alkali–silica reaction under variable temperature and humidity conditions” provides a Beauharnois dam simulation together with the reaction extent and damage. Beauharnois gravity dam displayed cracks due to ASR only six years after construction.
- Today, wider application of deterioration models is possible through software. This work could be considered the first step (besides e.g. SIMCO or EUCON) towards a simple design and assessment of the structures in terms of durability, through implementation of selected models in a software. The objective of this thesis was to create a software tool for civil engineers without a large amount of input data.

Chapter 6

Publications from the student

Generated from application https://v3s.cvut.cz; 22.03.2020 17:43; user: Ing. Karolina Jandová (Hájková)

- Jendele, L.; Hájková, K.; Šmilauer, V. and Červenka, J. "Modeling alkali-silica-reaction in reinforced concrete structures combining kinetics and fracture mechanics". In: *ECCM-ECFD 2018*. Glasgow, 2018-06-11/2019-06-15. Madrid: ECCOMAS, 2018.

- Jandová, K. et al. "Prediction of reinforcement corrosion due to chloride ingress and its effects on serviceability". In: *Engineering Structures*. 2018, 174 768-777. ISSN 0141-0296.

- Jedrzejewska, A. et al. "COST TU1404 Benchmark on macroscopic modelling of concrete and concrete structures at early age: proof-of-concept stage". In: *Construction and Building Materials*. 2018, 2018(174), 173-189. ISSN 0950-0618. DOI 10.1016/j.conbuildmat.2018.04.088.

- Wyrzykowski, M. et al. "Numerical benchmark campaign of COST Action TU1404 - microstructural modelling". In: *RILEM Technical Letters*. 2017, 2(1), 99-107. ISSN 2518-0231.

- Šmilauer, V.; Hájková, K.; Jendele, L. and Červenka, J. "Durability assessment of reinforced concrete structures due to chloride ingress up and beyond induction period". In: *39th IABSE Symposium*. Vancouver, 2017-09-19/2017-09-23. Zürich: IABSE c/o ETH Hönggerberg, 2017. pp. 2488-2495. ISBN 978-3-85748-153-6.

- Hájková, K. et al. "Validation of CTU Prague thermo-mechanical simulator with TU Graz restraining frame experiments". In: *2ND INTERNATIONAL RILEM/COST CONFERENCE ON EARLY AGE CRACKING AND SERVICEABILITY IN CEMENT-BASED MATERIALS AND STRUCTURES Volume 2*. Brusel, 2017-09-12/2017-09-14. Cachan: RILEM Publications, 2017. pp. 703-708. ISBN 978-2-35158-200-8.

- Hájková, K. et al. "Modelování koroze výztuže vlivem chloridů v železobetonových konstrukcích". In: *SAJDLOVÁ, T a J VÍCH, eds. 23. Betonářské dny 2016*. Litomyšl, 2016-11-30/2016-12-01. Praha: ČBS - Česká betonářská společnost ČSSI, 2016. pp. 1-6. ISBN 978-80-906097-6-1.

- Hájková, K. and V. Šmilauer. "Determination of steel corrosion rate". In: *ZOLOTAREV, I. a V. RADOLF, eds. Engineering Mechanics 2016 - Book of full texts*. 22nd International Conference on Engineering Mechanics, Svratka, 2016-05-09/2016-05-12. Prague: Institute of Thermomechanics, AS CR, v.v.i., 2016. pp. 186-189. ISSN 1805-8248. ISBN 978-80-87012-59-8.

- Hájková, K. et al. "Reinforcement corrosion in concrete due to carbonation and chloride ingress up and beyond induction period". In: *Eccomas 2016 Proceedings*. ECCOMAS Congress 2016 (VII European Congress on Computational Methods in Applied Sciences and Engineering), Chersonisos, 2016-06-05/2016-06-10. Paris: ECCOMAS, 2016.

- Šmilauer, V. et al. "ConTemp - A virtual thermo-mechanical simulator for hydrating reinforced concrete blocks with extension to service life". In: *Service Life of Cement-Based Materials and Structures.* Materials, Systems and Structures in Civil Engineering 2016, Lyngby, 2016-08-21/2016-08-24. Bagneux: Rilem Publications s.a.r.l., 2016. pp. 463-472. ISBN 978-2-35158-172-8.
- Šmilauer, V. and K. Hájková. "WG2: Model of carbonation and chloride ingress for cracked concrete structures". In: *SCHLICKE, D., M. AZENHA a S. STAQUET, eds. TU 1404 COST ACTION, Research posters' eBook.* 1st workshop of COST TU1404, Lublaň, 2015-04-16/2015-04-17. University of Ljubljana, 2015. pp. 30.

Bibliography

[1] Ahmed, T. et al. "The effect of alkali reactivity on the mechanical properties of concrete". In: *Construction and Building Materials* 17 (2003), pp. 123–144.

[2] Alexander, M. and Beushausen, H. "Durability, service life prediction, and modelling for reinforced concrete structures – review and critique". In: *Cement and Concrete Research* 8122 (2019), pp. 17–29.

[3] Alexander, M. and Santhanam, M. "Achieving durability in reinforced concrete structures: Durability indices, durability design and performance-based specifications". In: *TKeynote Paper at International Conferences on Advances in Building Sciences & Rehabilitation and Restoration of Structures.* Chennai, India, 2013.

[4] Alonso, C. et al. "Relation between resistivity and corrosion rate of reinforcements in carbonated mortar made with several cement types". In: *Cement and Concrete Research* 18.5 (1988), pp. 687–698.

[5] Alonzo, C. et al. "Factors Controlling Cracking of Concrete Affected by Reinforcement Corrosion". In: *Materials and Structures* 31 (1998), pp. 435–441.

[6] Angst, U. M. "Predicting the time to corrosion initiation in reinforced concrete structures exposed to chlorides". In: *Cement and Concrete Research* 115 (2019), pp. 559–567.

[7] Bamforth, P. B. "The derivation of input data for modeling chloride ingress from eight-year UK coastal exposure trials". In: *Magazine of Concrete Research* 51.2 (1999), pp. 87–96.

[8] Bazant, Z. P. "Physical Model for Steel Corrosion in Sea Structures - Theory". In: *ASCE Journal of the Strucutural Division* 105 (1979), pp. 1137–1153.

[9] Bažant, Z. P. and Oh, B. H. "Crack band theory for fracture of concrete". In: *Materials and Structures. RILEM Bookseries* 16.3 (1983), pp. 155–177.

[10] Bažant, Z. P. and Steffens, A. "Mathematical model for kinetics of alkali–silica reaction in concrete". In: *Cement and Concrete Research* 30 (2000), pp. 419–428.

[11] Bentz, E. C. et al. "Simplified Modified Compression Field Theory for Calculating Shear Strength of Reinforced Concrete Elements". In: *Structural Journal* 103.4 (2006), pp. 614–624.

[12] Berra, M. "Influence of stress restraint on the expansive behavior of concrete affected by alkali-silica reaction". In: *Cement and Concrete Research* 40 (2010), pp. 1403–1409.

[13] Beushausen,H. and Fernandez-Luco, L. *Performance-based specifications and control of concrete durability: State-of-the-Art Report of RILEM Technical Committee 230-PSC.* report. RILEM Publications S.A.R.L., 2015, p. 373.

[14] Boddy, A. et al. "An overview and sensitivity study of a multimechanistic chloride transport model". In: *Cement and Concrete Research* 29 (1999), pp. 827–837.

[15] Broomfield, J. P. *Corrosion of Steel in Concrete. Understanding, Investigation and Repair.* Spon Press, 2003.

[16] Broomfield, J. P. *Corrosion of Steel in Concrete.* 2nd edition. Taylor & Francis, 2007.

[17] Cady, P. D. and Weyers, R. E. "Chloride Penetration and the Deterioration of Concrete Bridge Decks". In: *Cement, Concrete, and Aggregates* 5.2 (1983), pp. 81–87.

[18] ccpl. "Reinforcement corrosion". 2020. URL: `www.ccpl.com.sg`.

[19] Červenka, J. and Papanikolaou, V. "Three Dimensional Combined Fracture-Plastic Material Model for Concrete". In: *Journal of Plasticity* 24.12 (2008), pp. 2192–2220.

[20] Červenka, J. et al. “On finite element modelling of compressive failure in brittle materials”. In: *Computational Modeling of Concrete Structures, Euro-C 2014*. St. Anton, Austria, 2014, pp. 273–281.

[21] Červenka, V. and Margoldová, J. “Tension Stiffening Effect in Smeared Crack Model”. In: *10th Conference of Engineering Mechanics*. Boulder, Colorado, 1995, pp. 655–658.

[22] Červenka, V. et al. *Atena Program Documentation, Part 1 Theory*. Cervenka Consulting, 2017.

[23] Collepardi, M. et al. “Penetration of chloride ions into cement pastes and concrete”. In: *Journal of the American Ceramic Society* 55.10 (1972), pp. 534–535.

[24] Comby-Perot, I. et al. “Development and validation of a 3D computational tool to describe concrete behaviour at mesoscale”. In: *Comput Mater Science* 46.4 (2009), pp. 1163–77.

[25] Comi, C. et al. “A chemo–thermo-damage model for the analysis of concrete dams affected by alkali–silica reaction”. In: *Mech Mater* 41 (2009), pp. 210–30.

[26] Czech Statistical Office. “Czech Statistical Office web page”. 2019. URL: `https://www.czso.cz/csu/czso/indexy-cen-stavebnich-praci-indexy-cen-stavebnich-del-a-indexy-nakladu-stavebni-vyroby-ctvrtletni-casove-rady-1-ctvrtleti-2019`.

[27] Darmawan, M. S. and Stewart, M. G. “Effect of Pitting Corrosion on Capacity of Prestressing Wires”. In: *Magazine of Concrete Research* 59.2 (2007), pp. 131–139.

[28] Duprat, F. “Reliability of RC beams under chloride-ingress”. In: *Construction and Building Materials* 21.8 (2007), pp. 1605–1616.

[29] EN 206-1:2013. *Concrete - specification, performance, production and conformity*. European Standard, 2013.

[30] Esposito, R. and Hendriks, M. “Degradation of the mechanical properties in ASR-affected concrete: overview and modeling”. In: *Strategies for Sustainable Concrete Structures* (2012).

[31] Farage, M. C. R. “Modelagem e implementacao numerica da expansao por reacao alcali–agregado do concreto, DSc thesis”. DSc thesis. Universidade Federal do Rio de Janeiro, COPPE, 2000.

[32] fhwa. “ASR crack-damage photos”. 2020. URL: `https://hesspumice.com/pumice-pages/pumice-uses/pumice-pozzolan-mitigates-asr.html`.

[33] FIB. *Model Code 2010*. International Federation for Structural Concrete (fib), 2010.

[34] fib. *Model code for service life design*. Switzerland, fib bulletin 34, 2006.

[35] Fratta, D. et al. *Corrosion Protection Performance of Epoxy-Coated Reinforcing Bars*. Tech. rep. Minnesota Department of Transportation, Feb. 2015.

[36] Gjørv, O.E. *Durability Design of Concrete Structures in Severe Environments*. CRC Press (Taylor & Francis Group), 2014.

[37] Gonzales, J. A. et al. “Comparison of Rates of General Corrosion and Maximum Pitting Penetration on Concrete Embedded Steel Reinforcement”. In: *Cement and Concrete Research* 25.2 (1995), pp. 257–264.

[38] Gowripalan, N. et al. “Chloride diffusivity of concrete cracked in flexure”. In: *Cem Concr Res* 12 (2000), pp. 725–730.

[39] Holt, E.E. *Early age autogenous shrinkageof concrete*. VTT Publications, 2001.

[40] Hordijk, D. D. “Local Approach to Fatigue of Concrete”. PhD Thesis. Delft University of Technology, 1991.

[41] ISO 13823. *General Principles on the Design of Structures for Durability*. International Organization for Standardization, 2008.

[42] Izumi, I. et al. *Carbonation*. Tokyo: Kibo press, 1986.

[43] Izumi, I. et al. “Design of Cover Thickness for Reinforcement in Concrete Structures :On Case of Reinforcement Corrosion Caused by Concrete Carbonation”. In: *Architectural Institute of Japan* 384 (1988), pp. 58–67.

[44] Janda, Z. “Nelineární modelování prostorových zděných a železobetonových konstrukcí programem Atena”. M.Sc. Thesis. ČVUT v Praze, 2007.

[45] Jirásek, M. and Zeman, J. *Přetváření a porušování materiálů*. ČVUT v Praze, 2006.

[46] Junek, V. "Pontex". Diagnostický průzkum a výpočet zatížitelnosti, X-567. 2016.

[47] Kagimoto, H. et al. "ASR expansion, expansive pressure and cracking in concrete prisms under various degrees of restraint". In: *Cement and Concrete Research* 59 (2014), pp. 1–15.

[48] Kobayashi, K. and Shuttoh, K. "Experimental and Analytical Studies on Oxygen Transport in Various Cementitious materials". In: *Cement and Concrete Research* 21 (1991), pp. 273–284.

[49] Kovalčíková, H. "Influance of changes in concrete pore structure on actually durability of reinforced and pre-stresses structures". M.Sc. Thesis. BRNO UNIVERSITY OF TECHNOLOGY, 2012.

[50] Kranc, S. C. and Sagüés, A. A. "Detailed modelling of corrosion macrocells on steel reinforcement in concrete". In: *Corrosion Science* 43 (2001), pp. 1355–1372.

[51] Kwon, S. J. et al. "Service life prediction of concrete wharves with early-aged crack: Probabilistic approach for chloride diffusion". In: *Structural Safety* 31.1 (2009), pp. 75–83.

[52] Kwon, S.-J. and Na, U.-J. "Prediction of Durability for RC Columns with Crack and Joint under Carbonation Based on Probabilistic Approach". In: *International Journal of Concrete Structures and Materials* 5.1 (2011), pp. 11–18.

[53] Larive, C. *Apports combinés de l'expérimentation et de la modélisation á la comprehension de l'alcali-reaction et de ses effets mécaniques*. Ecole Nationale des Ponts et Chaussées, 1997.

[54] Léger, P. et al. "Finite Element Analysis of Concrete Swelling due to Alkali-aggregate Reactions in Dams". In: *Computers & Structures* 60.4 (1996), pp. 601–611.

[55] Li, K. *Durability Design of Concrete Structures*. Wiley, Singapore, 2016.

[56] LIFE-365. *Service life prediction model, computer program for predicting the service life and life-cycle costs of reinforced concrete exposed to chlorides*. ACI Committee, 2005.

[57] Lindgard, J. et al. "Alkali–silica reactions (ASR): Literature review on parameters influencing laboratory performance testing". In: *Cement and Concrete Research* 43 (2012), pp. 223–243.

[58] Liu, T. and Weyers, R. W. "Modeling the dynamic corrosion process in chloride contaminated concrete structures". In: *Cement and Concrete Research* 28.3 (1998), pp. 365–367.

[59] Liu, Y. and Weyers, E. "Modeling the Time-to-Corrosion Cracking in Chloride Contaminated Reinforced Concrete Structures". In: *Materials Journal* 95.6 (1998), pp. 675–680.

[60] Mac, M. and Wong, H. "3D characterization of microcracks in concrete". In: (2017).

[61] Mangat, P. S. and Molloy, B. T. "Prediction of long term chloride concentration in concrete". In: *Materials and Structures* 27 (1994), pp. 338–364.

[62] Markeset, G. and Myrdal, R. *Modelling of reinforcement corrosion in concrete - State of the art*. SINTEF Building and Infrastructure, 2008.

[63] Martinez, I. and Andrade, C. "Examples of reinforcement corrosion monitoring by embedded sensors in concrete structures". In: *Cement and Concrete Composites* (2009), pp. 545–554.

[64] Maruya, T. et al. "Numerical Modelling of Steel Corrosion in Concrete Structures due to Chloride Ion, Oxygen and Water Movement". In: *Journal of Advanced Concrete Technology* 1.2 (2003), pp. 147–160.

[65] Maso, J. C. *Interfacial Transition Zone in Concrete: State-of-the-Art Report prepared by RILEM Technical Committee 108-ICC, Interfaces in Cementitious Composites*. report 11. London: E & FN Spon, an imprint of Chapman & Hall, 1996.

[66] Menetrey, P. and Willam, K. J. "Triaxial Failure Criterion for Concrete and its Generalization". In: *ACI Structural Journal* 92.3 (1995), pp. 311–318.

[67] Michel, L. "ifb.ethz.ch". 2020. URL: `https://ifb.ethz.ch/durability/research/ongoing-projects/initiation-of-chloride-induced-corrosion.html`.

[68] Multon, S. and Toutlemonde, F. "Effect of moisture conditions and transfers on alkali silica reaction damaged structures". In: *Cement and Concrete Research* 40 (2010), pp. 924–934.

[69] Multon, S. et al. “Coupled effects of aggregate size and alkali content on ASR expansion”. In: *Cement and Concrete Research* 38.3 (2007), pp. 350–359.

[70] Multon, S. et al. “Chemo–Mechanical Modeling for Prediction of Alkali Silica Reaction (ASR) Expansion”. In: *Cement and Concrete Research* 39 (2009), pp. 490–500.

[71] Multon, S. et al. “Effects of aggregate size and alkali content on ASR expansion”. In: *Cement and Concrete Research* 40 (2010), pp. 508–516.

[72] Muthena, A. et al. *DuraCrete, Final Technical Report.* 2000.

[73] Neville, A. “Chloride attack of reinforced concrete: an overview”. In: *Materials and Structures* 28 (1995), pp. 63–70.

[74] Nilsson, L. O. *HETEK: A system for estimation of chloride ingress into concrete: Theoretical Background.* Rapport - Vejdirektoratet. Danish Road Directorat, 1997. ISBN: 9788774917830. URL: `https://books.google.cz/books?id=Na7lNAAACAAJ`.

[75] Ožbolt, J. et al. “Modelling the effect of damage on transport processes in concrete”. In: *Constr. Build. Mater.* 24.9 (2010), pp. 1638–1648.

[76] Page, C. L. “Nature and properties of concrete in relation to environment corrosion”. In: *Corrosion of Steel in Concrete* (1992).

[77] Page, C. L. et al. In: *Cement and Concrete Research* 16 (1986), p. 79.

[78] Papadakis, V. G. “Effect of supplementary cementing materials on concrete resistance against carbonation and chloride ingress”. In: *Cement and Concrete Research* 30.2 (2000), pp. 291–299.

[79] Papadakis, V. G. and Tsimas, S. “Supplementary cementing materials in concrete. Part I: efficiency and design”. In: *Cem. Concr. Res.* 32.10 (2002), pp. 1525–1532.

[80] Parrott, L. J. *A review of carbonation in reinforced concrete.* Cement and Concrete Association, 1987.

[81] Petcherdchoo, A. “Pseudo-coating model for predicting chloride diffusion into surface-coated concrete in tidal zone: time-dependent approach”. In: *Cement and Concrete Composites* 74 (2016).

[82] Pourbaix, M. “Atlas of Electrochemical Equilibria in Aqueous Solutions”. In: *National Association of Corrosion Engineers* (1974). Houston, Texas, USA, pp. 307–321.

[83] Poyet, S. “Etude de la dégradation des ouvrages en béton atteints par la réaction alcali-silice: Approche expérimentale et modélisation numérique multi-échelles des dégradations dans un environnement hydro-chemomécanique variable”. PhD Thesis. Université de Marne-La-Vallée, 2003.

[84] Prakash, S. “UNIT V: Durability of concrete”. 2017. URL: `https://www.slideshare.net/selvaprakash549/durability-of-concrete-71805290`.

[85] Prasath, T. *Fffect of corrosion on bonding strength of reinforcement steel in concrete.* Tech. rep. DEPARTMENT OF MATERIALS SCIENCE and ENGINEERING, UNIVERSITY OF MORATUWA, SRI LANKA, 2013.

[86] Prochazka, J. “YTBK”. 2014. URL: `http://concrete.fsv.cvut.cz/~prochazka/YTBK/Prednaska%5C_2%5C_2014.pdf`.

[87] Rodriguez, J. et al. “Corrosion of Reinforcement and Service Life of Concrete Structures”. In: *Proceedings of International Conference on Durability of Building Materials and Components.* Ed. by B.H.V. Topping. 1996, pp. 117–126.

[88] Rommer, M. *Effect of moisture and concrete composition on the Torrent permeability measurement.* Empa, Swiss Federal Laboratories for Materials Testing and Research. Laboratories for Concrete & Construction Chemistry, Switzerland, 2004.

[89] Saouma, V. and Hariri-Ardebili, M.-A. *MERLIN Validation & Application of ARR Problems.* The University of Colorado, 2016.

[90] Saouma, V. and Perotti, L. “Constitutive model for alkali-aggregate reaction”. In: *ACI Mater J* 103.3 (2006), pp. 194–202.

[91] Shakouri, M. and Trejo, D. “A time-variant model of surface chloride build-up for improved service life predictions”. In: *Cement and Concrete Composites* (2017).

[92] Slobbe, A. T. et al. “Systematic assessment of directional mesh bias with periodic boundary conditions: Applied to the crack band model”. In: *Engineering Fracture Mechanics* 109 (2013), pp. 186–208.

[93] Šmilauer, V. “Durability overview, Lesson 10”. CTU in Prague. 2011.

[94] Šmilauer, V. et al. “Prediction of Carbonation and Chloride Ingress in Cracked Concrete Structures”. In: *Proceedings of the Fourteenth International Conference on Civil, Structural and Environmental Engineering Computing*. Ed. by B.H.V. Topping. 2013, pp. 1–12.

[95] Song, H. W. et al. “Service life prediction of concrete structures under marine environment considering coupled deterioration”. In: *J Restor Build Monum* 12 (2006), pp. 265–284.

[96] Song, H.-W. et al. “Predicting carbonation in early-aged cracked concrete”. In: *Cement and Concrete Research* 36.5 (2006), pp. 979–989.

[97] Song, H.W. et al. “Service life design of reinforced concrete structures and its verification”. In: *CMCL workshop, Qingdao* (2005).

[98] Mapei SpA. *The deterioration of concrete*. Mapei SpA, Milan, 2012.

[99] SPEC-NET. “Corrosivity Zones for Steel Construction from Galvanizers Association”. 2015. URL: `http://spec-net.com.au/press/1014/gaa%5C_081014.htm`.

[100] STADIUM software. “STADIUM”. 2020. URL: `www.simcotechnologies.com`.

[101] Tanaka, Y. et al. “Loading Test of RC Beam Bridge Built 80 Years Ago in Japanese Coastal Area”. In: *Modelling of Corroding Concrete Structures. RILEM Bookseries* 5 (2010), pp. 159–177.

[102] Tang, L. *Chloride Ingress in Concrete Exposed to Marine Environment - Field data up to 10 years’ exposure*. report. Boras, Sweden: SP Swedish National Testing and Research Institute, 2003.

[103] Tang, L. “Service-life prediction based on the rapid migration test and the ClinConc model”. In: *International RILEM Workshop on performance Based Evaluation and Indicators for Concrete Durability*. Madrid, Spain, Mar. 2006, pp. 157–164.

[104] Tang, L. and Nilsson, L. O. “A numerical method for prediction of chloride penetration into concrete structures”. In: *The Modelling of Microstructure and its Potential for Studying Transport Properties and Durability* 304 (1994), pp. 539–552.

[105] Tang, L. and Utgennant, P. *Chloride Ingress and Reinforcement Corrosion in Concrete under De-Icing Highway Environment – A Study after 10 Years’ Field Exposure*. SP Report 2007:76. SP Sveriges Tekniska Forskningsinstitut, 2007.

[106] Tang, L. et al. “Durability and service life prediction of reinforced concrete structures”. In: *Journal of the Chinese ceramic society* 43.10 (2015), pp. 1408–1419.

[107] Thomas, M. D. A. and Bentz, D. *Life 365 – Computer program for predicting the service life and life-cycle costs of reinforced concrete structures exposed to chlorides, User Manual (version 1.0.0)*. 2001. URL: `https://www.nrmca.org/research/Life365v2UsersManual.pdf`.

[108] Toongoenthong, K. and Maekawa, K. “Simulation of coupled corrosive product formation, migration into crack and propagation in reinforced concrete sections”. In: *J Adv Concr Technol* 3.2 (2005), pp. 253–265.

[109] Torrent, R. and Fernández, L. *Non-Destructive Evaluation of the Penetrability and Thickness of the Concrete Cover: State-of-the-Art Report of RILEM Technical Committee 189-NEC*. report 40. France: RILEM Publications S.A.R.L., 2007.

[110] Ulm, F. J. et al. “Thermo–chemo–mechanics of ASR expansion in concrete structures”. In: *Journal of Engineering Mechanics* 126.3 (2000), pp. 233–242.

[111] Český hydrometeorologický ústav. “Měsíční data”. 2016. URL: `http://portal.chmi.cz/historicka-data/pocasi/mesicni-data`.

[112] Val, D. and Melchers, R. E. “Reliability of deteriorating RC slab bridges”. In: *JOURNAL OF STRUCTURAL ENGINEERING* 123.12 (1997), pp. 1638–1644.

[113] Vu, T. and Steward, G. “Structural reliability of concrete bridges including improved chloride-induced corrosion models”. In: *Cement and Concrete Research* 22.4 (2000), pp. 313–333.

[114] Vytlačilová, V. and Dvorský, T. “Permeabilita a vodotěsnost betonu”. In: *Fyzikální a chemické vlastnosti stavebních hmot* (2008).

[115] Walraven, J. “Design for service life: how should it be implemented in future codes, international conference on concrete repair, rehabilitation and retrofitting”. In: ICCRRR, 2008, pp. 3–10.

[116] Walraven, J. et al. *Model Code 2010*. Fib, 2010.

[117] Wesavestructures. “Corrosion-evaluation”. 2020. URL: `https://www.wesavestructures.info/corrosion-evaluation`.

[118] Weyers, R. E. et al. *Concrete Bridge Protection and Rehabilitation: Chemical and Physical Techniques: Service Life Estimates*. Report SHRP-S-668. Strategic Highway Research Program. National Research Council, 1994.

[119] Wikipedia. “Carbonatation”. 2020. URL: `https://en.wikipedia.org/wiki/Carbonatation`.

[120] Wikiwand. “Alkali–silica reaction”. 2020. URL: `https://www.wikiwand.com/en/Alkali%E2%80%93silica_reaction`.

[121] Williamson, G. “Service life modeling of Virginia bridge decks”. Ph.D. Thesis. Virginia Polytechnic Institute and State University, 2007.

[122] Yalçyn, H. and Ergun, M. “The prediction of corrosion rates of reinforcing steels in concrete”. In: *Cement and Concrete Research* 26.10 (1996), pp. 1593–1599.